

Prairie View A&M University

Digital Commons @PVAMU

All Theses

12-2023

Woven Natural Fiber-Reinforced Pla Polymer 3d Printed Through A Laminated Object Manufacturing (Lom) Process

Sazidur Rahman Shahriar
Prairie View A&M University

Follow this and additional works at: <https://digitalcommons.pvamu.edu/pvamu-theses>

Recommended Citation

Shahriar, S. R. (2023). Woven Natural Fiber-Reinforced Pla Polymer 3d Printed Through A Laminated Object Manufacturing (Lom) Process. Retrieved from <https://digitalcommons.pvamu.edu/pvamu-theses/1526>

This Thesis is brought to you for free and open access by Digital Commons @PVAMU. It has been accepted for inclusion in All Theses by an authorized administrator of Digital Commons @PVAMU. For more information, please contact hvkoshy@pvamu.edu.

WOVEN NATURAL FIBER-REINFORCED PLA POLYMER 3D PRINTED
THROUGH A LAMINATED OBJECT MANUFACTURING (LOM) PROCESS

A Thesis

by

SAZIDUR RAHMAN SHAHRIAR

Submitted to the Office of Graduate Studies of
Prairie View A&M University
in partial fulfillment of the requirements for the degree of

MASTER OF SCIENCE

December 2023

Major Subject: Mechanical Engineering

WOVEN NATURAL FIBER-REINFORCED PLA POLYMER 3D PRINTED
THROUGH A LAMINATED OBJECT MANUFACTURING (LOM) PROCESS

A Thesis

by
SAZIDUR RAHMAN SHAHRIAR

Submitted to the Office of Graduate Studies of
Prairie View A&M University
in partial fulfillment of the requirements for the degree of

MASTER OF SCIENCE

Approve as to style and content by:

Lai Jiang
Chair of Committee

Xiaobo Peng
Member

Jaejong Park
Member

Jeffrey Streator
Head of Department

Pamela Obiomon
Dean, College of Engineering

Dr. Tyrone Tanner
Dean, Graduate School

December 2023

Major Subject: Mechanical Engineering

ABSTRACT

Woven Natural Fiber-Reinforced PLA Polymers 3D Printed through a Laminated Object
Manufacturing Process

(December 2023)

Sazidur Rahman Shahriar, B.S., Ahsanullah University of Science and Technology

Chair of Advisory Committee: Dr. Lai Jiang

This investigation explored an innovative additive manufacturing method that employed laminated object manufacturing (LOM) technology in combination with woven natural fiber-reinforced biopolymer. Conventional synthetic composites are made from crude oil that are nonrenewable and have few options for disposal or recycling, rendering them ecologically unfavorable. Integration of continuous woven natural fiber with polylactic acid (PLA) markedly enhances the mechanical strength to ensure complete biodegradability. Woven natural fiber-reinforced biocomposites are considered a promising alternative to synthetic composites. The potential applications of these fiber-reinforced PLA polymers include vehicle panels, construction materials, athletics equipment, and musical apparatuses.

The author has developed and constructed a prototype LOM 3D printer for this research. The LOM 3D printer prototype utilized a laser to cut the woven Jute/PLA, and the melted PLA powder helped to bond successive plies. The tensile and flexural characteristics of the LOM-printed biocomposites were assessed. For comparison,

corresponding values were measured from Fused Deposition Modeling (FDM) 3D-printed pure PLA specimens. The infusion of PLA polymer and the bonding with fiber were subsequently investigated under a Scanning Electron Microscope (SEM) by examining the cross-sections of the failed test specimens. The experiment results revealed that LOM 3D-printed biocomposites exhibited improved mechanical properties compared to FDM-printed pure PLA specimens. Additionally, the author conducted a Finite Element Analysis (FEA) simulation and compared it with the experimental outcomes. This research study successfully integrated the advantages of both material and process, consolidating them into a unified and sustainable approach.

***Index Terms-* Additive manufacturing, biocomposites manufacturing, finite element analysis (FEA), laminated object manufacturing (LOM), mechanical properties, polylactic acid (PLA), scanning electron microscope (SEM), woven natural fiber.**

DEDICATION

This thesis work is dedicated to my dear parents, Mr. Salahuddin Ahmed Shahriar and Mrs. Sajeda Yesmin, whose unwavering love and continuous support have been my guiding lights throughout my academic journey.

ACKNOWLEDGMENTS

I express my heartfelt gratitude to my advisor and committee chair Dr. Lai Jiang, for providing valuable guidance and mentorship during this project. Special thanks to Mr. Tony Grady from the Chemistry Department at Prairie View A&M University for his crucial assistance in testing the materials essential for this research. Lastly, I acknowledge the National Science Foundation (NSF) award #1900699 and the Prairie View A&M University Faculty-RISE Graduate Research Award 2022-23 for funding this research work.

TABLE OF CONTENTS

	Page
ABSTRACT.....	iii
DEDICATION.....	v
ACKNOWLEDGMENTS	vi
LIST OF FIGURES	ix
LIST OF TABLES.....	xv
CHAPTER	
1. INTRODUCTION	1
2. LITERATURE REVIEW	5
2.1 Classification of Additive Manufacturing (AM) Technologies.....	5
2.2.1 AM Technologies Based on VP Process.....	5
2.2.2 AM Technologies Based on PBF Process.....	8
2.2.3 AM Technologies Based on ME Process.....	11
2.2.4 AM Technologies Based on MJ Process.....	15
2.2.5 AM Technologies Based on BJ Process.....	17
2.2.6 AM Technologies Based on DED Process.....	19
2.2.7 AM Technologies Based on SL Process	21
2.2 Background Information on AM of Biocomposites	23
2.2.1 ME Process Based Biocomposites.....	23
2.2.2 PBF Process Based Biocomposites	25
2.2.3 VP Process Based Biocomposites	27
2.2.4 SL Process Based Biocomposites.....	28
2.3 Mechanical Properties of Natural Fiber Reinforced Composites	30
3. METHODOLOGY.....	45
3.1 The LOM Prototype Design and Development.....	45
3.1.1 Customer Needs	45
3.1.2 Brainstorming and Selection of Solutions.....	46
3.1.2.1 Laser Head Selection.....	48

3.1.2.2	Motherboards, Motor and Motor Drives Selection.....	49
3.1.3	Design Specifications.....	49
3.1.4	CAD Models of The Parts and The Final Product.....	50
3.1.4.1	Main Frame CAD Model.....	50
3.1.4.2	Build Plate CAD Model	51
3.1.4.3	Material Feed and Wastage Take-up Roller CAD Models.....	51
3.1.4.4	Laser Head CAD Model.....	52
3.1.4.5	The Final LOM Prototype CAD Model.....	52
3.1.5	Prototype Building and Assembly.....	53
3.1.5.1	Frame, Build Plate, and Laser Head Assembly.....	53
3.1.5.2	Motherboard Connection Setup.....	54
3.1.6	Debugging and Testing.....	57
3.1.6.1	CAD Designs for Testing.....	57
3.1.6.2	G-code Implementation.....	58
3.1.6.3	LOM Printed Parts for Testing.....	59
3.2	Preparation of Materials and Mechanical Test samples.....	60
3.3	Mechanical Test Methodology.....	63
3.3.1	Tensile Tests.....	63
3.3.2	Flexural Tests.....	67
3.3.3	SEM Imaging Tests.....	70
3.4	FEA Simulation of LOM Printed Jute/PLA Biocomposite.....	71
3.4.1	Tensile Properties FEA Simulation.....	74
3.4.2	The 3-point Bending Properties FEA Simulation.....	79
4.	RESULTS AND DISCUSSIONS.....	87
4.1	Tensile Test.....	88
4.2	Flexural Test.....	90
4.3	SEM Imaging	92
4.4	Discussion of The Stress Fields Obtained From The FEA Simulation....	93
5.	CONCLUSIONS.....	97
	REFERENCES.....	99
	CURRICULUM VITAE.....	111

LIST OF FIGURES

FIGURE	Page
1. Laminated object manufacturing (LOM).....	3
2. (a) SLA, (b) DLP, and (c) CLIP process	6
3. (a) SLA/TiO ₂ tensile properties, (b) SLA/lignin tensile properties	7
4. (a) DLP method, (b, c) DLP printed cat, (d, e) DLP printed test specimens, and (f, g) DLP printed honeycomb structures.....	7
5. (a) SLS process, (b) DMLS process, and (c) EBM process.....	9
6. SLM-printed Ti–TiB composites compressive true stress–strain curves.....	10
7. Fused deposition modelling	12
8. Mechanical properties for FDM CGF/PA6 printing samples: (a) tensile properties; (b) flexural characteristics; and (c) impact strength	13
9. SEM micrographs for FDM printed glass fiber reinforced PLA/TPU composites: (a) no treatment, (b) one-hour of acetone treating, (c) four hours of annealing, and (d) eight hours of annealing	13
10. Direct ink writing process	14
11. (a) (i) DIW of gel PDPCPD solution to create free-form 3D-printed structures, (ii) DIW printed structures of cyanate ester polymerization, and (b) SC-DIW printed parts mechanical properties.....	15
12. (a) MJ working principle; and (b) MJ printing part	16
13. (a) Binder jetting, and (b) sandstone made parts by binder jetting.....	18

14. (a) Basic DED process, (b) WFDED process, (c) GMAW process, (d) GTAW process, and (d) PAW process.	20
15. Ultrasonic assisted LOM process and printed parts.....	22
16. PP, PLA, PLA+WF, FDM printed PLA+WF, and pure PLA (a) Tensile Modulus, (b) Flexural Modulus, PLA, JFRTP, CFRTP, (c) Tensile Modulus, and (d) Tensile Strength.....	25
17. Comparisons of mechanical properties: (a) SLS-printed WPCs, (b) SLS-printed WPCs and RPCs, and (c) SLS-printed wax- infiltrated WPCs and RPCs.....	26
18. (a) Tensile Test Curves, and (b) Tensile Fracture Strength of Pure Resin, CF, GF, HSPE.....	27
19. Comparison of: (a, b) tensile, and (c, d) flexural properties of hydrovanilloin, elium and jute/hydrovanilloin and jute/eliium samples	29
20. (a) CBAM working principle, and (b) CBAM printed carbon-nylon comparison with FDM printed carbon-nylon.	30
21. Schematic of natural fiber composition.	32
22. Manufacturing steps required to produce biocomposite filaments	35
23. (a) PLA reinforced wood, (b) ABS reinforced kenaf, and (c) PLA reinforced astragalus biocomposites filaments.....	35
24. SEM images of wood and PLA (a) 500 μm , and (b) 50 μm	35
25. (a) Hemp/Harakeke mixed with PLA tensile characteristics, (b) Hemp/Harakeke mixed with PLA Young's modulus, (c) PP/harakeke and PP/hemp tensile properties, and (d) PP/harakeke and PP/hemp Young's modulus	36
26. SEM images of composites: (a) jute fiber with PE, (b) jute fiber with PE and MA, (c) jute fiber with PE and MA clay, (d) jute fiber with PE and MA silica; (e) tensile properties comparison, and (f) comparison of Young's modulus	38

27. (a) Laminated woven bamboo and strip bamboo samples, (b) tensile strength, (c) tensile modulus, (d) flexural strength, and (e) flexural modulus.....	39
28. (a) SEM image of jute/mycelium biocomposites, (b) laminated biocomposites orientation, (c) mycelium-based biocomposites sandwich structures, (d) biocomposites design following ASTM C393 standard, (e) jute, flax and BioMid reinforced beam specimens, (f) core shear yield stress comparison, (g) core shear ultimate strength comparison, and (h) flexural modulus comparison.....	41
29. Manufacturing steps to create PP-based composites reinforced with jute, kenaf, and PALF	42
30. (a) Jute specimens, (b) kenaf specimens, (c) PALF specimens, (d) specimen dimension (ASTM D638), (e) tensile Strength, (f) tensile Modulus, (g) flexural Strength, and (h) flexural Modulus of all specimens.....	43
31. SEM images of jute, kenaf, and PLAF fibers	44
32. Application of natural fiber reinforced biocomposites	46
33. CleanGreen3D limited CG-1 LOM 3D printer.....	47
34. (a) Failed 5.5W, 7.5W and 10W laser heads, and (b) selected 40W laser head. ..	48
35. MKS DLC32 motherboard with MKS TS35 RV2.0 touchscreen and A4988 motor drivers.	49
36. Design of the main frame of the LOM prototype.	50
37. Design of build plate of the LOM prototype.	51
38. Design of the material feed and wastage take-up roller with necessary components, i.e., pulley, timing belts, and stepper motor covers.	51
39. CAD design of 40W laser head.	52
40. 3D CAD design of LOM prototype.	52

41. The assembled LOM prototype.	54
42. MKS DLC32 interface introduction.	55
43. (a) Motor drive Settings, (b) micro-step setting for A4988 drivers, (c) laser module connection, and (d) touch screen interface (EXP1 and EXP2).	56
44. (a) MKS TS35 touchscreen panel interface, and (b) MKS DLC32 with necessary wire connections and motor drives.	56
45. (a) Spur gear CAD Design, (b) key tag CAD design, (c) wrench CAD design....	57
46. (a) Spur gear sliced layers, (b) key tag sliced layers, (c) wrench sliced layers. ...	57
47. (a) Spur gear G-code implementation in NC-viewer, (b) key tag G-code implementation in NC-viewer, and (c) wrench G-code implementation in NC-viewer.	59
48. (a) Wrench G-code uploaded shown in MKS TS35 touchscreen, and (b) LOM 3D printed PLA infused Jute fiber reinforced wrench, key tag, and spur gear.	60
49. (a) Woven jute fiber used in this research, (b) weighted single layer jute fiber, and (c) weighted PLA coated jute fiber.	61
50. Manufacturing steps for LOM printed PLA infused woven jute fiber reinforced biocomposites.	62
51. INSTRON 5582 universal testing machine.	64
52. (a) ASTM D3039/D3039M-14 tensile specimens' dimension, (b) SolidWorks design for preparing the G-code, and (c) G-code for LOM print.	65
53. LOM printed PLA infused woven jute fiber reinforced biocomposites.	65
54. (a) ASTM D638-14 tensile Specimen Dimension, and (b) SolidWorks design for preparing the G-code.	66

55. (a) Raise 3D pro2 Plus FDM 3D printer, and (b) Pure PLA filament FDM 3D printed tensile specimens	66
56. Woven jute fibers cut for tensile tests following ASTM D5035 – 06	67
57. (a) ASTM D7264/D7264M-07 flexural test dimensions, (b) SolidWorks design, and (c) G-code for LOM print.	68
58. LOM prototype printed flexural test specimens	69
59. a) ASTM D790-10 standard flexural specimen dimension, (b) CAD design of the flexural specimen, and (c) Raise 3D FDM printed flexural specimens	69
60. (a) JEOL JSM-6010LA SEM machine, and (b) failed mechanical test samples loaded into the SEM.....	71
61. Project schematic for the FEA simulation of LOM printed jute/PLA biocomposites tensile specimen.	75
62. Geometry of the single layer jute/PLA tensile test specimen in ANSYS.....	75
63. Six-layer jute/PLA biocomposite tensile specimen.	76
64. Meshing of LOM printed jute/PLA biocomposites.	77
65. Fixed support applied to one end of the jute/PLA biocomposite tensile specimen.	78
66. Force applied to the other end of the jute/PLA biocomposite tensile specimen...	78
67. Tensile stress FEA Simulation of LOM printed jute/PLA biocomposites.	79
68. Elastic strain FEA Simulation of LOM printed jute/PLA biocomposites.	79
69. Project schematic for the FEA simulation of LOM printed jute/PLA biocomposites flexural specimen.	81

70. Geometry of LOM printed jute/PLA biocomposites flexural specimen with a load and two supports.	81
71. Geometry of single-layer LOM printed jute/PLA biocomposites flexural specimen.	82
72. Meshing of single-layer LOM printed jute/PLA biocomposites flexural specimen.	82
73. Stacking of layers for the LOM printed jute/PLA biocomposites flexural specimen (first 10 of 12 layers).....	83
74. Stacking of layers for the LOM printed jute/PLA biocomposites flexural specimen (final 2 of 12 layers).....	83
75. Meshing for the FEA simulation of LOM printed jute/PLA biocomposites flexural specimen.	84
76. Remote displacements applied in load and two supports for the FEA simulation.	85
77. Flexural stress FEA simulation of LOM printed jute/PLA biocomposites.....	86
78. Flexural strain FEA simulation of LOM printed jute/PLA biocomposites.....	86
79. Comparisons of (a) tensile, and (b) flexural strengths of pure PLA, jute fabric (tensile only), and fiber-reinforced PLA (FR-PLA)	88
80. Tensile test stress-strain curves (a) PLA, and (b) woven jute fiber-reinforced PLA	89
81. Tensile stress-strain curves for natural jute fiber.....	90
82. Flexural test stress-strain curves of (a) woven jute fiber-reinforced PLA, and (b) pure PLA.....	91
83. SEM imaging of (a) jute fiber and PLA polymer with voids ($\times 700$), and (b) the interface of jute reinforcement fiber and PLA polymer matrix ($\times 1,500$)	93

LIST OF TABLES

TABLE	Page
I. Natural fiber properties	33
II. Comparison of properties of e-glass fiber to natural fibers	34
III. Jute fiber cut lengths on the tensile strength (MPa) of jute-fiber composites	40
IV. Design specifications for the LOM prototype	49
V. Woven jute fiber reinforced PLA biocomposites' mechanical properties data for FEA simulation	73
VI. Mechanical properites of PLA and jute/PLA specimens	87
VII. Comparison of FEA simulated data and the experimental data	94

CHAPTER 1

INTRODUCTION

In the age of smart manufacturing, additive manufacturing (AM) is the way of the future. AM in recent years has reduced the need for conventional manufacturing because it allows the manufacturing sector to process more quickly than traditional manufacturing techniques, thereby increasing productivity. AM techniques are now widely used because they are affordable and can create complex shapes with little material waste. The term AM means to layer materials to produce parts from computer-aided design (CAD) data.

3D printing is widely known as another name for AM. 3D printing enables manufacturing teams working on product design and development to simulate how their product will appear and operate successfully. Some of the key characteristics of AM include the widespread use of CAD software, access to various printable materials, and the use of inexpensive mechanical parts in 3D printers. AM technologies have been around for over three decades and now come with newer techniques and more materials. For instance, automakers use AM to create functional prototypes, fuel tanks, brake parts, and air vents. Similarly, aerospace industries produce pilot seats, landing gear, and aircraft engine brackets. Utilizing 3D printing, the medical sector manufactures essential dental parts like crowns, bridges, and dentures.

Despite decades of rapid growth, AM industries experienced losses due to the Covid-19 pandemic. Revenue losses of 38%, 32%, and 12%, respectively, between 2019 and 2020 were experienced by Desktop Metal, GE Aviation, and 3D Systems [1]. The demand for raw materials and 3D printers decreased simultaneously as the aerospace and automotive industries were also affected. Because of this, GE reported losing 10,000 aviation jobs, Boeing reduced the number of aircraft it produced, and Airbus saw a 55% decline in revenue [1]. This demonstrates the significant influence that 3D printing has right now on the manufacturing sector.

The current use of additive manufacturing has two drawbacks: 3D-printed structures have poor mechanical properties and need to be more environmentally friendly. 3D printing materials heavily rely on plastics which is harmful to the environment. Therefore, two-phase inhomogeneous composite materials, which are composed of softer matrix material and a hard load-bearing reinforcing phase, have become a potential material option for 3D printing. Conventional synthetic composites, sourced from finite crude oil, pose environmental concerns due to their restricted disposal options. Due to environmental concerns, researchers currently use different polymer and polymer-based composite materials in additive manufacturing. Natural fiber-reinforced polymers are attracting increased attention as an alternative to glass fiber-reinforced polymer composites. This is due to their cost-effectiveness, biodegradability, lower carbon footprint, and satisfactory mechanical properties. [2].

In this research, an eco-friendly additive manufacturing technology for 3D printing biocomposite materials was implemented using the Laminated Objected Manufacturing (LOM) process. LOM, an AM technique, creates a tangible model by layering sheets of

stock material, with each sheet precisely cut to match the cross-sectional profile of a CAD model divided into layers. Fig. 1 shows the LOM technique. These cut layers are successively stacked and pressed atop the preceding ones to construct the final part. Surplus material in each layer serves as support for the entire part throughout the construction process. Typical raw materials for LOM consist of paper and metal sheets, ranging from 0.05 to 0.50 mm in thickness (0.002 to 0.020 inches) [3]. However, these feedstocks have limited mechanical properties, which leads to minimal engineering applications.

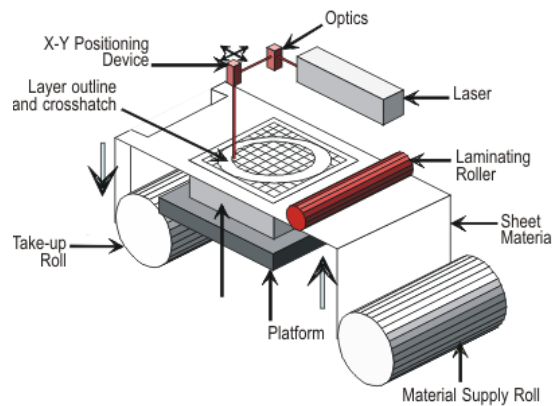


Fig. 1 Laminated object manufacturing (LOM) [4].

Therefore, this research study used a custom-designed LOM prototype and natural woven jute fibers as the primary feedstock materials. Jute fibers exhibit favorable mechanical properties in comparison to various other natural fibers. Jute fibers are considered a highly promising reinforcement material due to their substantial cellulose hemicellulose, lignin, and pectin content [5]. Polylactic acid (PLA, $(C_3H_4O_2)_n$ [6]) is used for the polymer matrix. PLA is used as a biopolymer as it can be made reasonably cheaply using renewable resources, and the melting temperature is typically 170°-180°C. PLA is an aliphatic polyester owing to the presence of ester bonds linking the monomer units. This classification enables natural degradation through hydrolysis. Here polymer backbone was

generated by water molecules breaking the ester, establishing it as an environmentally friendly matrix polymer material. [7]. The primary goal of this research was to showcase that the LOM printing of woven jute fiber incorporated with PLA polymers exhibits enhanced mechanical properties in comparison to FDM printed parts using pure PLA filament. The author used tensile and flexural properties, SEM images, and FEA simulation to test the LOM printed jute/PLA specimens.

The subsequent sections of this thesis comprise five chapters. Chapter 2 offers a comprehensive review of existing studies on additive manufacturing, biocomposite materials, and their components. Chapter 3 elucidates the research design, methodologies, experimental procedures, and data collection processes. Chapter 4 delves into the results outlined in Chapter 3, providing discussions. Finally, Chapter 5 is dedicated to summarizing overarching conclusions drawn from the entire thesis and proposing potential avenues for future research relevant to manufacturing industries and other stakeholders.

CHAPTER 2

LITERATURE REVIEW

2.1 Classification of Additive Manufacturing (AM) Technologies

There are 7 classifications of AM, and these are: Vat Photopolymerization (VP), Material Jetting (MJ), Binder Jetting (BJ), Material Extrusion (ME), Sheet Lamination (SL), Powder Bed Fusion (PBF), and Directed Energy Deposition (DED) [8].

2.1.1 AM Technologies Based on VP Process

VP solidifies a liquid resin when exposed to a laser emitting a particular frequency of light to create a part[8]. Popular technologies of VP are Stereolithography (SLA), 2) Direct Light Processing (DLP) and Continuous Liquid Interface (CLIP) [9]. These processes are shown in Fig. 2. SLA relies on ultraviolet (UV) light. DLP printing employs digital micromirror (DMD) light. CLIP utilizes DMD light for polymerization. SLA achieves curing through a laser, DLP utilizes a projector, and CLIP relies on LEDs and Oxygen for curing. The DLP process is swifter than SLA technology, as each layer undergoes complete exposure to curative illumination emanating from a digital display [9]. DLP technique is employed to enhance the projector count in the device, aiming to improve the geometric precision of large components. Nevertheless, the disadvantages associated with DLP technology include the diminished mechanical strength of the produced [9]. Due to the continuous movement of the platform, CLIP can produce components with superior accuracy and mechanical characteristics compared to DLP. However, SLA technology can achieve higher accuracy compared to DLP and CLIP [9, 10, 11]. One significant drawback

associated with VP's post-processing is its extended duration and higher cost when contrasted with alternative additive manufacturing technologies.

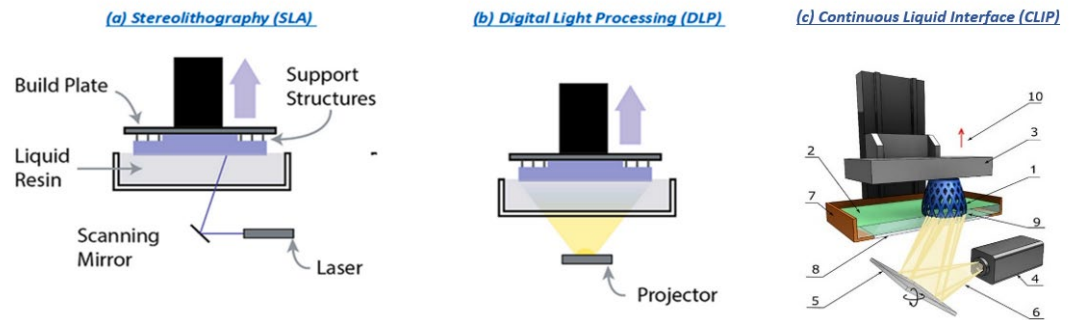


Fig. 2 (a) SLA, (b) DLP, and (c) CLIP process [9, 10, 11].

Mummareddy et al. [12] explored SLA printed ceramic-metal composites fracture properties. The compressive and flexural strengths of this composite were found to be 97 and 92 MPa, respectively, exhibiting a harder surface compared to its sintered states. Mubarak et al. [13] investigated SLA printed acrylic-urethane resin and titanium dioxide (TiO_2). Among the tested samples, TiO_2 annealed at 800°C demonstrated a tensile strength of 47.43 MPa with an elastic modulus of 2.261 GPa, indicating improvements of 103% and 32% over pure SLA resin, respectively. Fig. 3(a) shows SLA/ TiO_2 tensile test results. Nagarajan et al. [14] investigated SLA printing of photopolymer composites. Strontium ferrite (SrFeO) and neodymium iron boron (NdFeB) powders were mixed with urethane acrylate resin. The SLA printed part resulted in improved tensile strengths (28.1 MPa in SrFeO and 22 MPa in NdFeB), yield points (10.1 MPa in SrFeO and 8.2 MPa in NdFeB), and elastic moduli (656.5 MPa in SrFeO and 536.7 MPa in NdFeB) based on tensile testing. The tensile test results are shown in Fig. 3(b).

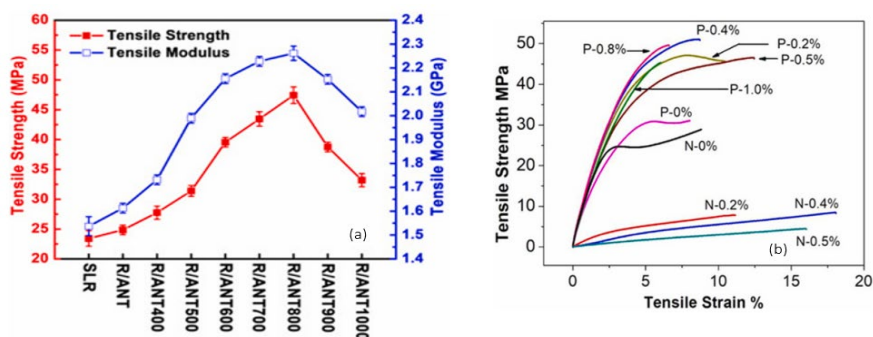


Fig. 3 (a) SLA/TiO₂ tensile properties [13], (b) SLA/lignin tensile properties [14].

Zhao et al. [15] presented a selection of photosensitive resins suitable for this purpose. Photo resin H-PSi-20 demonstrated its maximum elongation at a break of 1400%. As the silica content increased from 0% to 20%, tensile strength and elongation rose from 0.30 MPa to 2.59 MPa and 311%, respectively to DLP print silicon elastomers. Fig. 4 shows the DLP printed cat and honeycomb structures. Using the DLP method, Xiao et al. [16] investigated SiCN ceramic matrix composites using the DLP technique with a maximum tensile strength of 65.8MPa and maximum elastic modulus of 45 GPa.

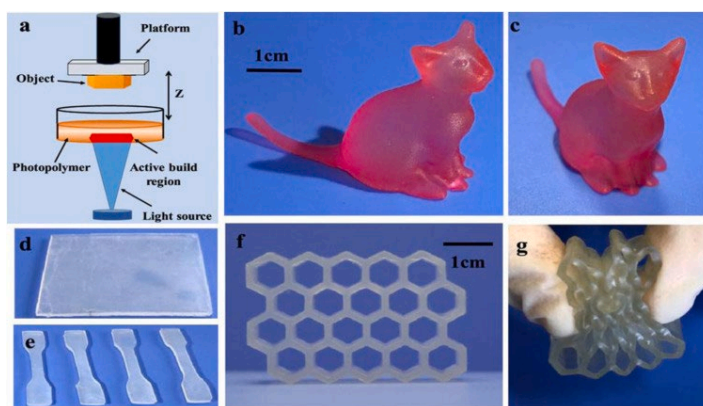


Fig. 4 (a) DLP method, (b, c) DLP printed cat, (d, e) DLP printed test specimens, and (f, g) DLP printed honeycomb structures [15].

Asif et al. [17] investigated carbon fiber and it was found that the single-layered specimen with the 1% concentration had a tensile strength of 2.78 MPa. This implies that

vat polymerization printed carbon fiber reinforcement materials have improved mechanical properties.

2.1.2. AM Technologies Based on PBF Process

PBF stands out as a highly versatile AM method, offering a range of material options such as metal, ceramic, polymer, and composites. The process involves selectively melting or fusing powdered materials using either a laser or an electron beam to 3D print part on a powder bed. [18]. Popular PBF technologies are: Selective Laser Sintering (SLS), Selective Laser Melting (SLM), Direct Metal Laser Sintering (DMLS), Selective Heat Sintering (SHS), and Electron Beam Melting (EBM) [18, 4].

In SLS, powders are scanned and fused using a laser beam. SLS is rapid and precise with superior quality surfaces with less material wastage requiring no jigs and fixtures. SLM process offers superior mechanical properties with the same process as SLS. SLM parts are highly sought after in aircraft, vehicle, and medical equipment applications. DMLS is also the same as SLS but uses metals rather than plastics. Metal powders are heated in the DMLS process to a temperature that allows them to combine to form a solid part, but not to the melting point. SHS melts plastic powder particles using a heated head that moves according to the sliced STL model. This method is widely favored for the manufacture of structural components. EBM melts the metal powder by using an electron beam [18, 4]. Fig. 5 shows the SLS, DMLS, and EMB technology.

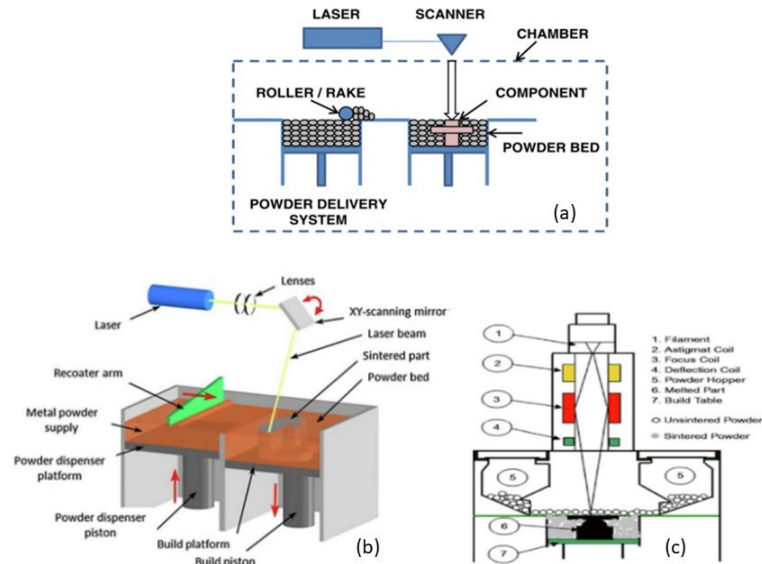


Fig. 5 (a) SLS process, (b) DMLS process, and (c) EBM process [18].

PBF technology, suitable for engineering and biomedical applications, has demonstrated remarkable capabilities [18]. Bewlay et al. [19] 3D printed Boeing 787 and 747–8 low-pressure airplane turbine blades using PBF, outperforming traditional methods with significant reductions in noise, fuel consumption, and NO_x emissions by 50%, 20%, and 80% respectively. PBF can 3D print a wide spectrum of alloys and their composites. H. Attar et al. [20] studied SLM printed Ti–TiB composites, revealing differences in density and compression properties between samples of 95.1% and 99.5% density. In Fig. 6, the compressive stress–strain curves for Ti–TiB composite samples at 95.1% and 99.5% density are depicted. The 95.1% density exhibits lower yield and ultimate strengths in comparison to the 99.5% density composites. Moreover, the compression strain is greater in the 99.5% density when compared to the 95.1% density. B. Zhang et al. [21] SLM

printed TiB_2 particle-reinforced Inconel 625 matrix composites. The results of compressive stress and strain are depicted in Fig. 6.

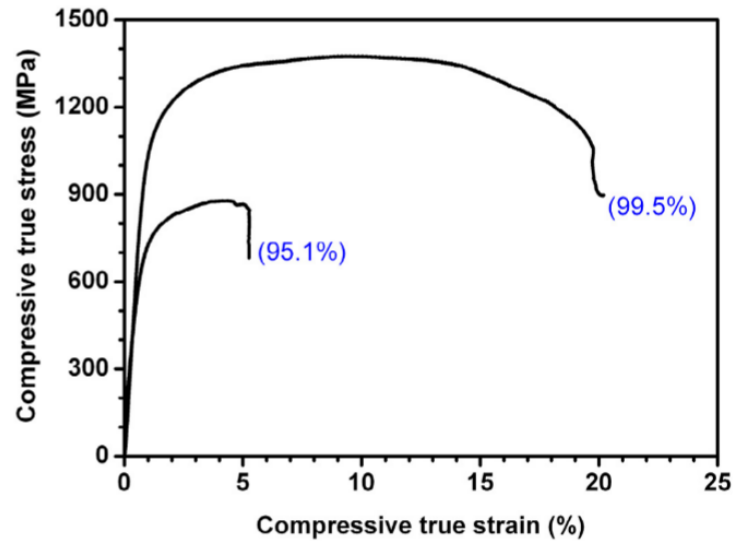


Fig. 6 SLM-printed Ti-TiB composites compressive true stress-strain curves [21].

Using a wide variety of materials, tuning part properties during processing, increased functionality, relatively low cost, and creating nearly net-shaped components ready for use are some of the biggest benefits of using PBF. However, PBF is a slow process due to the speed limitations of the process. PBF also has disadvantages such as severe size restrictions, high time and power consumption, excessive initial costs, and the generation of rough surfaces in the produced parts. Moreover, components may experience cracking in the manufacturing process if brittle or materials with elevated temperatures are utilized. This is because these materials are unable to endure elevated internal stress and need a more gradual cooling rate during printing [22].

2.1.3. AM Technologies Based on ME Process

The most popular AM technology is ME for its simplicity, cost-effectiveness, and applicability to various materials, making it suitable for both prototyping and manufacturing of objects in diverse industries. refers to a category of 3D printing techniques where Fused Deposition Modeling (FDM) is a common example of ME. FDM's raw material (filament) is heated and extruded through a nozzle in a controlled manner, depositing the material layer by layer to build the desired object [23]. Fig. 7 shows the typical demonstration of an FDM 3D printer. Currently, over half (51%) of AM products are crafted from polymer plastic filaments, contributing to the growing popularity of FDM. This method is compatible with various thermoplastic polymers, including but not limited to Polylactic acid (PLA), Acrylonitrile butadiene styrene (ABS), polypropylene (PP), Polyethylene terephthalate (PET), Thermoplastic polyurethane (TPU), Poly-ether-ketone (PEEK), Polyphenylsulfone (PPSU), High Impact Polystyrene (HIPS), and Acrylonitrile Styrene Acrylate (ASA) [24]. F. Ning et al. [24] demonstrated that the incorporation of carbon fiber into plastic materials resulted in enhanced tensile strength and Young's modulus. In particular, the carbon fiber composite specimen exhibited higher tensile and flexural properties. S. Woosley et al. [25] investigated FDM printed printed boron nitride nanocomposites, contrasting them with FDM-printed ABS samples to assess radiation shielding properties. The inclusion of 20% boron nitride in composite materials significantly enhanced neutron radiation shielding capability, increasing from 50% in pure ABS samples to 72%. This improvement holds the potential for mitigating neutron radiation source damage in aircraft parts manufacturing.

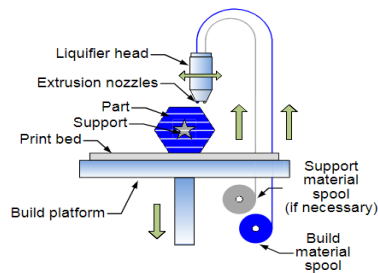


Fig. 7 Fused deposition modelling [24].

Three distinct glass fiber compositions and ABS matrix composites were studied by Zhong et al. [26]. The outcomes demonstrated that glass fiber may considerably increase the surface stiffness and tensile strength of the ABS filament. Another intriguing area for research is how fiber content affects the mechanical characteristics of printed objects. Wang et al. also reported similar, though not identical, work in which PEEK was combined with carbon fiber and glass fiber to create composite filaments, each of which had a distinct fiber composition [27]. In comparison to neat PEEK, both FDM printed CF with PEEK and GF with PEEK are stronger (GF with PEEK has performed better than CF with PEEK) [27]. As high-performance fibers carbon, glass, and Kevlar have been the subject of numerous research studies[28]. R. Zhang et al. [29] studied ultrasound assisted FDM 3D printed continuous glass fiber (CGF)/ PA6 composites and saw significant improvements in the tensile and flexural strength, as shown in Fig. 8. FDM printed glass fiber reinforced PLA/TPU composite parts were researched by L. Cao et al. [30]. The study involved investigating the effects of annealing and acetone vapor treatments on the parts. Post-processing treatments, by minimizing air gaps and voids on the morphological surface of fractured specimens. Fig. 9 shows the PLA/TPU SEM images.

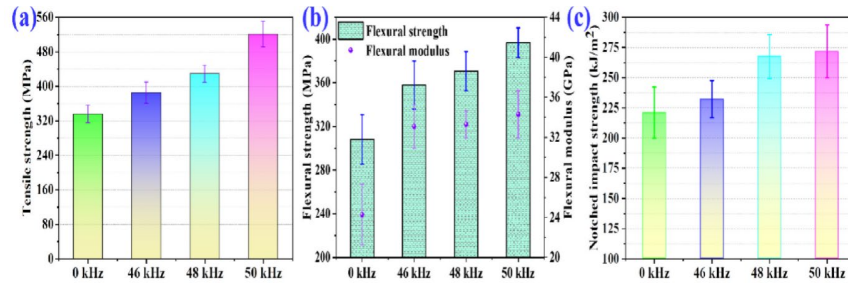


Fig. 8 Mechanical properties for FDM CGF/PA6 printing samples: (a) tensile properties; (b) flexural characteristics; and (c) impact strength [29].

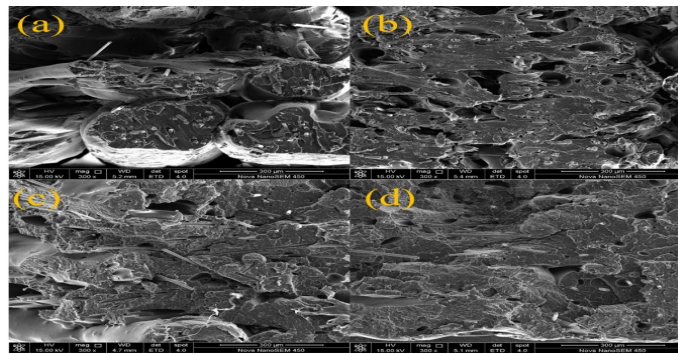


Fig. 9 SEM micrographs for FDM printed glass fiber reinforced PLA/TPU composites: (a) no treatment, (b) one-hour of acetone treating, (c) four hours of annealing, and (d) eight hours of annealing [30].

Direct Ink Writing (DIW) is another ME process wherein a small nozzle accurately deposits ink to create microscale 3D models [31]. Fig. 10 shows a typical demonstration of the DIW process. DIW will likely be at the cutting edge of additive manufacturing techniques due to the quick and can print using polymers, ceramics, metals, cement, alloys, and composites. Serra et al. [32] studied the use of polyethylene glycol (PEG) and G5 glass particles in DIW-printed PLA/bioglass 3D biodegradable scaffolds. Mechanical and bioactive properties significantly improved; however, PLA's lackluster mechanical properties have also restricted its use. To improve the mechanical properties of the resulting polymer composite, Zhang et al. [33] DIW printed PLA with hydroxyapatite (HA) which can be used to form human bones. Diogo et al. [34] DIW printed composite scaffolds

by mixing beta-tricalcium phosphate (β -TCP) with the natural biopolymer alginate obtained from seaweed. Using DIW, the authors precisely match a particular bone defect with scaffolds.

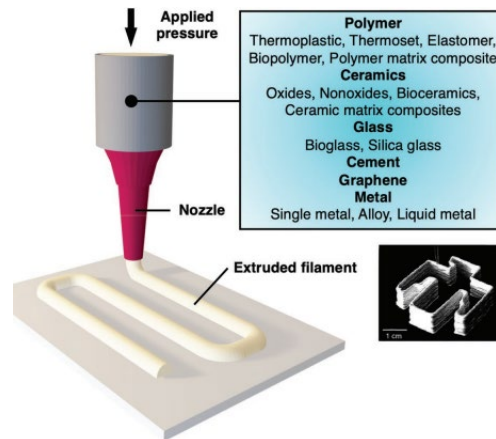


Fig. 10 Direct ink writing process [31].

Robertson et al. [35] DIW printed a complex crosslinked thermoset polymer Poly dicyclopentadiene (PDCPD) using frontal polymerization (Fig. 11a-i). Chandrasekaran et al. [36] used DIW to print well-architected structures using thermoset CE resins (Fig. 11a-ii). Guo et al. [37] used dissolvable thermoplastic polymer PLA to 3D print utilizing solvent cast DIW (SC-DIW) (Fig. 11b).

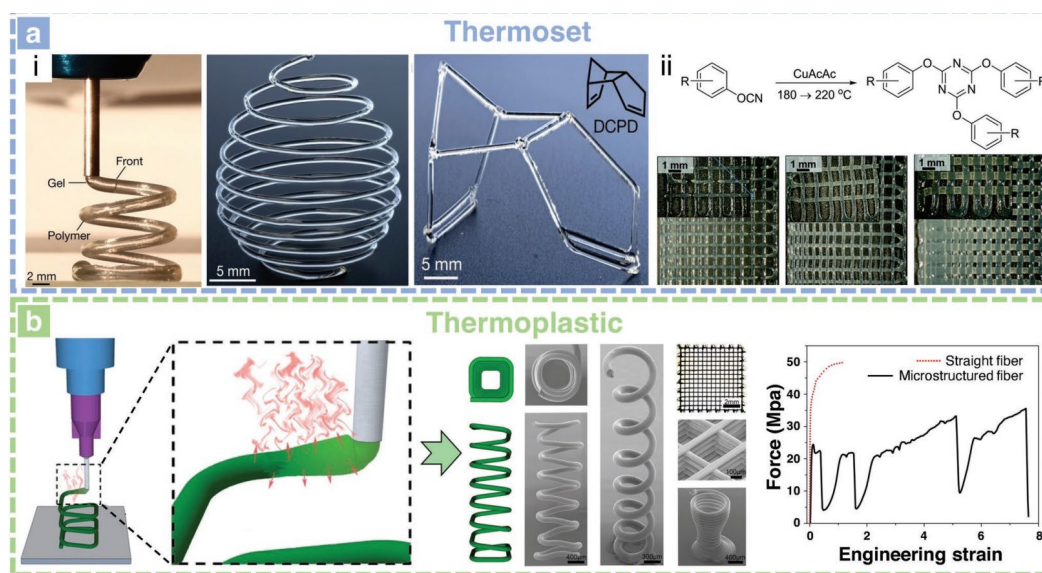


Fig. 11 (a) (i) DIW of gel PDCPD solution to create free-form 3D-printed structures [35], (ii) DIW printed structures of cyanate ester polymerization [36], and (b) SC-DIW printed parts mechanical properties [37].

2.1.4. AM Technologies Based on MJ Process

The MJ process selectively ejects liquid material droplets, which soften the deposited material layer and subsequently solidify through UV light exposure. The layer is removed from the build platform in one piece. The MJ process can be compared to a two-dimensional inkjet printer in many ways enabling multi-material printing that can print parts with smooth surfaces [38, 39]. The materials employed in the material jetting process are typically liquid thermoset photopolymers, such as acrylics, commercially available materials include fully transparent materials, rubber-like materials, resins, thermoplastics, waxes, reactive materials, and materials that resemble acrylonitrile butadiene styrene (ABS) [40]. MJ can provide high detail, precision, and a smooth surface finish, that can be utilized to print functional and non-functional prototypes. It is particularly favored for non-

functional prototype [41]. However, MJ's material is expensive, and the part properties are not significantly better than other AM techniques.

MJ's popular technologies are Drop on Demand (DOD), PolyJet by Stratasys, and NanoParticle Jetting (NPJ) by XJet. DOD utilizes two print jets, with one depositing build material and the other placing soluble support material. DOD can be used to print wax-like patterns used in lost wax casting and mold. PolyJet employs the deposition of ultra-thin layers, swiftly cured with UV light, and this sequence is reiterated to accomplish thorough curing. In NPJ, the build plate is coated with exceptionally thin layers of liquid nanoparticles through XJet technology [41]. Fig. 12 shows the MJ method and the printed part.

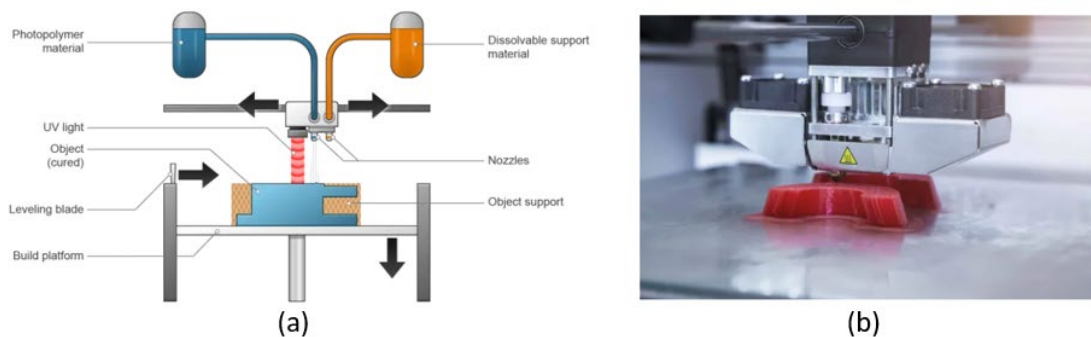


Fig. 12 (a) MJ working principle; and (b) MJ printing part [41].

Vdovin et al. [42] used photopolymer material in polyjet printing to create high-sound-absorbing acoustic samples. Kitamori et al. [43] used PolyJet printing to create a biocompatible resin mouthpiece. Using polyjet printers, thyroid cancer prototypes can be manufactured too [44].

2.1.5. AM Technologies Based on BJ Process

In BJ layers of powdered material, such as metal, ceramic, or plastic, are joined together to form solid objects [45]. Typically, a print head applies a liquid binder material to a layer of powder, fusing the particles to form a solid layer. The procedure is repeated layer by layer, with the print head depositing the binder material only where it is required, based on a digital model of the object being printed. The item is taken off the powder bed and the excess powder is cleaned up after the printing process is finished. To further strengthen and solidify the material, the object is frequently sintered or cured in an oven or other specialized machinery [45]. Figure 13(a) shows the schematic representation of the Binder Jetting Process. Compared to other techniques like laser sintering or fused deposition modeling (FDM), binder jetting is a relatively quick and affordable 3D printing process. In industrial settings, it is frequently used to create small to medium-sized components, including functional prototypes and intricate geometric shapes. However, it might not be appropriate for components that need a lot of strength or precision. BJ lies in its laser-free and low-temperature printing process, enabling the cost-effective production of large parts. BJ can print intricate structures without the need for support and accommodates a variety of powdered feedstocks [46]. With a higher build rate than MJ, BJ prints only a fraction of the entire object as a binder, achieving a component production rate of 200 cm^3 per minute with a 100-nozzle print head [47]. For metal items, BJ's high-build volume machines measure $780 \times 400 \times 400 \text{ mm}$ [48]. Despite these advantages, BJ-printed products exhibit suboptimal mechanical qualities, and the absence of sintering or melting options for structural reinforcement makes this method time-consuming and costly [45]. Fig. 13 shows the BJ method and printed part.

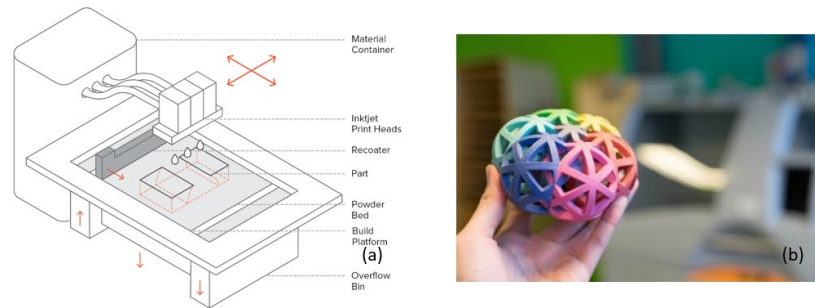


Fig. 13 (a) Binder jetting, and (b) sandstone made parts by binder jetting [49].

Q. Porter et al. [50] studied binder jetting made ceramic composites. The authors found the ceramic composites' compressive strength 826.0 MPa and the flexural strength 317.5 MPa. The results were better than those of any alumina-based specimens made via binder jetting. J. Liu et al. [51] incorporated TiO_2 particles into cement-based materials for binder jet 3D printing. The outcomes showed a superb filling effect that boosted hydration and densified the printed specimens, increasing their compressive strength. Furthermore, the filling and catalytic effects of larger TiO_2 particles can manufacture customized and environment-friendly highly functionalized structures with good strength. Kazi et al. [52] investigated that in binder jetting using post-process sintering, shell printing significantly affected green part density increase by 3.7%, 5% final part density increase, 290% increase in grain size, and tensile strength increase of 8.84% when compared to conventional strategies of homogeneous binder placement. This was discovered using pure copper and analyzing parts with varying shell thicknesses.

2.1.6. AM Technologies Based on DED Process

DED melts and fuses materials together by a laser to 3D print a part layer after layer. Usually, DED melts a metal powder or wire to a substrate or previously printed layer using a nozzle or another delivery system to begin the process. In the DED procedure, the energy source heats and melts the substance as it is being deposited, forming a molten pool that solidifies as the energy source travels along the desired path. DED can produce parts with intricate geometries and substantial material densities by precisely controlling the energy source and material feed. DED can do quick transitions between different materials to enable multi-material printing [53]. DED is a flexible process that can use metals, alloys, ceramics, composites, tantalum, titanium, stainless steel, aluminum, and cobalt as metal powders. It is frequently used to produce inexpensive intricate, high-performance parts as well as for prototyping and repairs in the aerospace, defense, and medical industries. Nevertheless, challenges arise in DED due to complexity and the growing surface roughness, necessitating post-processing to mitigate residual stress [53].

There are several types of DED processes like Powder-fed DED (PFDED), Wire-fed DED (WFDED), Blown powder DED (BPDED), and Directed light fabrication (DLF) which differ in the delivery and deposition of the material [54]. PFDED delivers powders and WFDED delivers a wire material using an electron beam [54]. Wire and arc additive manufacturing (WAAM) is a WFDED process that uses wire as a filament [55]. Popular WAAM methods are gas metal arc welding (GMAW), gas tungsten arc welding (GTAW), and plasma arc welding (PAW) [56]. GTAW or PAW allows for material deposition at twice the speed compared to GMAW. However, GMAW is less stable due to the influence of electric current on the feedstock. These processes utilize co-axial and off-axis feeding.

Despite these benefits, they exhibit drawbacks such as low repeatability, insufficient adaptive control, accumulative error, and reliance on expensive post-processing technologies [57]. Fig. 14 shows all the DED processes.

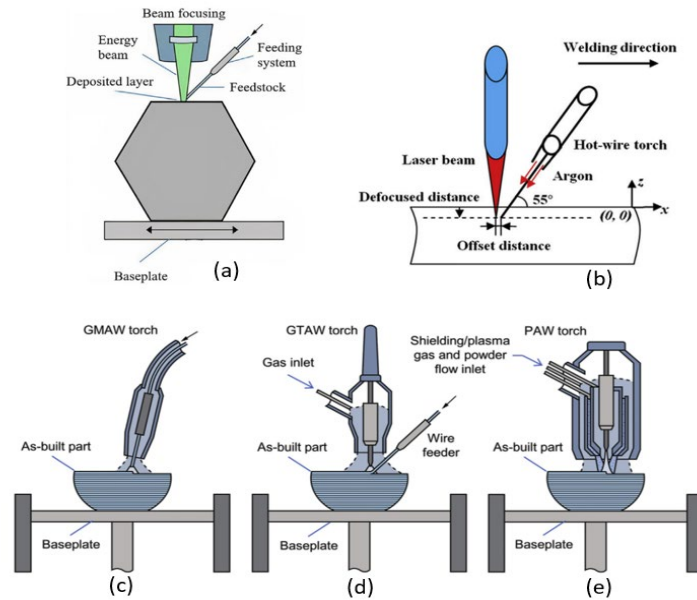


Fig. 14 (a) Basic DED process, (b) WFDED process, (c) GMAW process, (d) GTAW process, and (e) PAW process [56, 57].

In BPDED, a powder material is delivered through a high-pressure gas stream, such as nitrogen or argon. DLF delivers photocurable material and solidifies using a high-intensity light source, such as a UV laser or LED [54]. Depending on the application and materials being used, each of these DED processes has unique benefits and drawbacks. For instance, large metal parts are frequently built using PFDED, whereas existing parts can be repaired or upgraded using WFDED. DLF is excellent for 3D printing minute and intricate parts [54].

Rombouts et al. [58] investigated the effects of loading Inconel 625 in either a horizontal orientation or a vertical orientation. The results demonstrated that the produced Inconel 625 in the casting and annealing process had higher elongation but lower tensile

strength at a low cooling rate compared to both directions in laser metal deposition (LMD) due to the good heat conduction away from the interaction zone. Wilson et al. [59] repaired and remanufactured turbine blades and by repairing 10% of the entire part, the carbon footprint was increased by 45% and energy was saved by 36%. In DED, Saboori et al. [60] discovered that maintaining a laser's power while increasing the rate at which powder is fed improved the mechanical and surface qualities and that selecting the right nozzle-to-substrate distance was crucial for successful material deposition.

2.1.7. AM Technologies Based on SL Process

In SL, 3D parts are formed by stacking and connecting sheet materials atop each other. LOM serves as an illustration of this process, allowing the efficient fabrication of large parts at a generally lower cost compared to other AM technologies. Various polymer and polymer-based composite materials are attracting researchers' attention in implementing LOM. Using a commercial SD 300 Pro LOM 3D printer, Pilipovic et al. [61] studied LOM printed PVC parts. Tensile and flexural properties were evaluated on specimens 3D printed in the x, y, and z directions. The study revealed that polymer sheets outperformed paper as a feedstock material in LOM, exhibiting significantly enhanced mechanical properties and expanding the technology's potential applications.

ABS and thermoplastic polyurethane (TPU) polymers were used in Kumar et al.'s [62] utilized ABS and thermoplastic polyurethane (TPU) polymers in the LOM manufacturing of flexural test samples. FDM printing was initially employed to create two types of sandwich specimens (ABS-TPU-ABS (ATA) and TPU-ABS-TPU (TAT)) using different polymer filaments. Both TAT and ATA samples demonstrated higher flexural strengths than TAT composites, with a 92% increase from 6.8 MPa to 13 MPa. The authors

suggested potential applications for these sandwich-structured composites. Chang et al. [63] used continuous carbon fiber-reinforced thermoplastic composites (CF/PA6 prepregs) in the LOM 3D printing process. Laser-cut prepreg plies were consolidated using an ultrasonic roller, and the 3D-printed composite parts exhibited superior unidirectional tensile strengths of 1760.2 MPa and tensile moduli of 105.7 GPa. Krinitcyn et al. utilized the LOM process to manufacture a three-dimensional gear with a linear shrinkage of less than 3%. LOM-manufactured polymers and composites hold significant promise for load-carrying structural components across various industries. Fig. 15 shows ultrasonic assisted LOM printed parts.

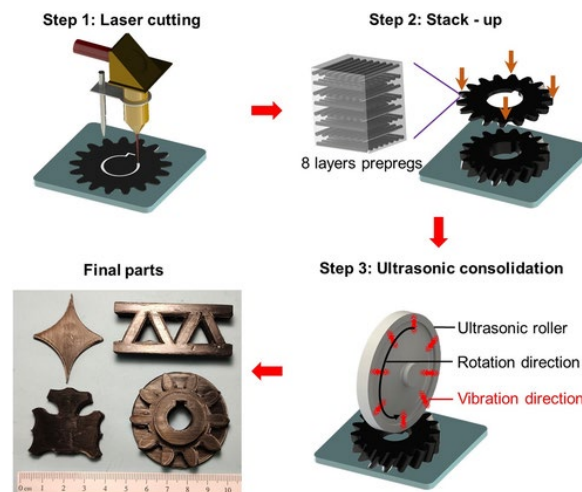


Fig. 15 Ultrasonic assisted LOM process and printed parts [63].

The LOM process does not entail chemical reactions and does not require support material, as the laminated material self-supports during curing before the final component is cut [64]. Complex geometric shapes are challenging to produce with LOM because of the difficulty in accessing the interior of a part and removing excess material. Moreover, LOM's dimensional accuracy has room for improvement. Parts manufactured with LOM

may exhibit low strength and subpar surface finish, particularly depending on the chosen material. Additionally, materials such as paper can absorb moisture if not treated [64].

2.2 Background Information on AM of Biocomposites

Abaca, bamboo, coir, flax, grass, hemp, jute, kenaf, ramie, sisal, and sugarcane are the most prevalent and readily available commercial biofibers worldwide [65]. A matrix, typically polymers and a biofiber reinforcement are combined to create biocomposites. Biocomposites are gaining interest in research and industrial applications of vehicles, aerospace, military equipment, construction, sports, and packaging. Biofibers possess qualities such as renewability, recyclability, cost-effectiveness, environmental friendliness, and biodegradability [65, 66].

2.2.1 ME Process Based Biocomposites

In the process of material extrusion, fused deposition modeling (FDM) can be used to manufacture biofiber reinforced polymer composites. There are two processes by which we can manufacture this: 1) Polymer pellets and chopped fibers can be blended in a mixer and subsequently fed into an extruder, where they are transformed into filaments for the production of biofiber composites, and 2) prepreg composite filaments made from continuous biofiber can also be directly extruded for 3D printed parts after being infused with or coated with polymer paste [67, 68]. In a composite part, two of the most important factors are fiber orientation and void fraction of composites. The higher fiber content reinforced biocomposites process is difficult as continuous filaments with high fiber for FDM are hard to manufacture and can't be printed due to nozzle clogging issues [67].

Correa et al. [69] developed a 4D printing method using FDM with filaments made from wood fibers and polymers. The wood FDM filaments were placed with exacting

precision to manage the anisotropic characteristics of the material by establishing specific grain patterns. Montalvo and Hidalgo [70] studied FDM with compound filaments using different plastic matrices and sugarcane bagasse as the filler, varying fiber and polymer amounts to analyze the composites. The FDM process can be used to produce biocomposites with a PLA/PHA matrix reinforced with recycled wood fibers [71]. The study revealed improved strength for extruded or injection molded PP with wood and HDPE with wood. Matsuzaki et al. [72] FDM printed continuous fiber reinforced composites (CFRPs). The authors concluded that the tensile strength of jute reinforced biocomposites was not improved significantly compared to that of carbon fiber ones. Using hemp and harakeke (phormium tenax) with PLA matrix, Stoof et al. [73] investigated the use of FDM to create natural fiber-reinforced composite components. According to their findings, 20 weight percent harakeke samples had a tensile strength that was 5.4% higher and Young's modulus that was 42.3% higher than plain PLA samples. Additionally, using pre- or post-consumer PP, they created composite filaments with various weights of fiber and gypsum and discovered that the tensile strength and Young's modulus of the filaments manufactured from harakeke in a PP matrix were significantly higher than pure PP. Furthermore, the authors showed PP with natural fiber had better properties than PP with glass fiber [74].

The study by Navarrete et al. [75] investigated the feasibility of using FDM to produce wood flour-reinforced polymer composites (WPCs). Four different concentrations of wood were used by the authors along with two different PP and PLA matrices. The 20% wood flour content that they discovered was best for the FDM process. After creating filaments from the 20% wood flour composites, the authors printed tensile and flexural test

samples and compared them to samples made by injection molding. The outcomes demonstrated that the samples produced using FDM printing had lower tensile and flexural moduli than those produced using injection molding. Kariz et al. [76] used Liquid Deposition Modeling (LDM) to mix the wood powder with polyvinyl acetate and urea-formaldehyde. The authors observed part shrinkage due to water removal during curing, with the largest shrinkage in the z-direction. However, wood increased the extrusion power. Rosenthal et al. [80] used sawdust and methylcellulose as the binding agent for LDM 3D printing. They used 0.25mm and 0.4mm sawdust particles and mixed them with methylcellulose and water to achieve good dimensional stability and bending properties. Fig. 16 shows all the mechanical properties of these FDM printed specimens.

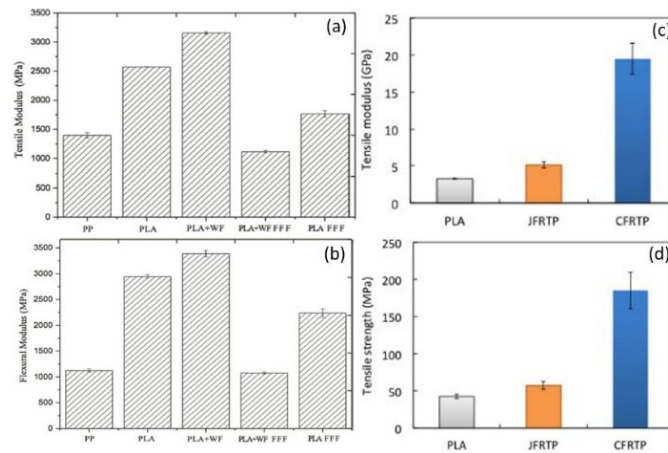


Fig. 16 PP, PLA, PLA+WF, FDM printed PLA+WF, and pure PLA (a) Tensile Modulus, (b) Flexural Modulus [75, 77], PLA, JFRTP, CFRTP, (c) Tensile Modulus, and (d) Tensile Strength [72, 77].

2.2.2 PBF Process Based Biocomposites

The SLS process is mostly used to print biofiber reinforced composites. Guo et al. [78] used wood and copolyester (Co-PES) powder with a viscosity reducer to form a wood/plastic composite using the SLS process. The volume ratio of wood to Co-PES

powder was 10:9. These parts obtained adequate strength and wax infiltration was used to drop in void fraction from 51% to 7% and a notable improvement in mechanical properties and part quality. Zeng et al. [79] used rice husk powder to make rice husk plastic composites (RPCs) through the SLS process. RPCs significantly improved mechanical properties compared to wood plastic composites (WPCs) made using the same process. RPCs had 2.6 times the bending strength, 10.7 times the tensile strength, and 78% the impact strength of WPCs. The mechanical properties of RPCs were further enhanced by wax post-processing, which led to tensile strength values of 1.47 MPa, bending values of 3.86 MPa, and impact values of 3.74 kJ/m², which are, respectively, 21%, 41%, and 165% higher than those of the WPCs. Fig. 17 shows these results.

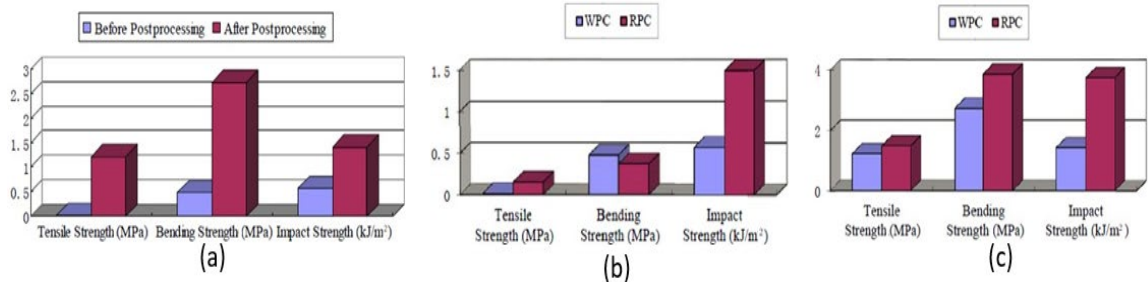


Fig. 17 Comparisons of mechanical properties: (a) SLS-printed WPCs [78, 77], (b) SLS-printed WPCs and RPCs [79, 77], and (c) SLS-printed wax-infiltrated WPCs and RPCs [79, 77].

Xin et al. [80] used aspen wood powder, adhesive powder, and polypropylene (PP) powder for SLS printing of biocomposites. Because there was inadequate wood and plastic bonding, the authors varied the wood powder content from 10% to 40% and discovered that doing so adversely affected the tensile and flexural strengths. The base material contained no combining agent, and the wood powder's particle size ranged from 80-100

μm . The PP powder ranged in size from 100-180 μm , while the hot-melt adhesive powder had a size of 120-180 μm .

2.2.3 VP Process Based Biocomposites

Two of the most used vat polymerization techniques to create biocomposites are SLA and DLP. Quan et al. [81] SLA printed with different fibers to improve the strength and toughness of printed parts. UV lighting projectors were used with the same light intensity while using carbon, glass, or high-strength PE (HSPE) yarns. The use of different fiber yarns with the same resin resulted in significantly improved elastic modulus and tensile fracture strength compared to parts made from pure resin. HSPE yarn reinforcement was better than both glass fiber and carbon fiber. The use of biofibers in SLA 3D printing is an area that requires further research and development. Fig. 18 shows the results of this study. Li et al. [82] utilized DLP technology to create glycerol composites reinforced with cellulose nanocrystals, improving strength and observed a positive correlation between cellulose nanocrystals concentration and Young's modulus, as well as a decrease in Young's modulus with increasing 3D printing layer thickness.

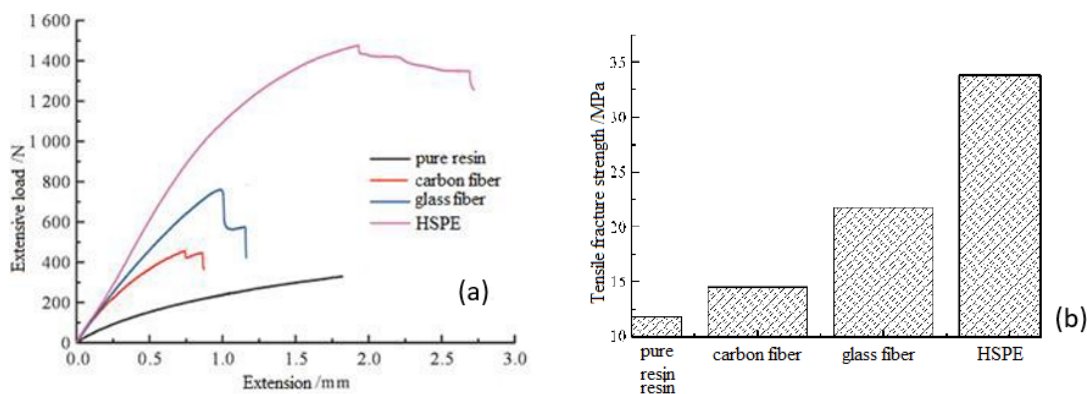


Fig. 18 (a) Tensile Test Curves, and (b) Tensile Fracture Strength of Pure Resin, CF, GF, HSPE [77, 81].

2.2.4 SL Process Based Biocomposites

LOM is the 3D printing process that is mostly used to create biocomposites. LOM technology is inexpensive, accurate, and has high fiber content and short building time. Jiang et al. [83] examined pure resin and woven jute fiber-reinforced composites. The results showed that both types of pure resin were relatively weak, with hydrovanilloin resin being very brittle. However, incorporating woven jute fibers into the resins significantly improved their tensile and flexural properties. The maximum tensile strength was 28.32 MPa for woven jute fiber reinforced Elixir resin, and the maximum tensile modulus was 2.68 GPa. The maximum flexural strength was 39.66 MPa for 3-ply woven jute fiber reinforced Elixir resin, and the maximum flexural modulus was 2.72 GPa. The results of this study suggest that LOM can be used to produce high-strength composite materials from natural fibers for rapid prototyping applications. Fig. 19 shows the results.

Weisensel et al. [84] utilized the reaction bonding technique to develop a LOM product by binding a paper and adhesive made from ethanol, polyvinyl butyral, benzyl butyl phthalate, and phenolic resin. After being pyrolyzed once more to turn the phenolic resin into carbon, the product was then post-infiltrated with liquid Si. The composite's average bending strength was 130 ± 10 MPa after 1 hour of infiltration which is comparable to other 3D-printed SiC materials.

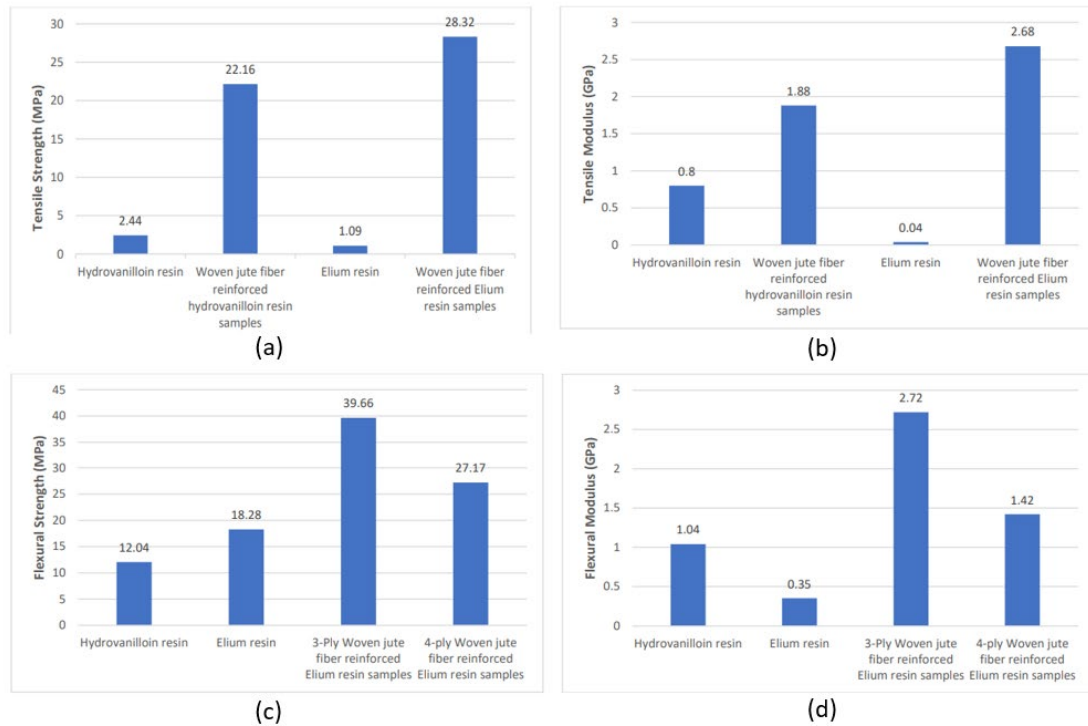


Fig. 19 Comparison of: (a, b) tensile, and (c, d) flexural properties of hydrovanilloin, elium and jute/hydrovanilloin and jute/elium samples [83].

Composite-Based Additive Manufacturing (CBAM) is another solid-sheet-based 3D printing technology that applies a fiber sheet with glue using an inkjet technique. Following that, the polymer is coated on the sheet, adhering to the sheet where the glue was printed. Once the excess powder has been taken out, the procedure is repeated until all the sheets have been stacked. The desired part is then made visible by removing the unbonded sheet fiber portions using mechanical or chemical processes after the entire component has been heated and compressed for consolidation. Impossible Objects [85], a company based in Northbrook, Illinois, uses the CBAM technology to produce complex and strong 3D printed parts at a faster rate than conventional processes. This company used Kevlar, carbon, and glass to achieve tensile strength of up to 150 MPa and tensile modulus of up to 11.0 GPa for their carbon-nylon parts and these parts are better than FDM printed

nylon [86]. Fig. 20 shows the CBAM working principle and CBAM printed parts properties.

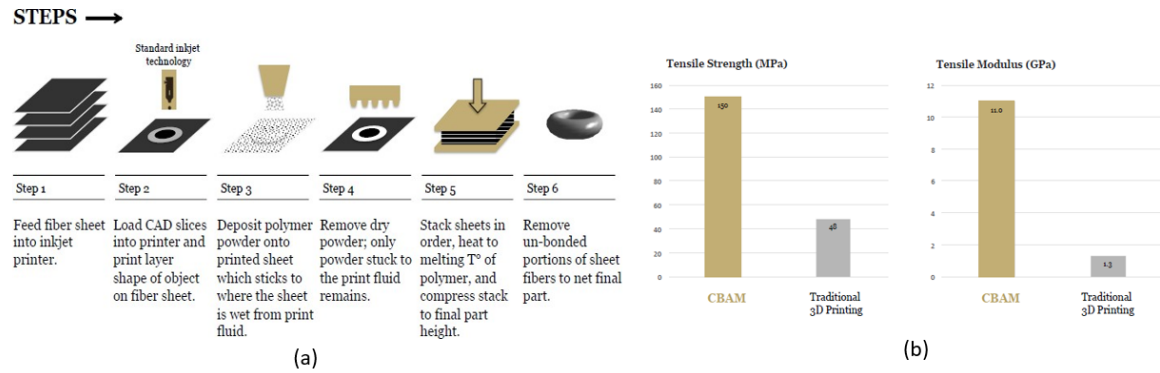


Fig. 20 (a) CBAM working principle, and (b) CBAM printed carbon-nylon comparison with FDM printed carbon-nylon [86].

2.3 Mechanical Properties of Natural Fiber Reinforced Composites

Various studies have investigated the use of natural fibers like bamboo, banana, hemp, jute, kenaf, pineapple, rice straw, sisal, sugar palms, sugarcane, and wood. as reinforcements in polymer matrices [87, 88, 89]. Different mechanical characteristics can be seen in different natural fibers. Composite materials based on cotton have demonstrated improved eco-efficiency and a decreased negative impact on the environment [90]. Bamboo fibers, which are famous for their woven structures, exhibit special qualities in terms of fiber displacement responses, matrix failures, and fracture features [91]. Heat-insulating compounds and acoustical absorbing substances are increasingly using natural fibers in 3D printing filaments [92]. Natural fiber composites have lower wear resistance than synthetic fiber composites. For this reason, natural fiber composites are suitable for applications in the automotive industry, particularly in automobile components subjected

to wear [91]. Depending on the kind of natural fiber used, the wear behavior of composites made from natural fibers varies.

Natural fibers with higher modulus and tensile strength typically have better wear resistance. The wear behavior of natural fiber composites is also significantly influenced by the fiber matrix bonding. These natural fibers can be shielded from wear and damage by a strong fiber matrix bond [91]. Longer natural fibers have a higher wear resistance than shorter fibers because they are less likely to break off during use. Additionally, the amount of fiber in natural fiber composites offers more protection for the fibers against deterioration, materials with higher fiber contents tend to be more wear-resistant than those with lower fiber contents. Moreover, by giving the fibers a chemical treatment that increases their wear resistance, Hybridization which is the process of combining two or more different types of fibers in a composite can also increase the composites' properties and wear resistance [91]. Natural fiber reinforced composites can show the exact mechanical properties of synthetic fiber reinforcements (glass and carbon fibers). This can be done by varying factors like fiber geometry, density, and chemical structure, as well as farming conditions [93]. By incorporating nanoscale fillers and gathering precise mechanical property data, the use of computer simulations, and advanced measurement techniques these adjustments can be made. Fig. 21 shows the natural fiber composition. Table I shows the properties of the popular natural fibers available.

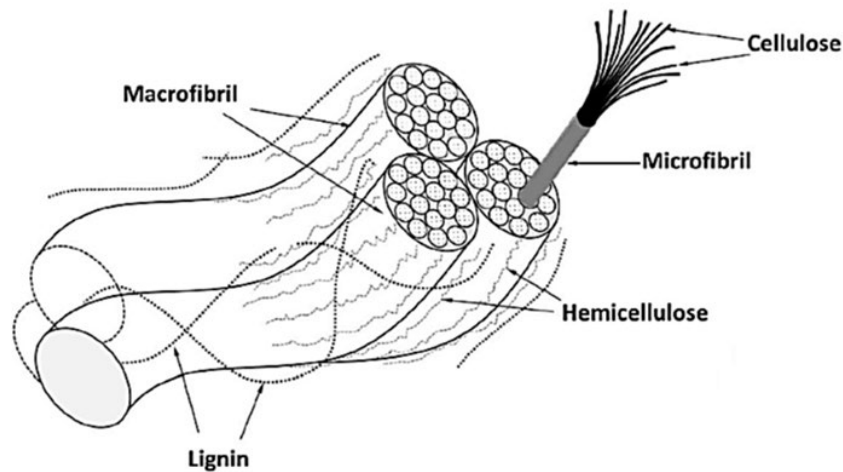


Fig. 21 Schematic of natural fiber composition [94].

Many natural fibers derived from plants, including flax, hemp, and jute, have superior mechanical qualities and a lower density than glass fibers. The mechanical properties of natural fibers can vary, though, depending on the plant variety, growing environment, processing, and measurement techniques. Natural fibers can achieve similar or even higher specific stiffness values than glass fibers, despite having a potentially lower tensile strength. Table II shows the comparison between E-Glass fiber and natural fibers. In comparison to other plants, flax and hemp have the benefit of requiring less space to be grown. For instance, flax exhibits a significantly higher yield than other plants [95]. Environmentally speaking, growing natural fibers like flax are preferable to manufacturing synthetic fibers like glass fibers and even other textiles like cotton. In comparison to cotton fibers, which need 700–29,000L of water per kg to produce, flax fibers only need 600–1000L [96].

TABLE I
NATURAL FIBER PROPERTIES [94, 97]

Fiber	Density (g/cm ³)	Tensile Strength (MPa)	Tensile Modulus (MPa)	Elongation at Break (%)
Sugar palm	1.30	15.5–290	0.5–3.4	5.7–28
Sisal	1.50	400–700	9.0–38.0	2.0–14.0
Oil palm	1.55	400	9.0	18.0
Jute	1.60	393–800	10.0–30.0	1.2–1.8
Kenaf	1.45	930	53.0	1.6
Hemp	1.48	550–900	70.0	1.6–4.0
Cotton	1.60	287–800	5.5–12.6	2.0–10.0
Bamboo	1.25	290	17.0	-
Flax	1.50	345–1500	27.6	1.2–3.2
Pineapple	1.44	413–1627	60.0–82.0	14.5
Banana	1.35	529–914	27.0–32.0	5.9

TABLE II
COMPARISON OF PROPERTIES OF E-GLASS FIBER TO NATURAL FIBERS [98]

Property	E-Glass	Flax	Hemp	Jute
Density (g/cm^3)	2.5	1.5	1.5	1.3-1.5
Length (mm)	Continuous	5-900	5-55	1.5-120
Tensile strength (MPa)	2000-3000	345-1830	550-1110	393-800
Specific tensile strength ($\text{MPa}/\text{g}\cdot\text{cm}^{-3}$)	800-1400	230-1220	370-740	310-610
Tensile stiffness (GPa)	70	27-80	58-70	10-55
Specific tensile stiffness ($\text{GPa}/\text{g}\cdot\text{cm}^{-3}$)	29	18-53	39-47	7.1-39

Ahmad et al. [97] developed composite filaments with varying weight percentages of oil palm fiber (0%, 3%, 5%, and 7%). The fibers were cleaned by soaking in water for two days and sodium hydroxide was used to avoid unwanted components. On the other hand, Nasir et al. [94] applied silane and alkaline treatments to sugar palm fiber composites. After three hours in the solution, the fibers were distilled water-rinse, and woven-dried. Natural fiber-reinforced thermoplastic filaments can be used in FDM, and Fig. 22 shows the fundamental steps involved in creating these composite materials. Han et al. [99], Yu et al. [100], and Tao et al. [101] developed natural fiber composite filaments: kenaf/ABS, astragalus/PLA, and wood/PLA respectively for FDM 3D printing (Fig.23). Muck et al. [102] made filament combining wood and PLA. The authors showed that this filament had

gaps between the fiber and the matrix generating a low interfacial bonding between the PLA matrix and wood fiber. Fig. 24 shows the SEM images of this study.

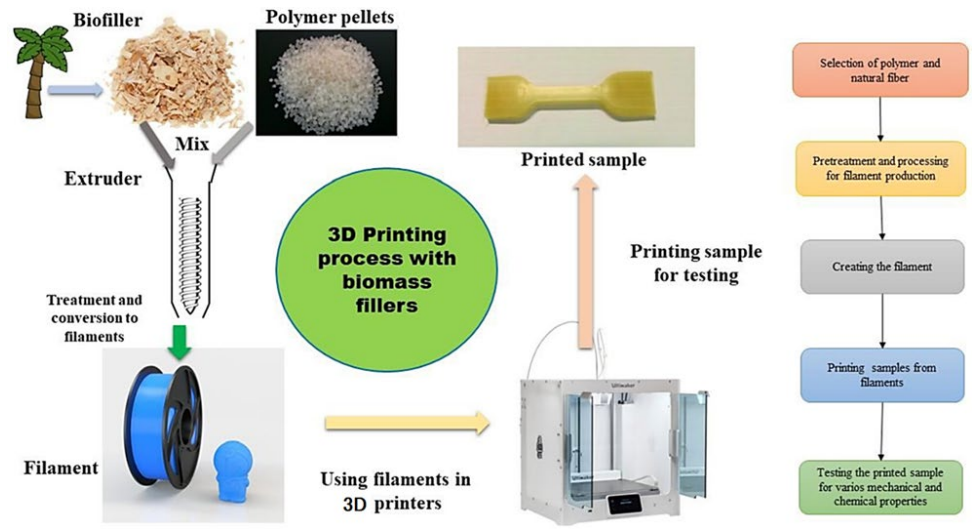


Fig. 22 Manufacturing steps required to produce biocomposite filaments [103].

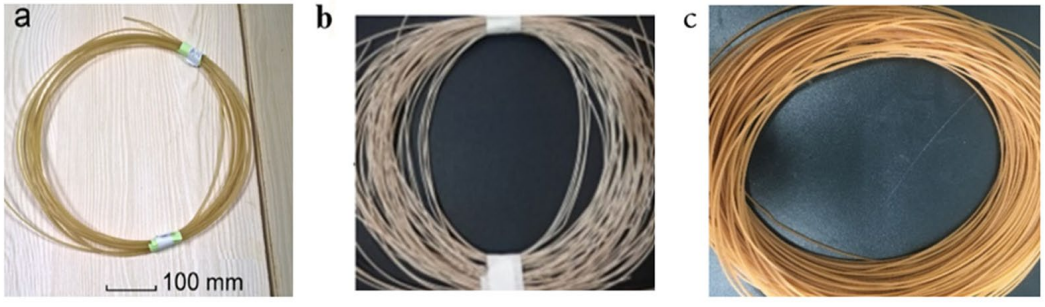


Fig. 23 (a) PLA reinforced wood, (b) ABS reinforced kenaf, and (c) PLA reinforced astragalus biocomposites filaments [99, 100, 101].

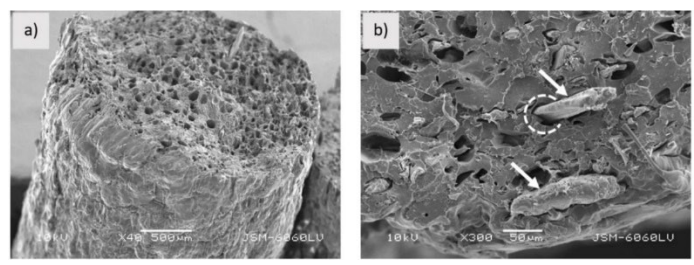


Fig. 24 SEM images of wood and PLA (a) 500 μm, and (b) 50 μm [102].

Stoof et al. [73] 3D printed composite samples reinforced with natural fibers using fused deposition modeling (FDM). They mixed different weight percentages of consistent

3 mm hemp and harakeke (phormium tenax) filaments in a PLA matrix. In comparison to plain PLA samples, the FFF samples with 20 weight percent harakeke displayed higher tensile properties. according to the results of their tests. Additionally, using pre- or post-consumer PP (polypropylene). Furthermore, Stooft et al. investigated FDM printed composite filaments with different weight contents of fiber and gypsum using pre- or post-consumer PP (polypropylene). High tensile properties are observed using 30% weight of PP with harakeke [74].

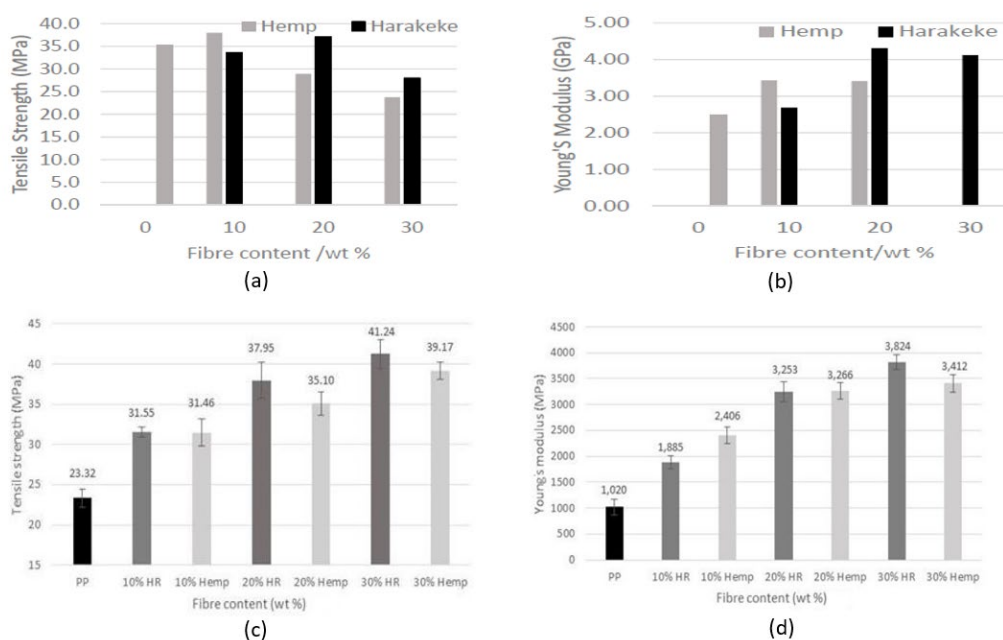


Fig. 25(a) Hemp/Harakeke mixed with PLA tensile characteristics, (b) Hemp/Harakeke mixed with PLA Young's modulus, (c) PP/harakeke and PP/hemp tensile properties, and (d) PP/harakeke and PP/hemp Young's modulus [74, 73].

Rahman et al. [104] highlighted the importance of filler selection and fiber loading in optimizing the jute fiber-reinforced polyethylene properties, emphasizing the role of interfacial bonding and compatibility between the components. The authors examined the effects of clay, silica, and maleic anhydride (MA) fillers on jute fiber polyethylene (PE)

composites. The preparation of various composite formulations included silica- and MA-based composites as well as those treated with MA, clay, or both. Clay served as a reinforcement filler, silica improved elongation characteristics, and MA improved the hydrophobic properties of PE. Jute fiber and PE mixtures were molded and heat-pressed under specific circumstances to create the composites. The results demonstrated that up to a 15% fiber loading percentage, the tensile strength and Young's modulus increased. However, these characteristics decreased at a reinforcement weight of 20%. Weak interfacial bonding, lower compatibility, and a higher level of fiber agglomeration within the matrix were blamed for this decrease. Notably, the composite's tensile strength significantly increased because of the addition of MA and silica. Additionally, samples with MA, silica, and clay showed the highest Young's modulus, demonstrating improved compatibility between the fiber and matrix. At higher fiber weight percentages, the researchers found that agglomeration of the fiber within the matrix was to blame for the decline in tensile strength and Young's modulus. Fig. 26 shows the SEM study that was done in the study to investigate the fracture surfaces of these biocomposites and the tensile strength and Young's modulus at various fiber loadings.

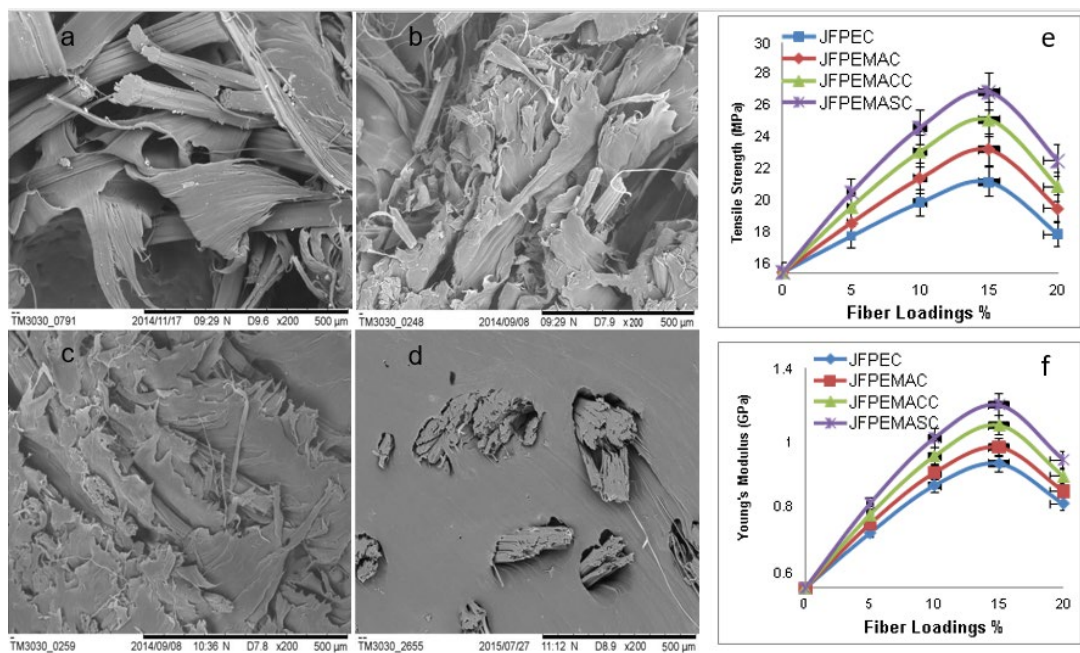


Fig. 26 SEM images of composites: (a) jute fiber with PE, (b) jute fiber with PE and MA, (c) jute fiber with PE and MA clay, (d) jute fiber with PE and MA silica; (e) tensile properties comparison, and (f) comparison of Young's modulus [104].

Rassiah et al. [105] used the hand lay-up technique to prepare compositions of woven bamboo with 2 layers and strip bamboo fiber with thicknesses ranging from 1.5 to 2.5 mm in a 3 mm thick mold. The outcomes showed that the woven bamboo-reinforced epoxy composite had superior properties to the strip bamboo-reinforced polyester composite. Comparing the woven bamboo composite to the strip bamboo composite, the tensile modulus, hardness, flexural strength, and tensile strength of the woven bamboo composite were all higher, ranging from 11.4% to 45.1%. The flexural modulus in the woven bamboo composite, however, displayed the opposite trend, declining by 13.5%. According to these findings, the woven bamboo-supported epoxy composite has excellent mechanical qualities and stands as a useful substitute for traditional composites.

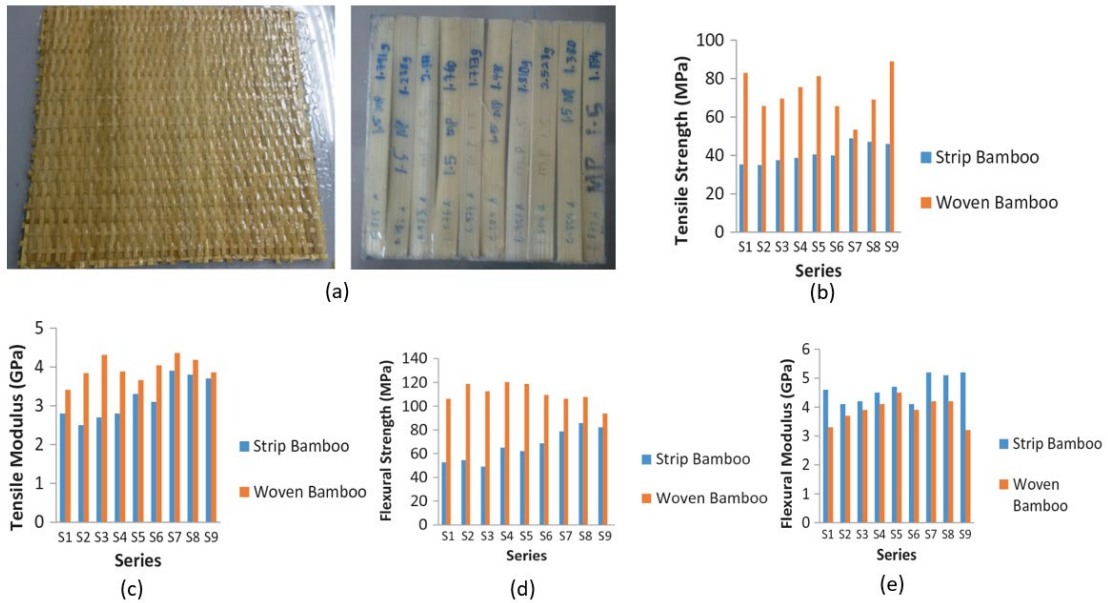


Fig. 27(a) Laminated woven bamboo and strip bamboo samples, (b) tensile strength, (c) tensile modulus, (d) flexural strength, and (e) flexural modulus [105].

To achieve the best tensile strength possible in jute fiber-reinforced polypropylene composites, Chatterjee et al. [106] emphasized the significance of choosing the proper fiber lengths and plies and focused on how thermal processing may affect the mechanical characteristics of composites. The authors concentrated on creating composites that are environmentally friendly by adding jute fibers to a polypropylene (PP) matrix. By varying the fiber lengths (3 cm, 6 cm, and 9 cm), number of plies (1, 2, or 3), and loading percentages (0%, 5%, and 10%), the researchers looked at the mechanical characteristics of the composites. The optimal tensile strength was with a fiber length of 3 cm and two plies, across all weight ratio percentages. However, the strength decreased when four plies of jute fiber were used. Table III shows the tensile strength values of jute/polypropylene composites with different plies and loading percentages.

TABLE III
JUTE FIBER CUT LENGTHS ON THE TENSILE STRENGTH (MPa) OF JUTE
FIBER COMPOSITES [106]

Fiber concentration	3cm jute fiber			6cm jute fiber			9cm jute fiber		
	1ply	2ply	4ply	1ply	2ply	4ply	1ply	2ply	4ply
0%	5.23	7.21	6.23	5.23	7.68	6.49	6.02	7.59	6.92
5%	10.44	12.01	11.54	10.09	11.88	10.16	9.68	11.36	10.34
10%	10.23	17.86	12.47	10.21	13.48	12.16	9.92	13.65	11.93

Jiang et al. [107] introduced a novel approach to manufacturing biocomposite sandwich structures consisting of a natural fiber textile (such as jute, flax, and cellulose) as the skin, mycelium-bound agricultural waste as the core, and a bio-resin as the matrix. A natural binder for biocomposite materials can be made from mycelium, the vegetative portion of a fungus made up of thread-like hyphae. It can colonize reinforcement fibers and core material without the need for additional energy input by ingesting and adhering to damp agricultural byproducts. The core materials for sandwich structures are natural fiber reinforcement and organic waste; a web of threadlike cells, resembling mushroom roots, connects them to create laminates. A two-piece growth mold set was created using heavy gauge plastic, featuring an enclosed cavity for the brick specimen and respiration holes to facilitate fungal growth. After sterilization, the molds were filled with various core, reinforcement, and mycelium binder materials. The molds were then left to grow together for five days under high humidity and room temperature conditions. These bricks underwent thermal pressing once they were fully grown to set their dimensions, and then a

convection drying cycle in a regular thermal oven. The authors created biotex jute, biotex flax, and biomid fiber reinforced sandwich structure composites 30 specimens using this process following ASTM D7250 and ASTM C393 standard dimensions $20.3 \times 6.4 \times 2.5$ cm³ ($8 \times 2.5 \times 1''$). These dried specimens were tested according to ASTM standards using the three-point bending method. Flax reinforcement demonstrated significantly higher strength compared to the other two skin materials, as the fungal mycelium used in the experiments showed a preference for flax. However, it was observed that stiffness was primarily determined by core strength, with weakly bound skin contributing little. The results of this research indicated that mycelium exhibits a preference for flax as the skin material, resulting in a stronger branching network and enhanced interfacial bonds. This preference may be attributed to the higher nutritional profile of flax, which includes starch, fatty acids, and ash, compared to jute and raw cellulose.

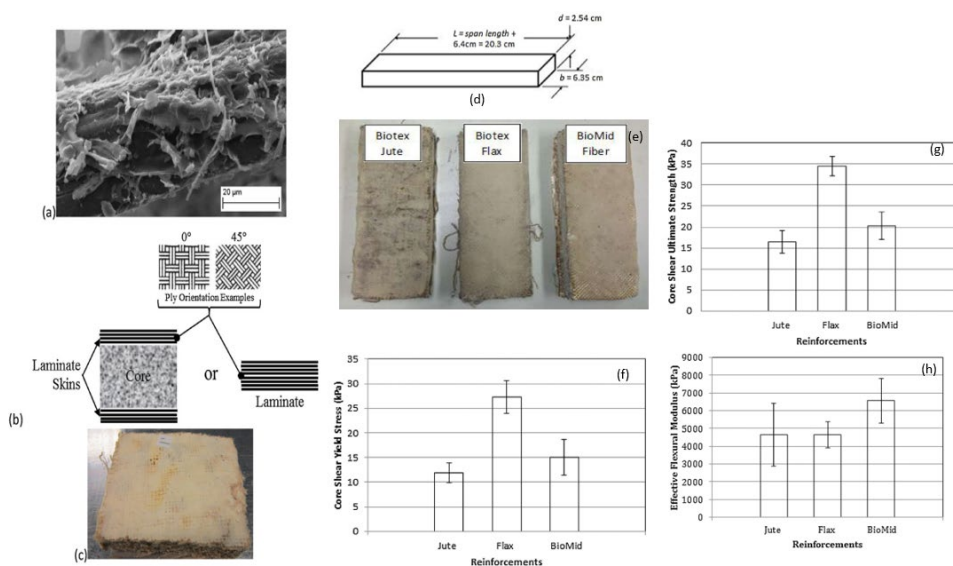


Fig. 28 (a) SEM image of jute/mycelium biocomposites, (b) laminated biocomposites orientation, (c) mycelium-based biocomposites sandwich structures, (d) biocomposites design following ASTM C393 standard, (e) jute, flax and BioMid reinforced beam specimens, (f) core shear yield stress comparison, (g) core shear ultimate strength comparison, and (h) flexural modulus comparison [107].

Sayed et al. [108] provided valuable insights into the mechanical properties and potential applications of PP-based composites reinforced with jute, kenaf, and pineapple leaf fiber (PALF). Fig. 28 shows the manufacturing steps required to create these composites. According to the findings, for all variations in fiber content (30%, 35%, 40%), the composites' tensile strength and impact strength significantly improved. In comparison to pure PP matrix, these had higher tensile (ranging from 43 to 58 MPa), flexural (53 to 67 MPa), and impact (25 to 46 kJ/m²) strengths. The high tensile strength of PALF gave PALF-PP composites the best mechanical characteristics. Fig. 29 shows the specimens and comparison of the tensile and flexural strengths of the PP-based composites. The comparison of different natural fibers enables researchers to select the most suitable fiber for fiber-reinforced composites based on specific product requirements.

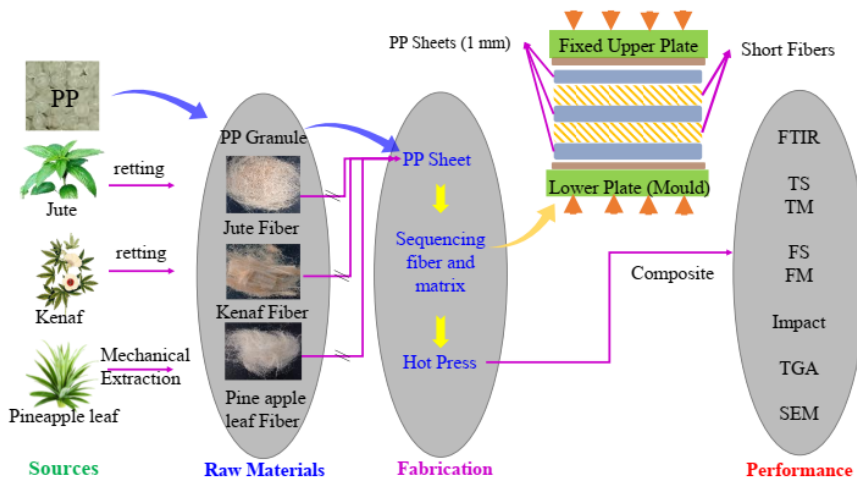


Fig. 29 Manufacturing steps to create PP-based composites reinforced with jute, kenaf, and PALF [108].

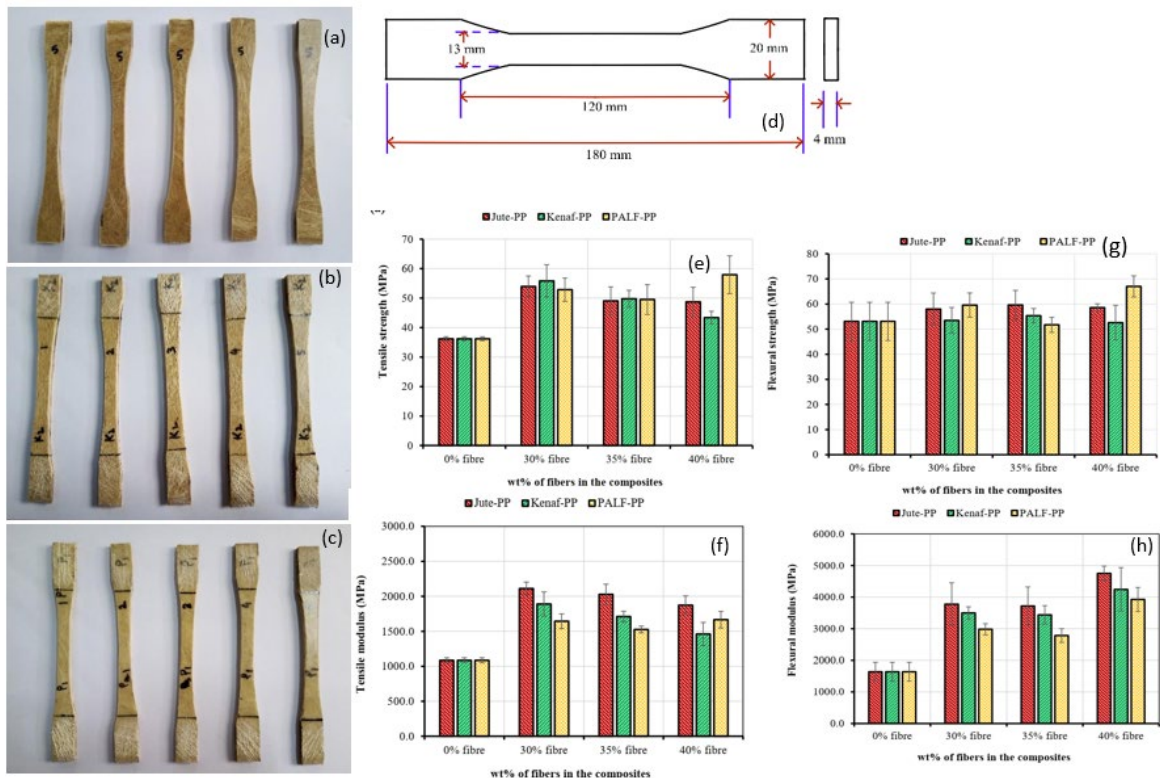


Fig. 30 (a) Jute specimens, (b) kenaf specimens, (c) PALF specimens, (d) specimen dimension (ASTM D638), (e) tensile Strength, (f) tensile Modulus, (g) flexural Strength, and (h) flexural Modulus of all specimens [108].

The authors took the fractured specimens to an SEM machine, and they observed at high magnification that there were voids between fiber-matrix bonding. Fig. 30 shows the SEM images of all the fracture specimens. The voids were less in the PALF-PP composites, indicating better adhesion between the fibers and the matrix. This improved fiber-matrix adhesion is likely to contribute to the ability of the PALF-PP composites to withstand higher loads compared to Jute and Kenaf PP composites. Fig. 31 SEM pictures of fractured jute, kenaf, and PLAF composites.

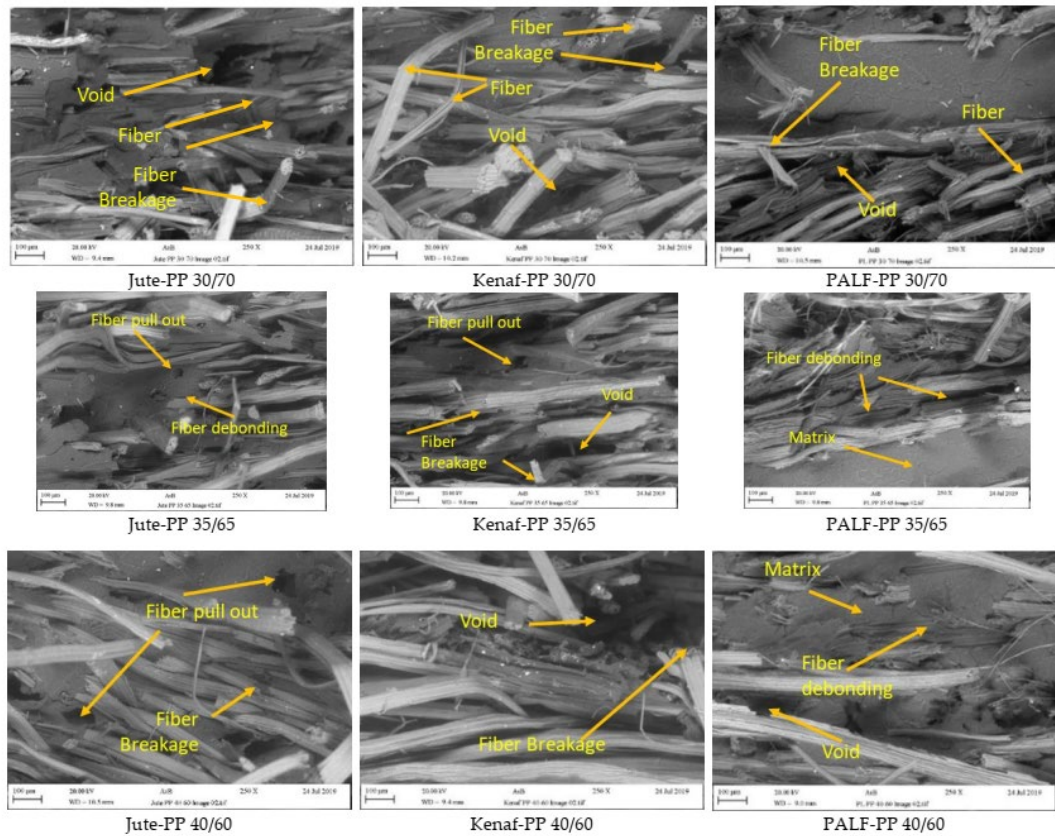


Fig. 31 SEM images of jute, kenaf, and PLAF fibers [108].

This research shows that biocomposites, which are made of natural fibers and biodegradable polymers, have better mechanical qualities in terms of tensile strength, flexural strength, and impact resistance, compared to individual fibers or polymers. The reinforcement provided by the natural fibers improves the biocomposites' overall performance, and the biodegradable polymer matrix guarantees their environmental friendliness. For this reason, the main objective of this research is to investigate LOM printed natural fiber reinforced biocomposites.

CHAPTER 3

METHODOLOGY

3.1 The LOM Prototype Design and Development

For this research, a LOM prototype was designed and developed to print PLA infused woven jute fiber reinforced biocomposites. This section is divided into 6 subsections: 1. customer needs; 2. brainstorming and selection of solutions; 3. design specifications; 4. CAD models of parts and the final product; 5. prototype building and assembly; 6. debugging and testing.

3.1.1 Customer Needs

There is a growing consumer demand for sustainable and eco-friendly products. Many industries and sectors, including automotive, construction, and packaging, are facing increasing regulations and standards for sustainability and reduced environmental impact. Natural fiber reinforced biocomposites align with these preferences and can be marketed as environmentally conscious alternatives. Natural fibers are lightweight, possess good mechanical properties, and can provide adequate strength and stiffness for various structural components. 3D printing of natural fiber reinforced biocomposites is an emerging field that combines the benefits of 3D printing technology with the sustainable and biodegradable properties of natural fibers. Natural fibers, such as jute, hemp, flax, and bamboo, can be used as reinforcing agents in the biocomposites filament or resin used for 3D printing. 3D printing also allows for complex and intricate designs that are difficult or impossible to achieve with traditional manufacturing methods. Natural fiber reinforced biocomposites can be 3D printed into custom shapes, structures, and geometries, providing design flexibility and customization options. 3D printing of natural fiber reinforced

biocomposites is still in its early stages, ongoing research and development are exploring new material formulations, processing techniques, and printer settings to optimize the properties and performance of the printed parts. For this reason, this research focused on building a LOM 3D printer prototype to explore the processing of natural fiber reinforced biocomposites using LOM. Fig. 32 shows the application of natural fiber reinforced biocomposites in the current world.

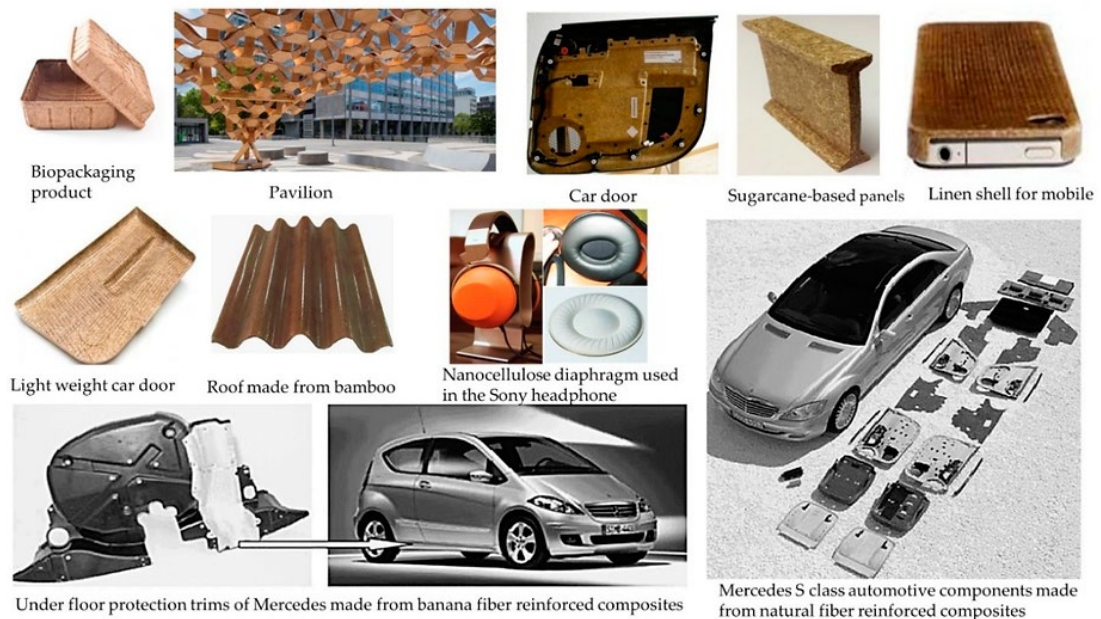


Fig. 32 Application of natural fiber reinforced biocomposites [109].

3.1.2 Brainstorming and Selection of Solutions

For the LOM prototype design, brainstorming is needed to select the solutions. The first step of the prototype build is to define the problem and requirements by brainstorming. The author searched for existing LOM machines to get an overall idea of how to build the prototype. LOM technology was invented by Helisys, now known as Cubic Technologies. They created the first LOM machines for sale and have improved the procedure ever since

[110]. A variety of LOM machines are available from Cubic Technologies, and they are renowned for their high build volumes and precision. The distinctive LOM process used by Mcor Technologies, which uses common office paper as the build material, to create highly detailed, full-color models. CleanGreen3D Limited later purchased Mcor Technologies [111]. Fig. 33 shows the CleanGreen3D Limited CG-1 LOM 3D printer.



Fig. 33 CleanGreen3D limited CG-1 LOM 3D printer.

The LOM prototype followed the CleanGreen3D CG-1 3D printer's working principle. The working principle involves two identical rollers (i.e., material feed roller and material waste take-up roller) that can be rotated using two stepper motors. Once the material feeding roller rotates it will supply the material in the build plate of the LOM prototype. Simultaneously, a laser head will cut the fiber according to the required design and then the waste take-up roller will take the unnecessary materials out of the build plate. G-codes are used to send the required CAD design in the LOM prototype. The brainstorming sessions led to the selection of the necessary components and solutions for the LOM prototype. These are described below:

3.1.2.1 Laser Head Selection

Usually for the LOM, the laser head needs to have a specific power so that it can easily cut the woven fibers. The research team started investigating with lower-watt laser heads (i.e., 5.5W, 7.5W, and 10W) to see if they could penetrate the fiber. However, these low-powered lasers are good for engraving but not for penetrating. Then, the research team decided to purchase a high 40W laser head that could easily penetrate the woven fiber used in this experiment. This 40W laser head enabled the LOM prototype to cut the woven fiber infused PLA biopolymer with its high power in a single pass. Fig. 34 (a) shows all the failed laser heads and 34 (b) shows the 40W laser head that is used for the prototype.

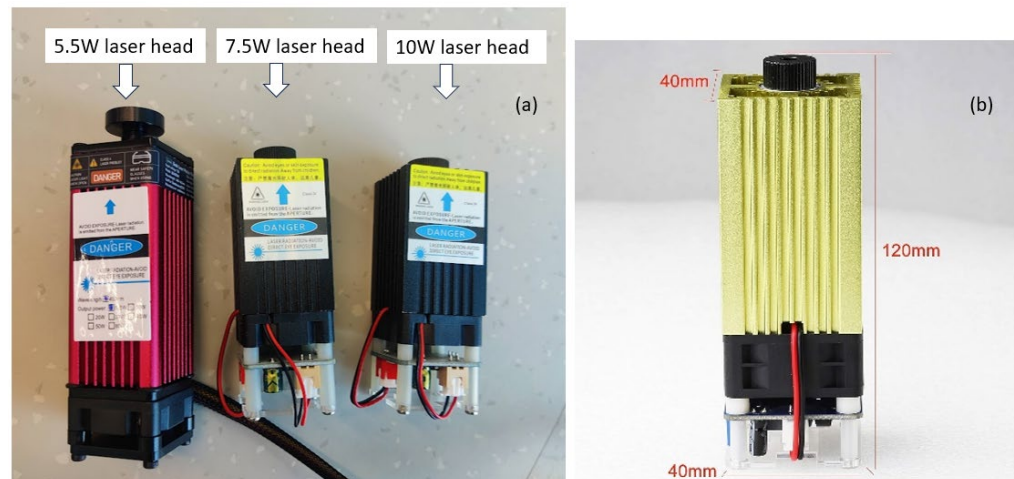


Fig. 34 (a) Failed 5.5W, 7.5W and 10W laser heads, and (b) selected 40W laser head.

3.1.2.2 Motherboard, Motors, and Motor Drivers Selection

After market research of the available 3D printer motherboards, the author selected MKS DLC32 motherboard. For controlling the prototype from the motherboard, a touch screen controlling panel named MKS TS35 RV2.0 was purchased. Additionally, five Tronxy SL42S TH40 Stepper Motors were purchased for driving the X, Y, and Z axes, material feed roller motor and material wastage take-up roller respectively. For driving

these motor drivers, A4988 motor drivers were used. Fig. 35 shows the MKS DLC32 motherboard with the MKS TS35 touchscreen and A4988 motor drivers.

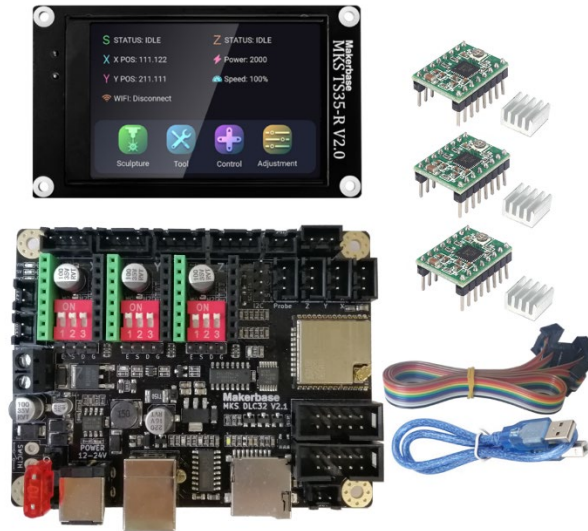


Fig. 35 MKS DLC32 motherboard with MKS TS35 RV2.0 touchscreen and A4988 motor drivers.

3.1.3 Design Specifications

The design specifications of the prototype are described below in Table IV.

Table IV
DESIGN SPECIFICATIONS FOR THE LOM PROTOTYPE

Design Parts	Specifications Description
Frame	552×485×510 mm
Build Plate	220×220×300 mm
Material Feed Roller	292×70×70mm
Material Wastage Take up Roller	292×70×70mm
Laser Head	40W, 120×40mm

Motherboard	MKS DLC32
Controlling Panel	MKS TS 35 R V2.0 Touchscreen
Motor Drivers	A4988 Stepper Motor Drivers
Stepper Motors	Tronxy SL42S TH40 Motors
Power Input/ Output	12V-24V

3.1.4 CAD Models of The Parts and The Final Product

SolidWorks software is used to do the CAD design of the LOM prototype. The following CAD designs are made before the prototype is built:

3.1.4.1 Main Frame CAD Model

The dimensions of the main frame of the prototype are 552×485×510 mm. Fig. 36 shows the SolidWorks design of the main frame.

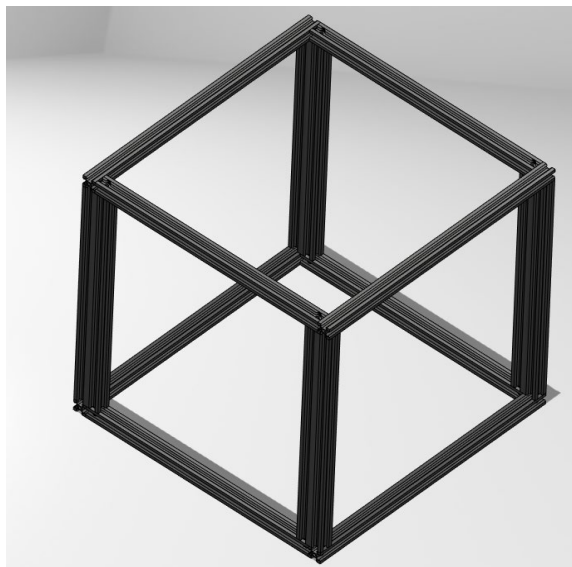


Fig. 36 Design of the main frame of the LOM prototype.

3.1.4.2 Build Plate CAD Model

The build plate dimension was 220×220×300 mm. Fig. 37 shows the build plate's SolidWorks design.

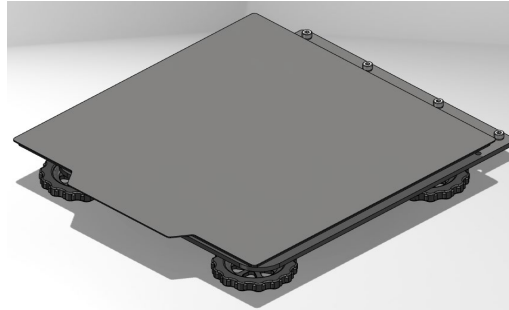


Fig. 37 Design of build plate of the LOM prototype.

3.1.4.3 Material Feed and Wastage Take-up Roller CAD Models

Material feed and wastage take-up rollers are identical with a dimension of 292×70×70 mm. These rollers are designed in such a way that two stepper motors can rotate the rollers. Stepper motors are connected to the roller using a timing belt and a pulley. Stepper motor covers are designed to hold the stepper motors with the frame. Fig. 38 shows the two rollers CAD design for the LOM prototype.

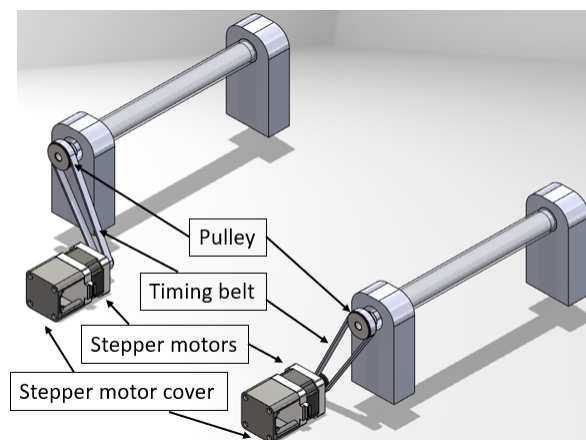


Fig. 38 Design of the material feed and wastage take-up roller with necessary components, i.e., pulley, timing belts, and stepper motor covers.

3.1.4.4 Laser Head CAD Model

The 40W laser head dimensions are 120×40 mm. Fig. 39 shows the SolidWorks design of the laser head.

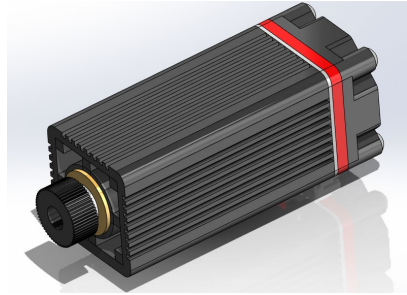


Fig. 39 CAD design of 40W laser head.

3.1.4.5 The Final LOM Prototype CAD Model

After the 3D CAD design of every part, the final prototype was assembled using SolidWorks software. Fig. 40 shows the final prototype designed and assembled using SolidWorks.

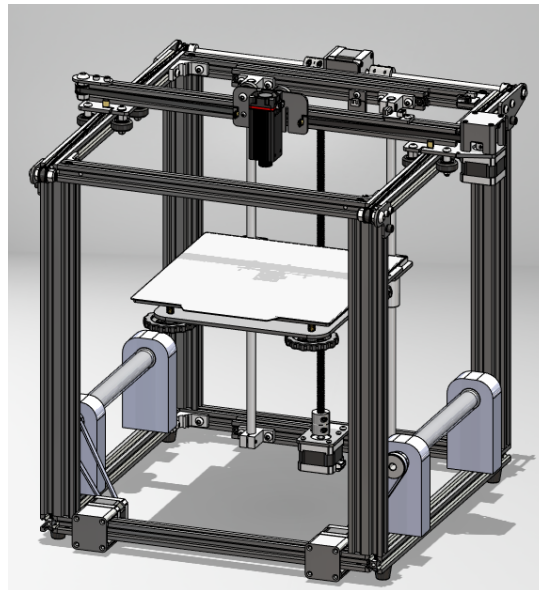


Fig. 40 3D CAD design of LOM prototype.

3.1.5 Prototype Building and Assembly

3.1.5.1 Frame, Build plate, and Laser Head Assembly

After the completion of the design phase, the author started constructing the LOM prototype. The initial step involved assembling the frame, followed by the installation of the build plate. To ensure precise movement, stepper motors for the X, Y, and Z axes, as well as the material feed roller and waste take-up roller, were installed. Additionally, the incorporation of several belts facilitated smooth travel between the X, Y, and Z axes. Custom 3D-printed covers for the stepper motors were created using the Stratasys Uprint SE Plus 3D printer. Five Tronxy SL42S TH40 stepper motors are used to control the X, Y, and Z axes of the printing platform, both the material feeding and the take-up rollers, respectively. All the stepper motors, equipped with their FDM printed covers, were securely attached to the body frame. As a crucial component of the LOM prototype, the 40W laser head was carefully installed with the addition of a small block on the frame, ensuring precise and controlled laser operation. The material feed-up roller feeds the prepregs continuously. After the laser cuts the prepreg, the material take-up roller takes the unused materials away, leaving the laser-cut part in the building platform. This process allows the next layer of printing material to be placed just above the previous one, and the same process keeps repeating until all the layers of the model to be built are completed. The entire model is then moved to a thermal press for a final press so the biopolymers can be melted again to have all layers bonded together. Fig. 41 shows the assembled LOM prototype.

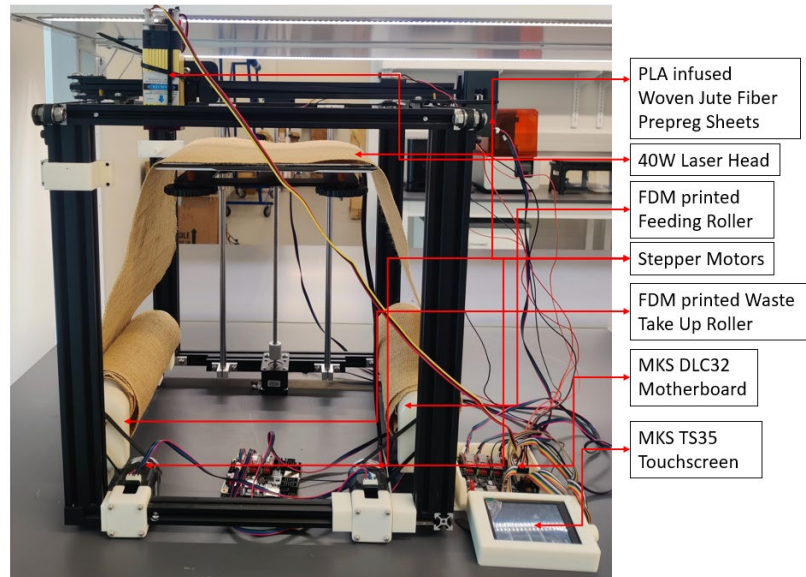


Fig. 41 The assembled LOM prototype.

3.1.5.2 Motherboard Connection Setup

The research team proceeded to establish the connection between the LOM prototype and the MKS DLC32 motherboard. Fig. 42 shows a typical interface of MKS DLC32 whose input voltage range is 12-24V and maximum current is 5A. The USB-PC interface is used for programming and online control and in the TF card slot a SD card can be installed for offline engraving file storage in the form of G-code. As depicted in Fig. 42, the X, Y, and Z axis stepper motor wires were carefully connected to their respective ports on the MKS DLC32 interface. To drive the motors effectively, three A4988 motor drivers were expertly positioned in the X, Y, and Z motor drive slots. Additionally, another set of wire connections from the stepper motors was made to the X, Y, and Z end stops on the motherboard. These end stops serve as essential limit switches, with an input signal voltage of 5V, ensuring precise movement and control. Moreover, the motor drivers were

configured to accommodate the required micro-step settings for the LOM prototype, as shown in Fig. 43, enabling optimal performance and precision during operation.

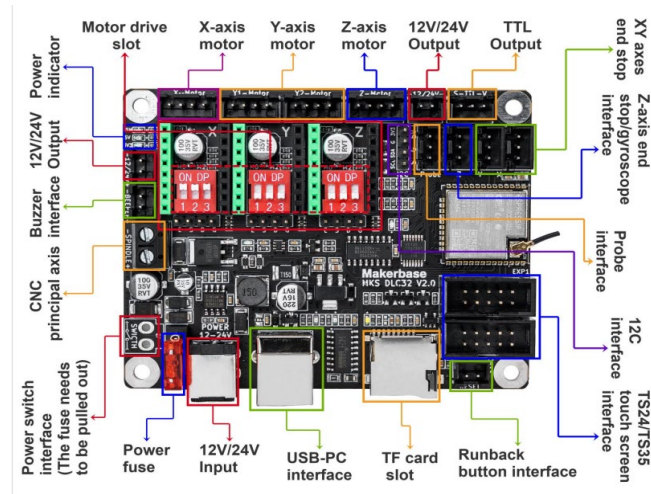


Fig. 42 MKS DLC32 interface introduction.

The 40W laser head utilized in the LOM prototype is of the TTL-PWM type, characterized by its 3PIN configuration. Consequently, the laser head's wire was appropriately connected to the TTL output port. The wiring diagram, depicted in Fig. 43 (c), illustrates the connections: V corresponds to the power input, with the voltage aligning with the power input voltage (e.g. if the power input is 24V, the output here will also be 24V), G represents the ground, and TTL input serves as the PWM signal input. The default main frequency is set at 1K Hz, although it can be adjusted within the range of 1K Hz to 10K Hz. The voltage output during PWM signal modulation ranges from 0V to 5V. For the MKS TS35 touchscreen, the wiring procedure is illustrated in Fig. 43(d). The EXP1 and EXP2 interfaces on the touchscreen correspond to the respective motherboard interfaces, facilitating seamless communication and control between the touchscreen and the LOM prototype.

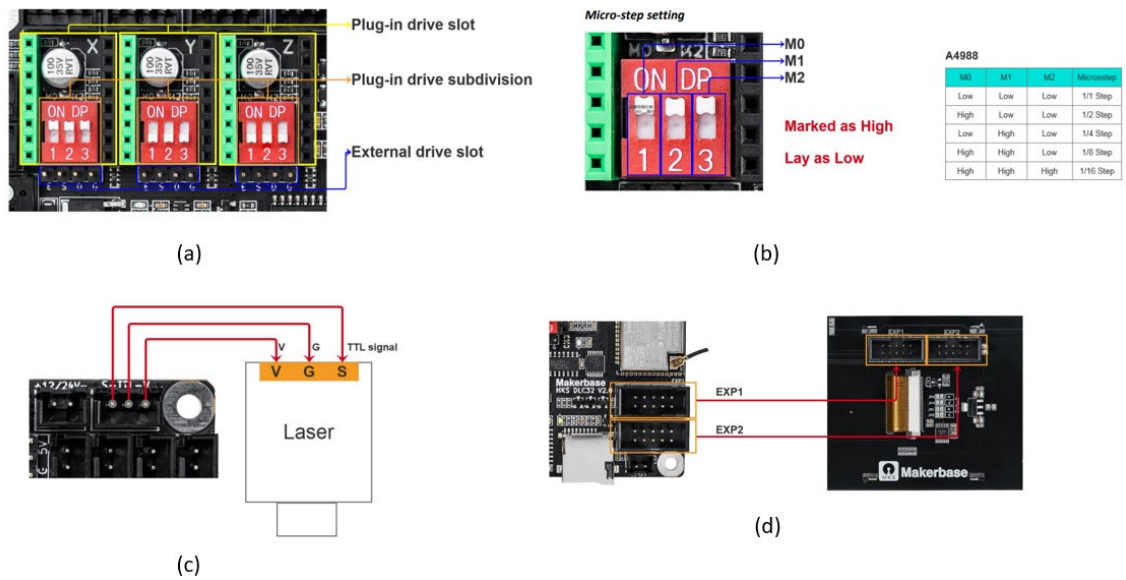


Fig. 43 (a) Motor drive Settings, (b) micro-step setting for A4988 drivers, (c) laser module connection, and (d) touch screen interface (EXP1 and EXP2).

Upon completing the wiring installation, the MKS DLC32 motherboard was programmed using the pre-installed firmware that came with the motherboard. Additionally, the software "LaserGRBL" was employed to configure the MKS DLC32 to meet specific requirements. Fig. 44 shows the successful integration and operation of the motherboard and touchscreen with the prototype.

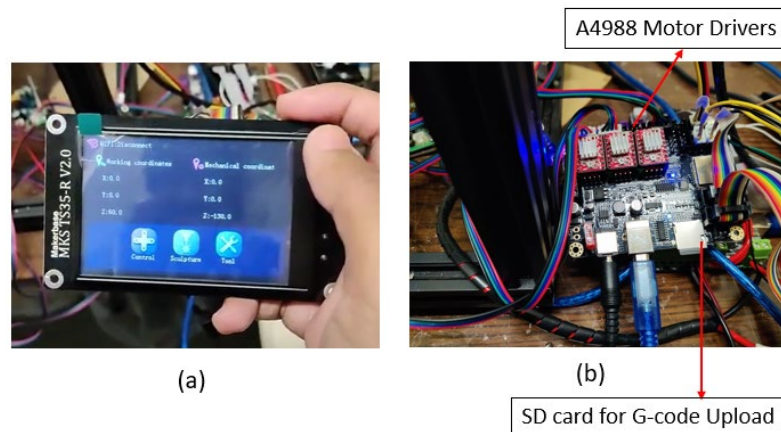


Fig. 44 (a) MKS TS35 touchscreen panel interface, and (b) MKS DLC32 with necessary wire connections and motor drives.

3.1.6 Debugging and Testing

3.1.6.1 CAD Designs for Testing

Three 3D CAD designs, spur gear, key tag, and wrench were made using SolidWorks for the debugging and testing of the LOM prototype print. Fig. 45 shows the CAD design of the spur gear, key tag, and wrench. These CAD designs are then uploaded to the Fusion360 Slicer software to slice each of the layers. Fig. 46 shows the slicing layers of these parts.

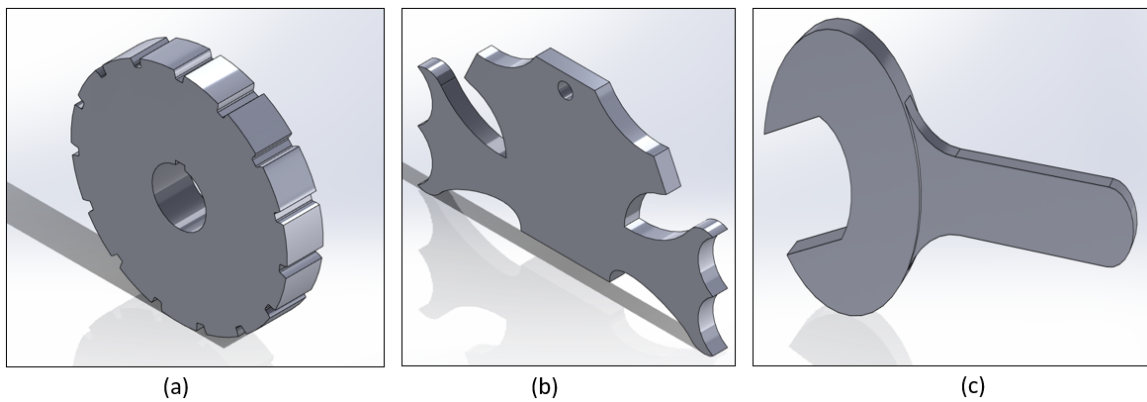


Fig. 45 (a) Spur gear CAD Design, (b) key tag CAD design, (c) wrench CAD design.

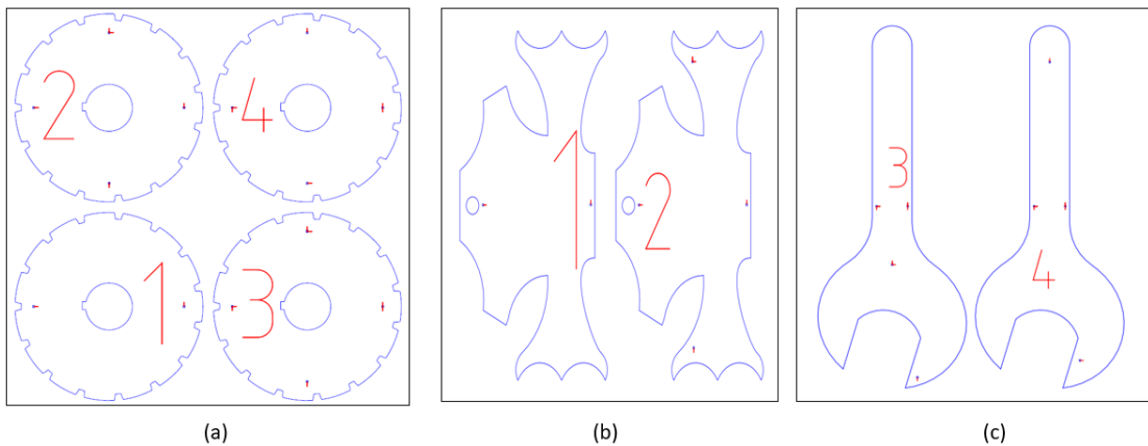


Fig. 46 (a) Spur gear sliced layers, (b) key tag sliced layers, (c) wrench sliced layers.

3.1.6.2 G-code Implementation

Upon slicing the CAD model into printable layers using the Fusion360 slicer software, the subsequent step in the process involved the utilization of the Inkscape laser tool software plugin. This tool was instrumental in generating the necessary G-code, a crucial set of instructions that dictate the precise movements of the 3D printing equipment. This process of G-code generation serves as a bridge between the digital design and the physical manifestation of the object. Providing a tangible connection between the virtual and physical realms, the G-code serves as a blueprint for the additive manufacturing process to follow. To facilitate this visualization, an NC viewer, a web-based platform with the specific purpose of rendering G-code output, was employed. This allowed the author to gain a clear visual insight into how the G-code commands were set using the plugin. The author then modified the G-code commands according to the specific requirements of the prototype and part building. The NC viewer functioned as a tool for validation, enabling the identification and correction of any discrepancies or errors in the G-code, ensuring a seamless and accurate translation from design to production. Fig. 47 shows the outcome of this G-code implementation and its execution, offering a comprehensive representation of how these instructions materialize into the desired output.

The G-code configuration was a critical aspect of this process, with laser power set to 100% (denoted by S255), signifying the maximum laser intensity for the task. Additionally, the feed rate for each movement across the X, Y, and Z axes was set to 70 units (indicated by F-70.0 in Fig. 47). This deliberate choice of a relatively slower feed rate played a pivotal role in the successful execution of the cutting process for the PLA-infused jute fiber-reinforced composite sheets. The rationale behind this decision was to ensure

that the laser had sufficient time to effectively cut through the composite material. A faster feed rate could potentially lead to inadequate cutting as the laser's rapid motion might not allow for the necessary precision in the cutting process.

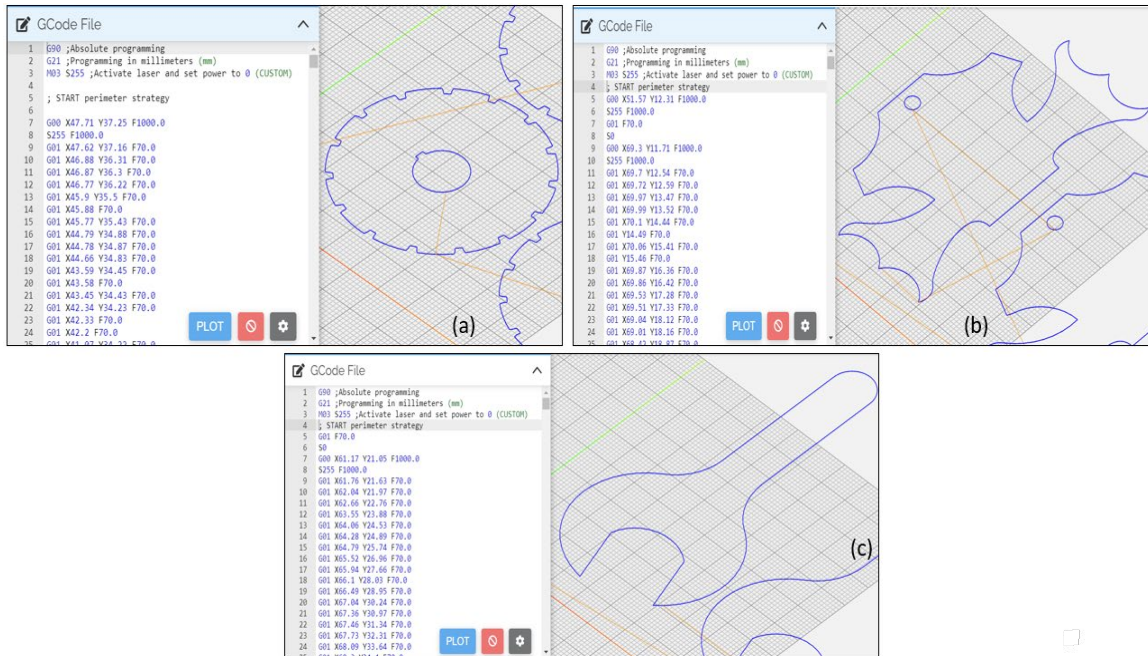


Fig. 47 (a) Spur gear G-code implementation in NC-viewer, (b) key tag G-code implementation in NC-viewer, and (c) wrench G-code implementation in NC-viewer.

3.1.6.3 LOM Printed Parts for Testing

Once the process of generating the G-codes, which serve as essential instructions for the 3D printing procedure, has been completed, the subsequent step involves the transfer of these G-codes to the MKS DLC32 motherboard. This integration is achieved through the utilization of the SD card slot on the motherboard, providing a seamless means of initiating the printing process. To set the printing process into motion, specific commands were conveyed to the motherboard through the device's touchscreen interface. This user-friendly approach allows for a straightforward and intuitive initiation of the

printing sequence. Fig. 48 (a) shows the G-code in MKS TS-35 touchscreen which is uploaded to the MKS DLC 32 motherboard.

To visually validate the efficacy of this approach, Fig. 48 (b) serves as a representation of the concrete results achieved through the LOM printing technique. The image captures the tangible output of the LOM printing process, showcasing the successful creation of a spur gear, a key tag, and a wrench. Each of these objects, produced using the LOM prototype, stands as a testament to the effectiveness of the 3D printing methodology in generating intricate and functional items.

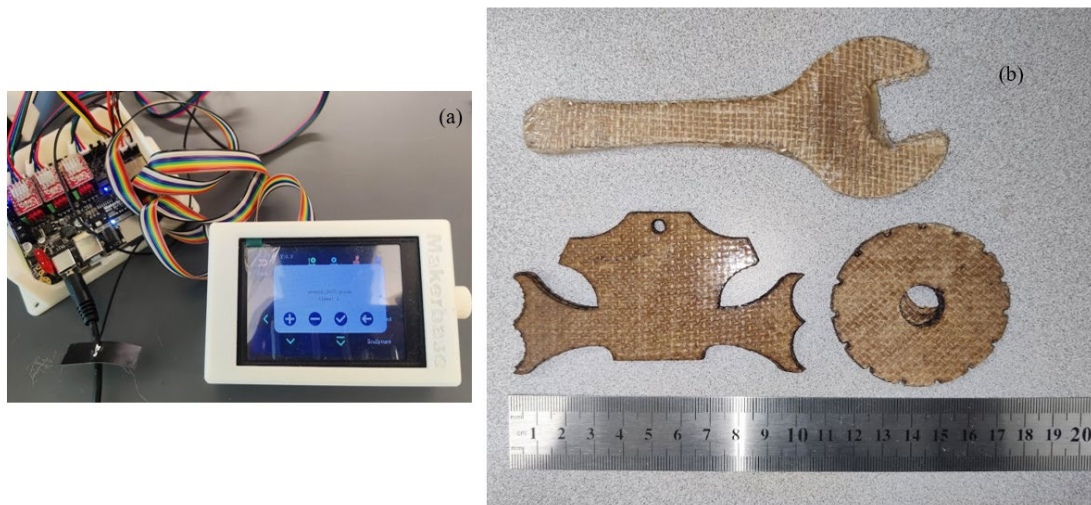


Figure 48 (a) Wrench G-code uploaded shown in MKS TS35 touchscreen, and (b) LOM 3D printed PLA infused Jute fiber reinforced wrench, key tag, and spur gear.

3.2 Preparation of Materials and Mechanical Test Samples

To reinforce the composite material, woven jute fabrics were employed as the fiber reinforcement. The jute fabric exhibited a fiber density of 5 threads/cm, while its average area density measured 338 g/m^2 . This chosen jute fabric possessed a singular ply with an average thickness of approximately 0.071 millimeters. The deliberate selection of such

woven jute fabrics as the reinforcing medium underscores the intention to enhance the mechanical properties of the resulting composite material, capitalizing on the inherent attributes of jute fibers in the pursuit of achieving desired performance characteristics. The visual representation of the woven jute fiber used in this study is depicted in Fig. 49 (a).



Fig. 49(a) Woven jute fiber used in this research, (b) weighted single layer jute fiber, and (c) weighted PLA coated jute fiber.

To initiate the fabrication process, the mixing of jute fiber and PLA polymer was accomplished through a multistep procedure. In the initial phase, the jute fiber underwent a coating procedure utilizing powdered PLA polymer. Prior to this, continuous rolls of jute fiber were meticulously pre-cut into uniformly sized sheets, each measuring 220×254 mm. Employing a manual layup technique, these sheets were uniformly coated with PLA powders. The PLA powder weight percentage of the jute/PLA biocomposites can be found by dividing the PLA powder weight by the total weight of the jute fiber and PLA powder mixture, where the PLA powder weight can be calculated from the difference of the mixture and the clean jute fiber used to make the mixture. The weight-taking procedure is shown in Fig. 49 (b) and 49(c). The calculated data are given below:

Jute fiber (single layer) = 8.97g

Jute fiber mixed with PLA powder (single layer) = 17.62g

PLA powder weight = $17.62 - 8.97 = 8.65\text{g}$

PLA powder weight percentage = $(8.65/17.62) \times 100 = 49.09\%$

Then, Dupont Kapton HN Films was used to enclose the coated jute fiber sheets. The subsequent stage involved subjecting the encapsulated sheets to a controlled heating process using a Carver 4120 thermal press. By setting an operating temperature of 180°C and applying a pressure of 5 bar, these sheets were for a duration of 10-15 minutes. Through this thermal consolidation process, the coated jute fiber sheets underwent a transformation, resulting in the creation of PLA-infused jute fiber reinforced prepreg sheets. Using the LOM prototype, the prepreg sheets underwent a transformative 3D printing process to create jute fiber-reinforced biocomposites. This process facilitated the transformation of raw materials into complex biocomposite structures with enhanced mechanical attributes. The manufacturing process of the prepreg sheets is depicted in Fig. 50.

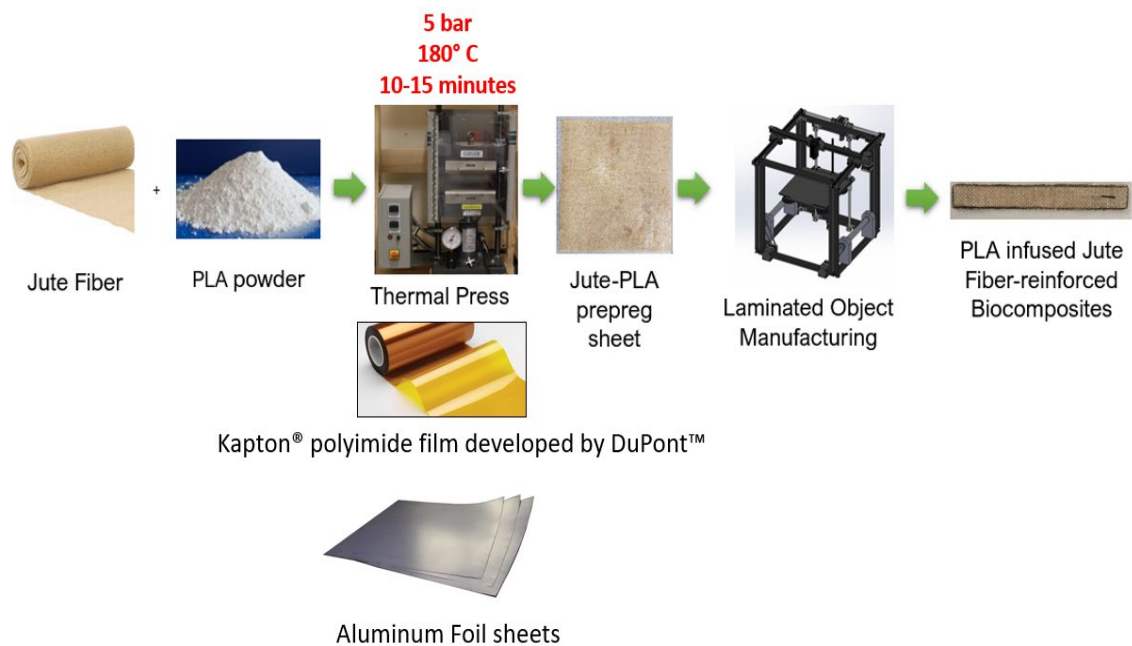


Fig. 50 Manufacturing steps for LOM printed PLA infused woven jute fiber reinforced biocomposites.

3.3 Mechanical Test Methodology

3.3.1 Tensile Test

The evaluation of tensile properties was meticulously undertaken through a series of tests carried out on flat specimens, employing the INSTRON 5582 Universal Testing Machine (UTM) as portrayed in Fig. 51. The experimental setup aimed to ensure accuracy and reliability in the subsequent data collection process. In order to account for the distinctive characteristics of different materials, the testing speeds were thoughtfully calibrated. The testing speeds for the jute/PLA composites, pure PLA, and woven jute samples were set at 2.0 mm/min, 5.0 mm/min, and 300 mm/min, respectively. The UTM system automatically collected tensile stress-strain data. The fundamental parameters assessed during the tensile testing were the ultimate tensile strengths and elastic moduli. The ultimate tensile strengths were determined from the maximum tensile stresses reached during testing, and the elastic moduli were calculated by averaging the slopes of the tensile stress-strain curves from five tested samples. This research adhered to ASTM standards for testing: ASTM D3039/D3039M - 14 for PLA-infused samples, ASTM D5035-06 for woven natural jute fibers, and ASTM D638-14 for pure PLA filament 3D printed specimens.



Fig. 51 INSTRON 5582 universal testing machine.

The stl. files for the PLA infused jute fiber reinforced biocomposites tensile tests (following ASTM D3039/D3039M-14 standards) were generated using SolidWorks. These files were subsequently transformed into cutting contours for each individual layer through the Fusion 360 slicer software and subsequently uploaded to the prototype. The dimensions of the jute/PLA tensile and flexural test samples are $250 \times 25 \times 2.5$ mm. The cross-sectional profiles of the test samples were generated using the LOM prototype and layered to achieve the desired thicknesses, as illustrated in Fig. 52(a) and (b) show the CAD design, and Fig. 52(c) shows the G-code generated for the print. A total of five 6-ply PLA-infused tensile specimens were fabricated using the LOM prototype. To enhance the quality, all samples produced using the LOM technique underwent thermal pressing. The final samples generated using the LOM approach are depicted in Fig. 53.

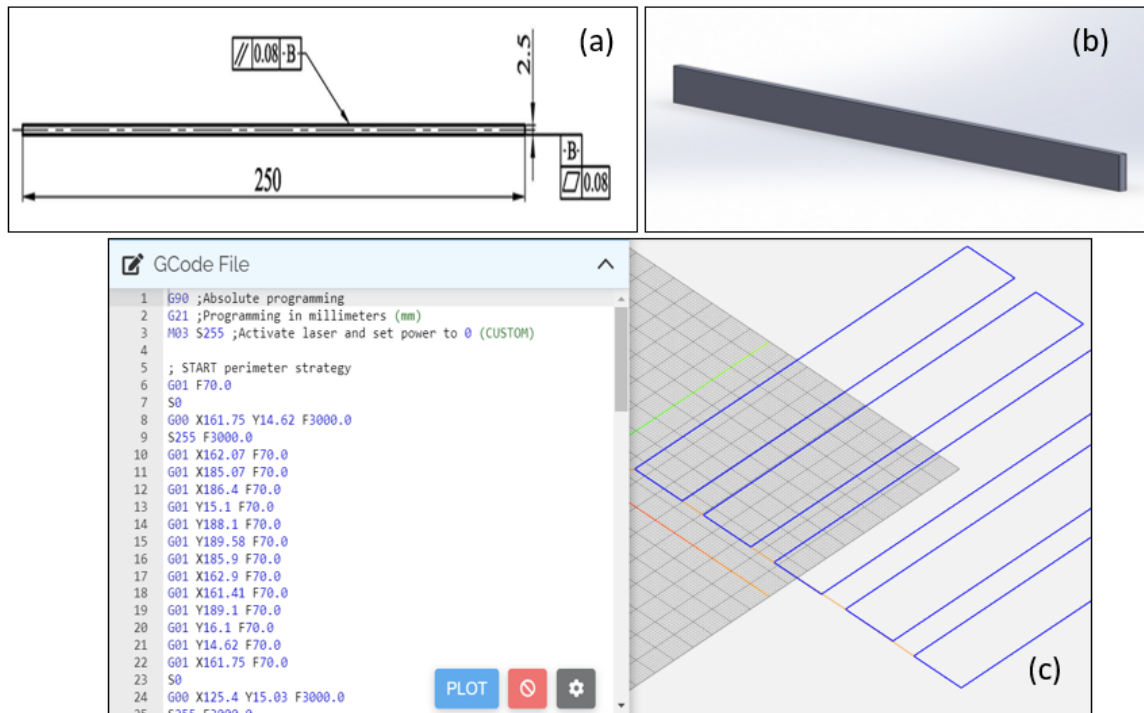


Fig. 52(a) ASTM D3039/D3039M-14 tensile specimens' dimension, (b) SolidWorks design for preparing the G-code, and (c) G-code for LOM print.



Fig. 53 LOM printed PLA infused woven jute fiber reinforced biocomposites [110].

For the pure PLA filament FDM printed specimens, the initial steps involved designing 3D CAD models of untainted PLA samples through SolidWorks, adhering to the dimensions stipulated by ASTM D638 – 14 standards. These models were 3D printed utilizing pure PLA filaments by means of a Raise3D Pro2 Plus 3D printer shown in Fig.

55(a). The dimensions of the pure PLA tensile test specimens were set at $165 \times 13 \times 3.2$ mm, as depicted in Fig. 54. Likewise, five test samples were fabricated in a solid form without any internal hollowness (0% hollow). Raise3D Pro2 Plus 3D printed PLA filament specimens are shown in Fig. 55(b).

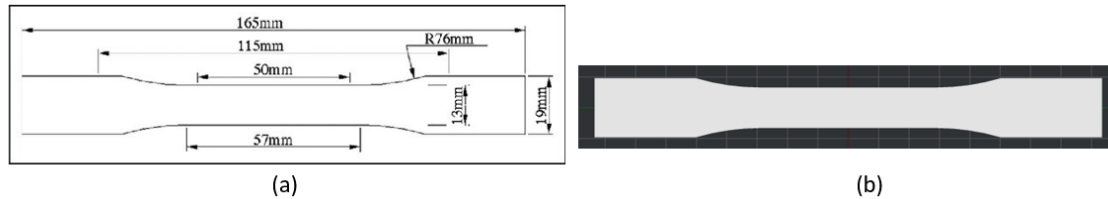


Fig. 54 (a) ASTM D638-14 tensile Specimen Dimension, and (b) SolidWorks design for preparing the G-code.

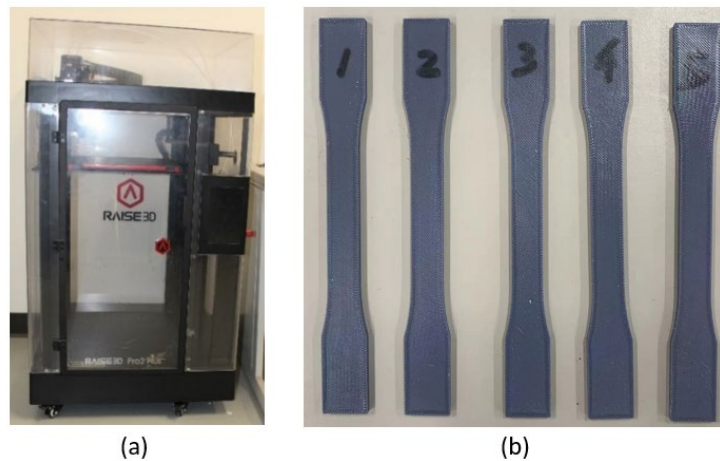


Fig. 55 (a) Raise 3D pro2 Plus FDM 3D printer, and (b) Pure PLA filament FDM 3D printed tensile specimens [110].

Finally, individual layers of jute fabric were shaped into rectangular pieces measuring 150×24 mm, adhering to the dimensions outlined by the ASTM D5035 – 06 standard. The average thickness of the fiber was 0.86 mm, as illustrated in Fig. 56. Same as before, five single-ply rectangular jute fiber sheets were created.



Fig. 56 Woven jute fibers cut for tensile tests following ASTM D5035 – 06 [110].

3.3.2 Flexural Tests

In the pursuit of comprehensively characterizing the mechanical properties of the jute/PLA composite specimens, 3-point bending tests were carried out to determine both the ultimate flexural strengths and the flexural moduli. These parameters play a pivotal role in understanding the material's response to bending forces and its ability to withstand such stresses. To ascertain the ultimate flexural strengths, the points corresponding to the locations of maximum tensile stresses were identified during the testing procedures. This comprehensive approach ensured a reliable assessment of the material's ability to withstand bending loads and its overall stiffness.

The flexural tests were conducted at a uniform speed of 1.0 mm/min for both the jute/PLA composites and pure PLA samples. The respective flexural stress-strain data were automatically captured through the utilization of the same Universal Testing Machine (UTM) system. The experimental setup involved the fabrication of five specimens each for the jute/PLA composites, utilizing the LOM prototype, and for the pure PLA, employing the Raise3D Pro2 Plus 3D printer. The ultimate flexural strengths were documented at the

points of maximum tensile stresses reached during the tests, while the flexural moduli were subsequently derived by computing the average slope of the flexural stress-strain curves derived from the analysis of the five tested samples. For the PLA-infused jute fiber-reinforced samples, the test procedure outlined in the ASTM D7264/D7264M-07 standard was adopted. The specimen's dimensions were $60 \times 13 \times 4$ mm, as visualized in Fig. 57(a). Fig. 57(b) shows the CAD design and Fig. 57(c) shows the G-code generated for LOM printing. Using the LOM prototype, a set of five 12-ply flexure specimens was manufactured. Fig. 58 shows the printed 5 flexural specimens. The flexural tests were executed by a three-point bending setup in the Instron UTM.

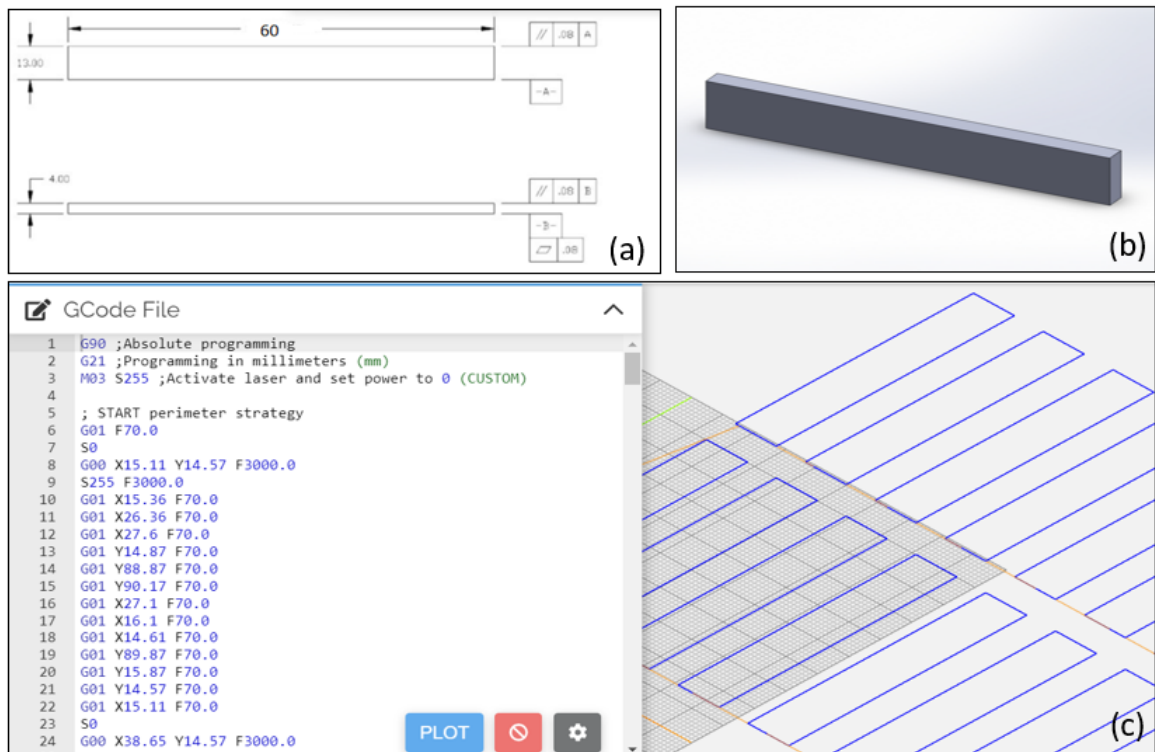


Fig. 57 (a) ASTM D7264/D7264M-07 flexural test dimensions, (b) SolidWorks design, and (c) G-code for LOM print.



Fig. 58 LOM prototype printed flexural test specimens [110].

The flexural tests for pure PLA samples adhered to the ASTM D790 - 10 standard procedure and were conducted through three-point bending tests in the Instron UTM. These samples, with dimensions measuring $127 \times 12.7 \times 3.2$ mm, were produced using the RAISE 3D Pro2 Plus printer. The dimension of the specimen is shown in Fig. 59(a) and the CAD design of the specimen is shown in Fig. 59(b). Raise 3D printing of five flexural specimens of the specified dimensions is shown in Fig. 59(c).

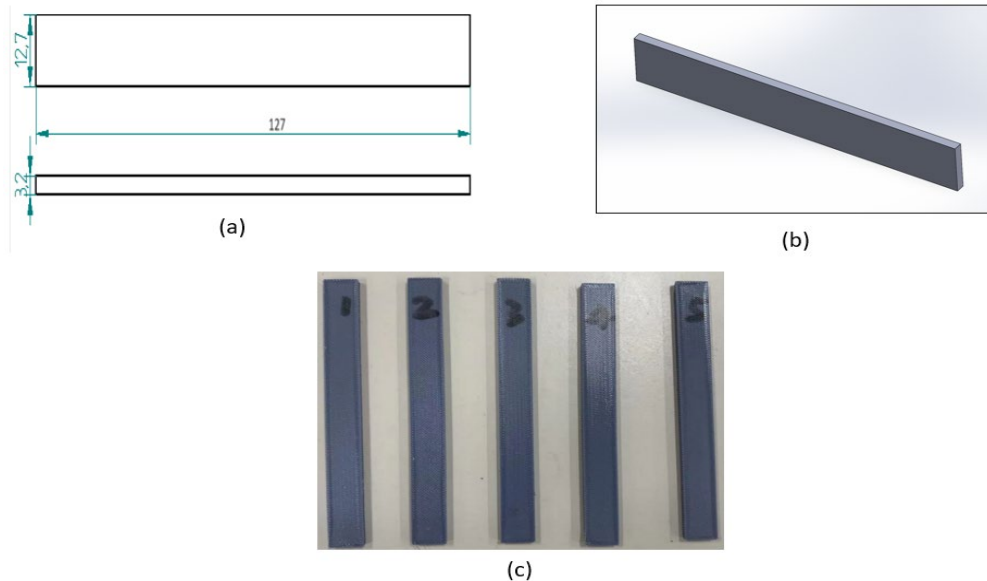


Fig. 59 (a) ASTM D790-10 standard flexural specimen dimension, (b) CAD design of the flexural specimen, and (c) Raise 3D FDM printed flexural specimens [110].

3.3.3 SEM Imaging Tests

To delve into the microscopic details of the jute/PLA composite materials that had undergone tensile and flexural tests, an analytical scanning electron microscope (SEM) was harnessed for its imaging capabilities. Specifically, the JEOL JSM-6010LA Analytical SEM was employed for this purpose, offering a platform to examine the internal structure and characteristics of the failed composite specimens. The utility of SEM imaging is rooted in its capacity to visualize minute features at high resolutions, enabling the author to gain insights into the underlying phenomena that govern material behavior. In this investigative phase, two distinct failed LOM printed jute/PLA composite samples were sectioned through the application of a precise utility knife. This strategic slicing procedure allowed for the unveiling of cross-sectional views of the specimens, providing a glimpse into their internal composition and arrangement. Within a controlled vacuum environment characterized by a pressure of 30 pascals, SEM imaging was executed at an acceleration voltage of 7 kilovolts. This choice of parameters ensured optimal imaging conditions that facilitated the capturing of detailed structural information. This approach proved invaluable in revealing both the broader structural layout and the finer features present within the jute/PLA composite samples. SEM imaging facilitated the identification of any anomalies, irregularities, or failure modes that could have contributed to the observed mechanical behavior. Fig. 60 shows the SEM machine used in this research to test the failed specimens.

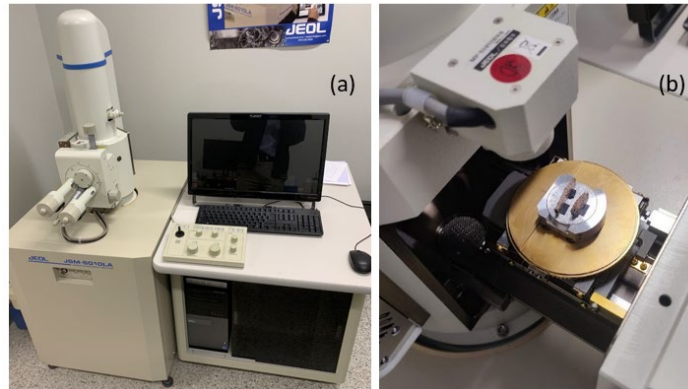


Fig. 60 (a) JEOL JSM-6010LA SEM machine, and (b) failed mechanical test samples loaded into the SEM.

3.4 FEA Simulation of LOM Printed Jute/PLA Biocomposites

The simulation of LOM printed jute/PLA biocomposites involves utilizing computational techniques using ANSYS software to model and assess the mechanical characteristics of biocomposite materials. These simulations helped the research team to test biocomposites under diverse conditions and loads even before physical production takes place. Through inputting material properties, geometric details, and boundary conditions, these simulations offer valuable insights into how LOM printed jute/PLA biocomposites will perform in various applications. The author can optimize the composition and design of biocomposites by integrating experimental data with simulation outcomes. The objective of ANSYS analysis and simulation of LOM-printed jute/PLA biocomposites is to predict the mechanical properties and mechanical response of jute/PLA biocomposites such as tensile and flexural tests. The simulation results will be compared and verified with experimental results.

For both the tensile and flexural Finite Element Analysis (FEA) simulation, the engineering data needs to be given to put the mechanical properties of jute/PLA

biocomposites. The simulation is based on the engineering data. The shear modulus (G) of the LOM-printed biocomposites can be determined through the multiplication of Young's modulus (E) by a factor of 0.4 [111]. Likewise, the shear strength is ascertainable by multiplying the tensile strength (TS) by a factor of 0.7 [111]. Equations 1 and 2 show the formula required to calculate shear modulus and shear strength.

$$G \approx 0.4 E \quad (1) [111]$$

$$S \approx 0.7 TS \quad (2) [111]$$

In order to calculate the density, five individual samples of both tensile and flexural specimen mass were measured. Then, the average mass (m) of these 5 specimens was computed. Subsequently, the density (ρ) is obtainable through division, where the average mass (m) is divided by the volume (V) of the biocomposite specimen. Equation 3 shows the formula to calculate density.

$$\rho = \frac{m}{V} \quad (3)$$

To determine the compressive strength of jute/PLA biocomposite material, the author utilized the compressive strength of the raw PLA material. This choice is made because, during the compression of the biocomposite material, the jute fibers were bearing a minimal load as they were wrapped inside the biocomposite structure. For the same reason, the author used the Poisson's ratio of 0.35 from the original PLA in the simulations. Table V shows the engineering data required for this FEA simulation.

TABLE V
WOVEN JUTE FIBER REINFORCED PLA BIOCOSCOMPOSITES' MECHANICAL
PROPERTIES DATA FOR FEA SIMULATION

Property	Value (Unit)
Young's modulus (E)	1.33 (GPa)
Flexural modulus (E_f)	1.67 (GPa)
Poisson's Ratio	0.35
Shear Modulus (G)	$G = 0.4E = 0.4 \times 1330 = 532$ (MPa)
Tensile Strength (TS)	22.23 (MPa)
Shear Strength (S)	$S = 0.7TS = 0.7 \times 22.23 = 15.56$ (MPa)
Flexural Strength (σ)	43.11 (MPa)
Compressive Strength	428.49 (MPa)
Tensile specimen volume	$175 \times 25 \times 2.5 \text{ mm}^3 = 10.938$ (cm ³)
Flexural specimen volume	$76.2 \times 13 \times 4 \text{ mm}^3 = 3.962$ (cm ³)
5 Tensile specimen's mass	11.47g, 11.95g, 10.77g, 10.95g, 11.86g
Avg. Tensile specimen's mass	11.4g
Tensile Specimen's Density	$11.4/10.938 = 1.0425$ (g/cm ³)
5 Flexural specimen's mass	4.25g, 4.33g, 4.37g, 4.37g, 4.16g, 4.64g
Avg. Flexural specimen's mass	4.35g
Flexural Specimen's Density	$4.35/3.962 = 1.097$ (g/cm ³)

3.4.1 Tensile Properties FEA Simulation

The tensile properties simulation of LOM printed jute/PLA biocomposites involves utilizing computational methods and software to model and analyze the mechanical behavior of the composite material under tension. The tensile stress simulation aims to predict how the biocomposites will respond to tensile forces and provide valuable insights into their tensile strength, Young's modulus, and other relevant properties. The author used ANSYS ACP (Advanced Composite Preprocessor) to input Jute/PLA biocomposite material properties, geometric details, and boundary conditions, the simulation can simulate the behavior of the biocomposites during a tensile test. ANSYS ACP is a specialized module within the ANSYS software suite that is designed specifically for modeling, analyzing, and optimizing composite materials and structures.

In Section A, the initial step involves initiating the ACP module. Within this section, essential engineering data pertaining to the jute/PLA biocomposites, as outlined in Table V, is input. Then the geometry was done for jute/PLA biocomposites with 6 laminate stackup layers. In the model, the mesh was generated. In the setup section, all the layer's material properties were given and layer stackup of jute/PLA biocomposite materials was ensured. Then the setup was transferred to section B static structural. Here, the solution was done to find out the results. For the results, equivalent tensile stress and strain were simulated. Fig. 61 provides an illustrative overview of the project schematic detailing the FEA simulation procedures pertaining to the tensile specimen. A detailed overview of the distinctive tasks within each section is described below.

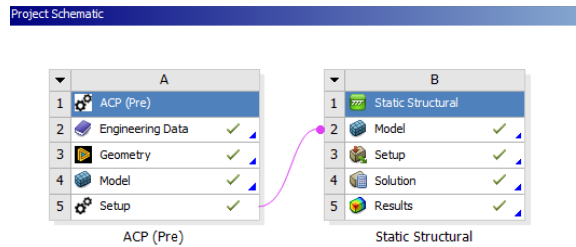


Fig. 61 Project schematic for the FEA simulation of LOM printed jute/PLA biocomposites tensile specimen.

After the material properties were assigned, the geometry of the jute/PLA tensile test specimen was done. The dimensions of the specimen was $175 \times 25 \times 2.5$ mm. The tensile specimen is made of 6 layers of jute/PLA biocomposite and each layer thickness was 0.42 mm. Fig. 62 shows the geometry of the single-layer jute/PLA tensile test specimen. After the geometry was done, the model moved to the setup part to create the remaining layers of the jute/PLA biocomposite specimens. After the first layer had been created in the geometry, the stackup option of the ANSYS ACP was used to create the remaining 5 layers to make it a 6-layer jute/PLA biocomposite tensile specimen. Fig. 63 shows the 5 layers stacked.



Fig. 62 Geometry of the single layer jute/PLA tensile test specimen in ANSYS.

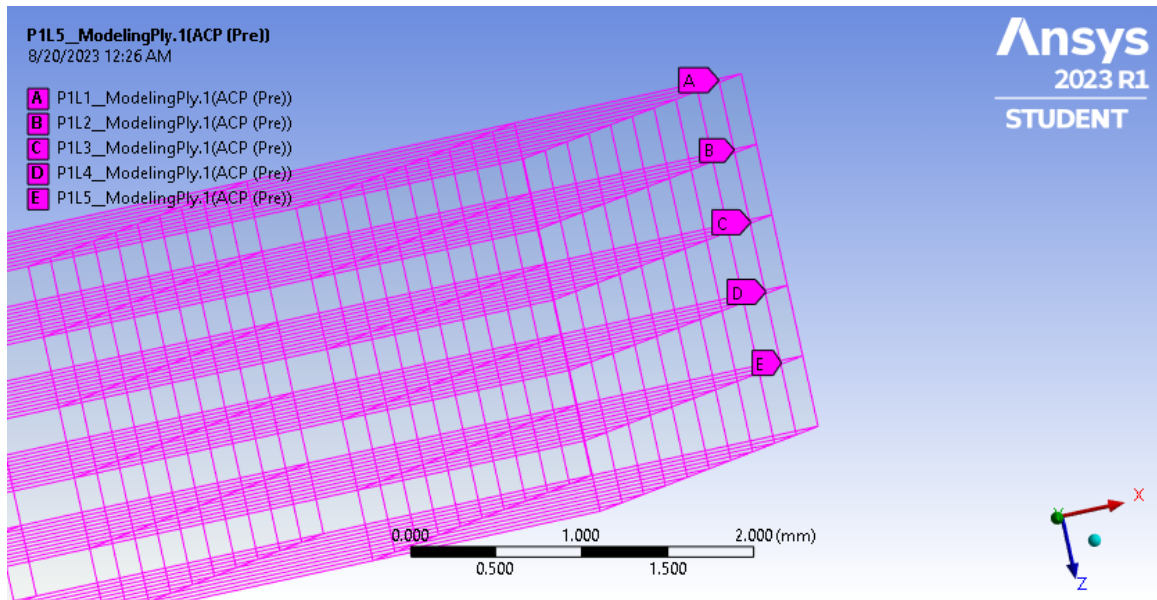


Fig. 63 Six-layer jute/PLA biocomposite tensile specimen.

After the establishment of the layer stackup, the mesh generation process was initiated within the geometric model. During the mesh creation, a prerequisite task involved the application of edge-sizing operations. The two vertical lateral edges of the composite specimens were subjected to 10 divisions each. Conversely, the two horizontal side edges underwent partitioning of 40 divisions attributed to each edge. After the mesh was done, face meshing was done to ensure a finer and more accurate representation of the interaction between fibers and matrix, as well as stress concentration around interfaces. Face meshing enables the capture of intricate features and localized effects within the model with greater accuracy. Fig. 64 shows the mesh of the biocomposite tensile specimen.

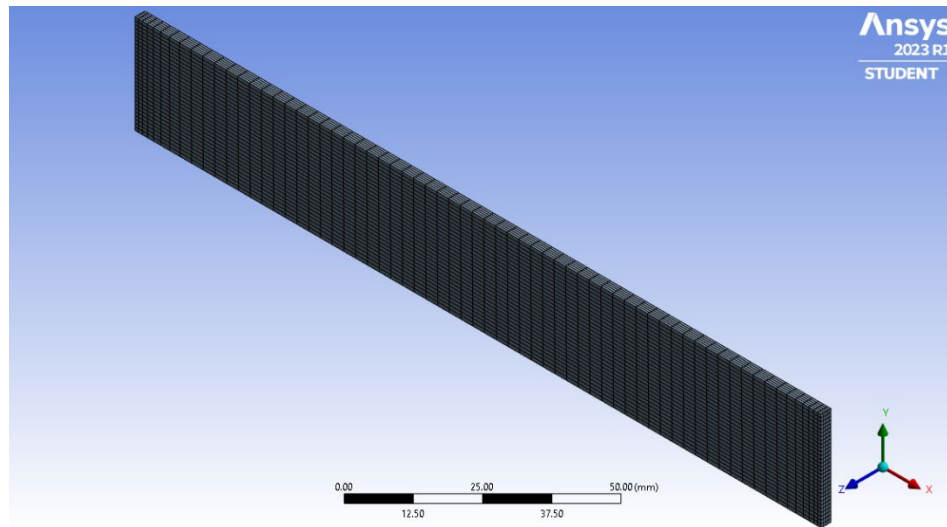


Fig. 64 Meshing of LOM printed jute/PLA biocomposites.

After meshing was done, ANSYS ACP setup and model were transferred to ANSYS Static Structural. The main purpose of ANSYS Static Structural is to predict how jute/PLA biocomposite tensile specimens will respond to applied forces, constraints, and displacements. First, the author defined the material properties such as Young's modulus, Poisson's ratio, and yield strength. The boundary conditions for this simulation were fixed constraint, and force. The fixed support was applied to one end of the composite. For the boundary conditions, one end of the biocomposite specimen was considered as fixed support and on the other hand force was applied. The amount of force applied in this tensile biocomposites specimen was 1,400N. Fig. 65 shows the fixed support that was done at one end of tensile specimen of biocomposite and Fig. 66 shows the 1,400N force applied to the other end.

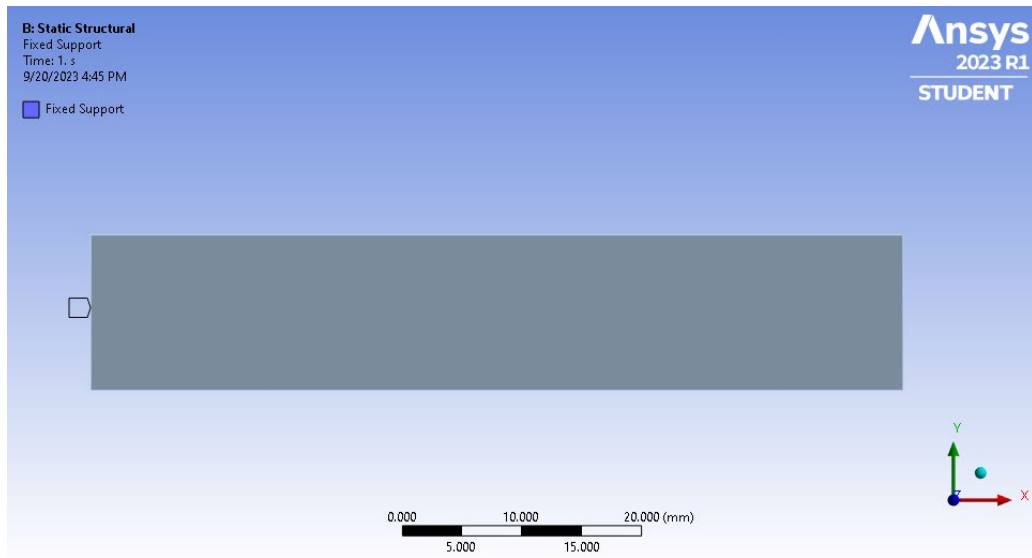


Fig. 65 Fixed support applied to one end of the jute/PLA biocomposite tensile specimen.

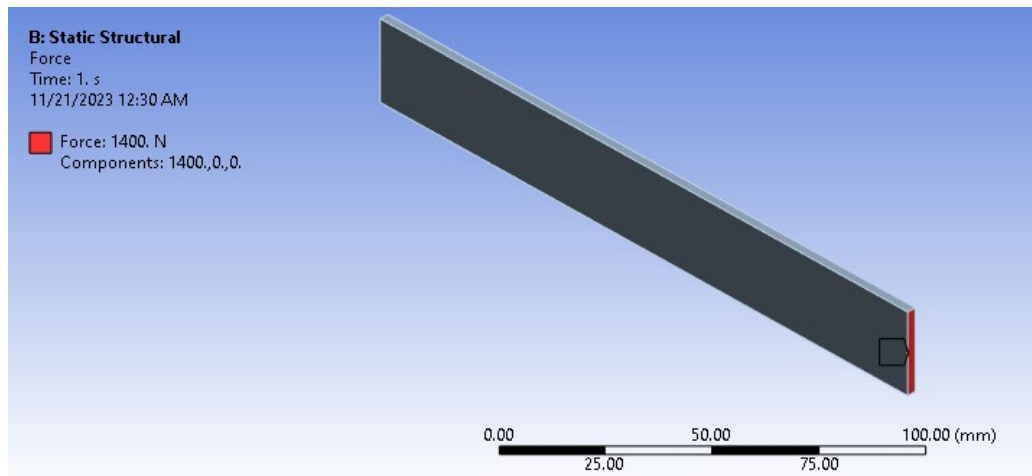


Fig. 66 Force applied to the other end of the jute/PLA biocomposite tensile specimen.

Following this, the finite element solver performed the simulation to compute equivalent (von Mises) tensile stress and equivalent elastic strain within the biocomposite specimen. This process provided valuable insights into the material's mechanical behavior. In Fig. 67 the distribution of tensile stress generated by the simulation is shown, while Fig. 68 illustrates the distribution of elastic strain.

The simulation results revealed that the average tensile stress experienced by the biocomposite specimen was approximately 23.598 MPa, with an average tensile strain of 1.75%. Force was applied to the cross-sectional area and that's why the simulation of average tensile stress and strain achieved the same color throughout the specimen.

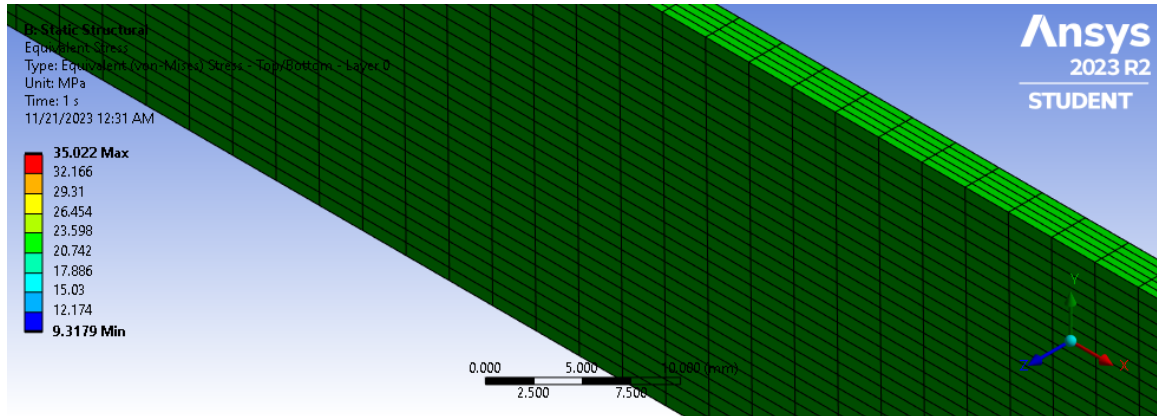


Fig. 67 Tensile stress FEA Simulation of LOM printed jute/PLA biocomposites.

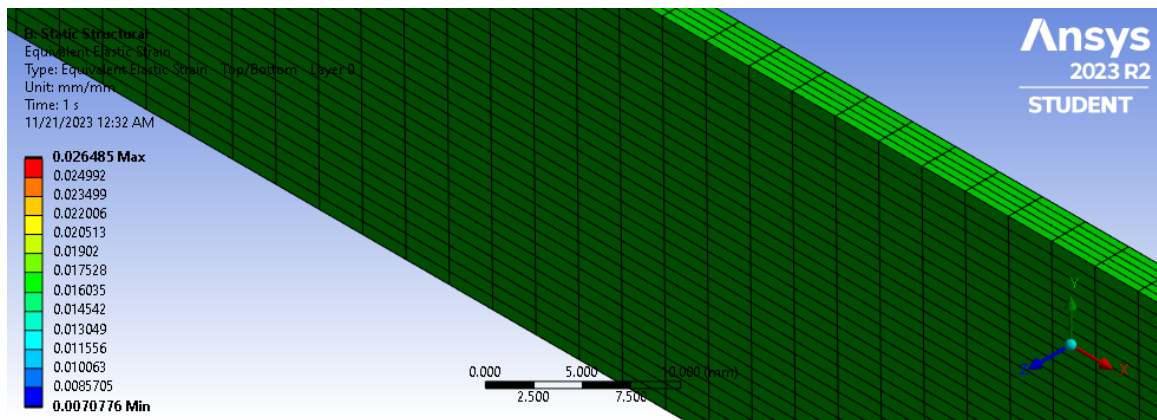


Fig. 68 Elastic strain FEA Simulation of LOM printed jute/PLA biocomposites.

3.4.2 The 3-point Bending Properties FEA Simulation

3-point bending properties refer to the flexural behavior exhibited by jute/PLA biocomposites. In this test, the jute/PLA biocomposite flexural specimen is supported at two points while a force is applied at the midpoint, causing the sample to bend. The

properties being evaluated typically include the load-displacement relationship, flexural strength, and flexural modulus. These properties provide insights into how the jute/PLA biocomposite flexural specimen behaves under bending forces. Similar to the tensile simulation, the geometry of the flexural specimen was created using ANSYS.

Fig. 69 presents an illustrative representation of the transformation process and schematic workflow conducted within the ANSYS Workbench for this study. In Section A designated as composite beam, the initial step involves initiating the ACP module. Within this section, essential engineering data pertaining to the jute/PLA biocomposites, as outlined in Table V, is input. Additionally, the geometric configuration for the 3-point bending test is established. A duplicate of this geometry is created in Section C to facilitate its transfer to Section D designated as load and supports, which is dedicated to the application of loads and supports. Subsequently, in Section A, all surfaces except the final one are removed, along with the load and support structures.

The model is then subjected to meshing processes on this single remaining surface layer, and material properties are assigned. Moving on to Section B, the primary action involves the transformation of the geometry to enable the implementation of the stackup option. Here, the stackup procedure was applied to create the 12 layers of jute/PLA biocomposite materials. In Section C, another geometric duplicate was generated, with the purpose of integrating the stackup-layered jute/PLA components into the 3-point bending geometry. Transitioning to Section D, the mechanical model was constructed. Within this model, meshing was conducted on the entire 3-point bending geometry, encompassing all laminate stackup layers of the jute/PLA biocomposite flexural specimen. The simulation then proceeds to Section E, designated as static structural, where the anticipated simulation

results are obtained. For the results, flexural stress and strain were simulated. A concise overview of the distinctive tasks within each section is described below.

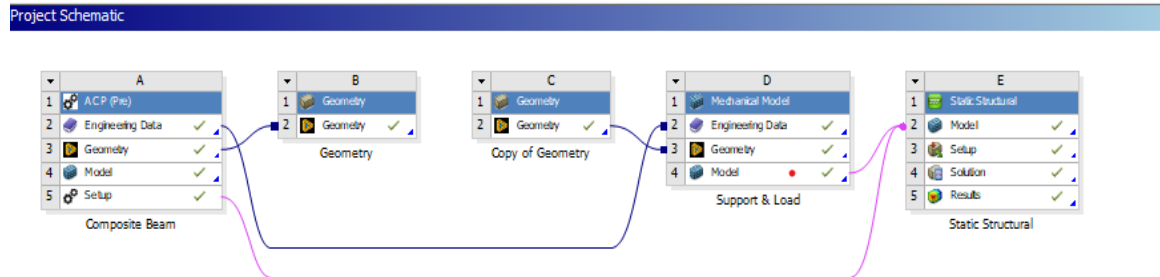


Fig. 69 Project schematic for the FEA simulation of LOM printed jute/PLA biocomposites flexural specimen.

For creating the geometry, the dimensions of the specimen were set at $76.2 \times 13 \times 4$ mm (ASTM D7264/D7264M-07 standard). For the materials for the specimen, jute/PLA biocomposite material properties were selected. Additionally, the load and two supporting points were configured with a diameter of 10 mm, with material properties data selected as Carbon Steel, 1020, annealed for the load and supports. Fig. 70 shows the geometry of the jute/PLA flexural specimen with one load and two supports.

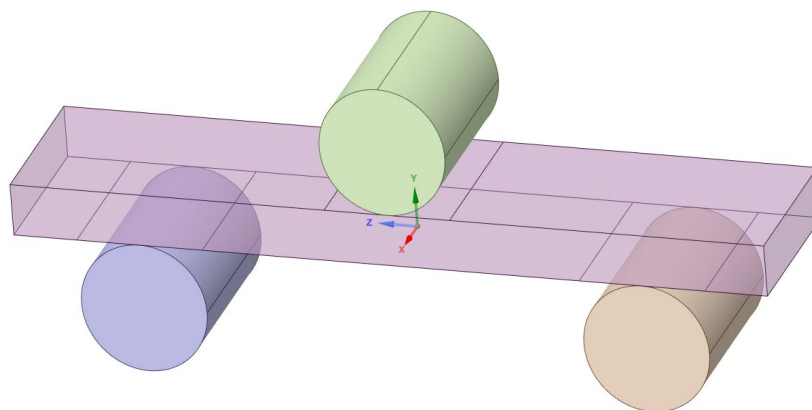


Fig. 70 Geometry of LOM printed jute/PLA biocomposites flexural specimen with a load and two supports.

Only one layer of jute/PLA biocomposite flexural specimen was taken out from the specimen to stack up the layers. Then, the meshing was done in that one layer of the flexural specimen to ensure that the mesh was fine enough to capture the bending behavior accurately in a single layer. Fig. 71 shows the single layer of flexural specimen and Fig.72 shows the single layer meshing.

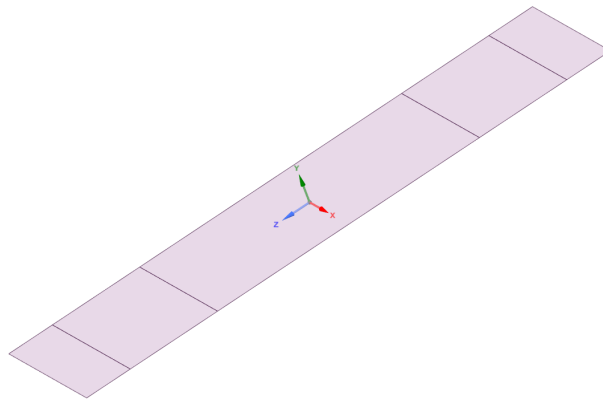


Fig. 71 Geometry of single-layer LOM printed jute/PLA biocomposites flexural specimen.

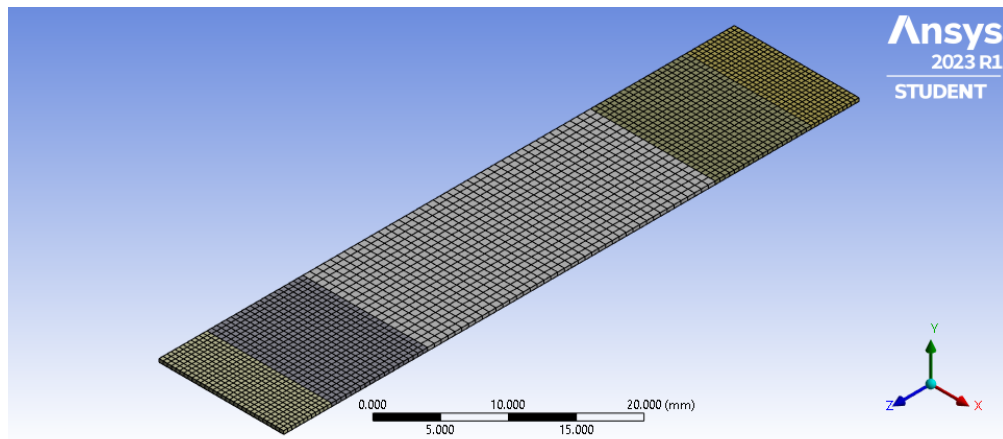


Fig. 72 Meshing of single-layer LOM printed jute/PLA biocomposites flexural specimen.

On this single-layer flexural specimen, 12 layers were stacked using the ANSYS ACP laminate stackup option. Each layer's thickness was 0.33 mm. Fig. 73 shows the first 10 layers of the 12 layers stackup in the jute/PLA biocomposite flexural specimen. Fig. 74

shows the remaining 2 layers. (ANSYS couldn't capture the image of all the 12 layers together. Due to this limitation, two figures are used.)

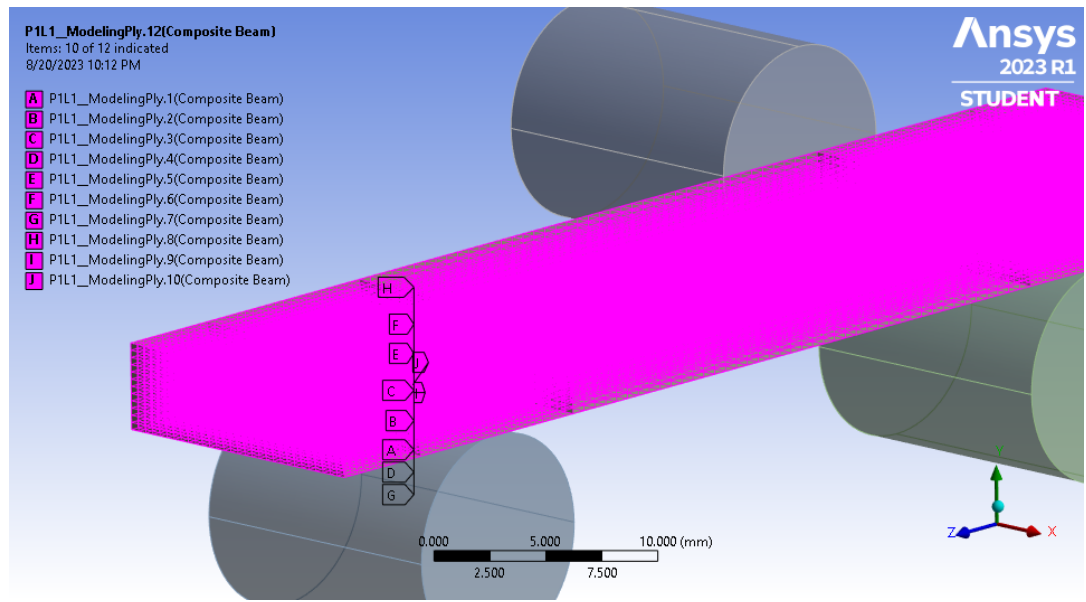


Fig. 73 Stacking of layers for the LOM printed jute/PLA biocomposites flexural specimen (first 10 of 12 layers).

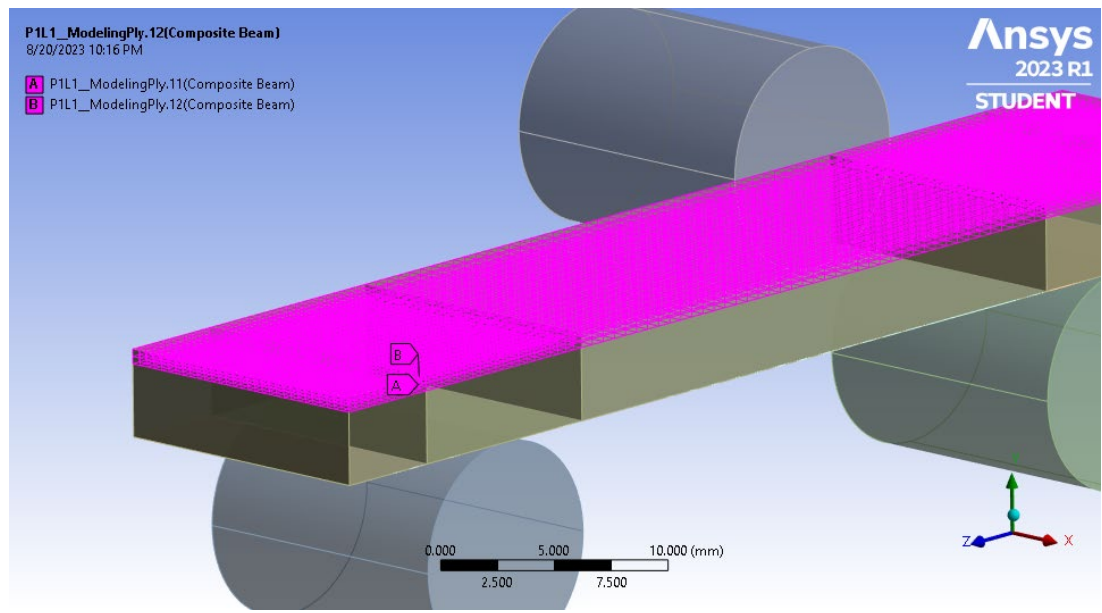


Fig. 74 Stacking of layers for the LOM printed jute/PLA biocomposites flexural specimen (final 2 of 12 layers).

Subsequently, the layering information was imported into the ANSYS mechanical model module (Section D) to create the mesh for the flexural specimen of the jute/PLA biocomposite. This meshing process encompassed both the stackup configuration as well as the incorporation of supports and applied loads. Fig. 75 shows the meshing generated for the LOM printed jute/PLA biocomposite flexural specimen. Then, the ANSYS static structural module (Section E) was used to do analysis settings and also the remote displacements in load and supports. Fig. 76 shows all the necessary remote displacements added to the load and supports.

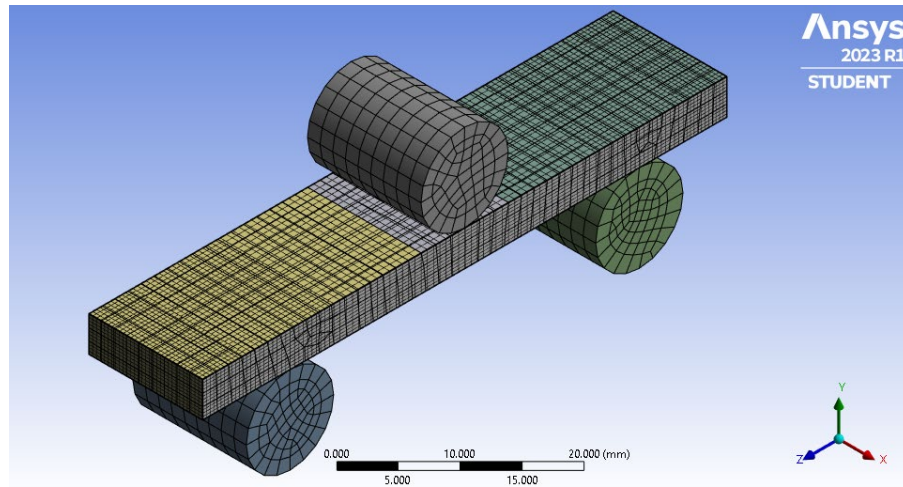


Fig. 75 Meshing for the FEA simulation of LOM printed jute/PLA biocomposites flexural specimen.

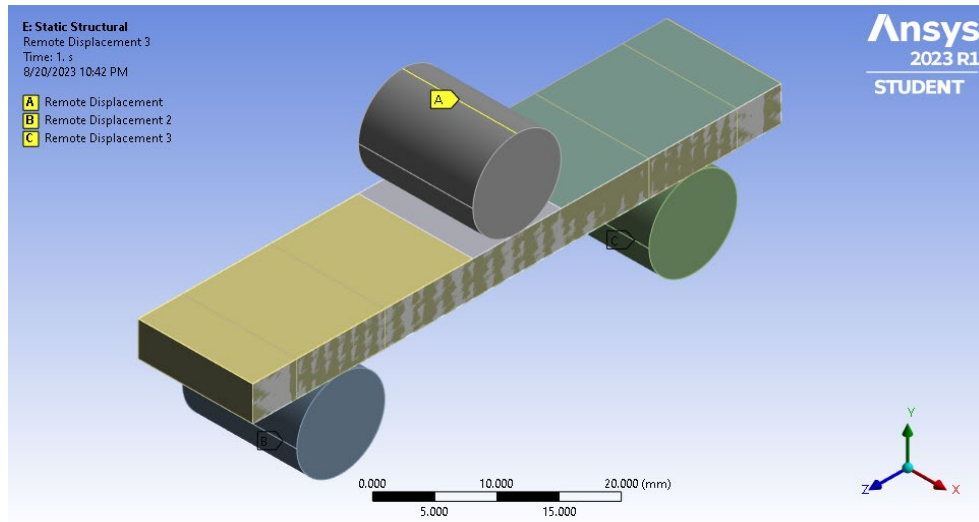


Fig. 76 Remote displacements applied in load and two supports for the FEA simulation.

Three remote displacements are applied in load and two supports and then the solver proceeded to calculate the equivalent flexural stress and strain using the von Mises criterion. The resulting equivalent flexural stress distribution illustrated in Fig. 77 and Fig. 78 displays the corresponding distribution of equivalent flexural strain within the biocomposite material. These data showed that the simulated maximum flexural stress of the 5 biocomposite flexural specimens is 55.06 MPa with maximum flexural strain at 4.91%.

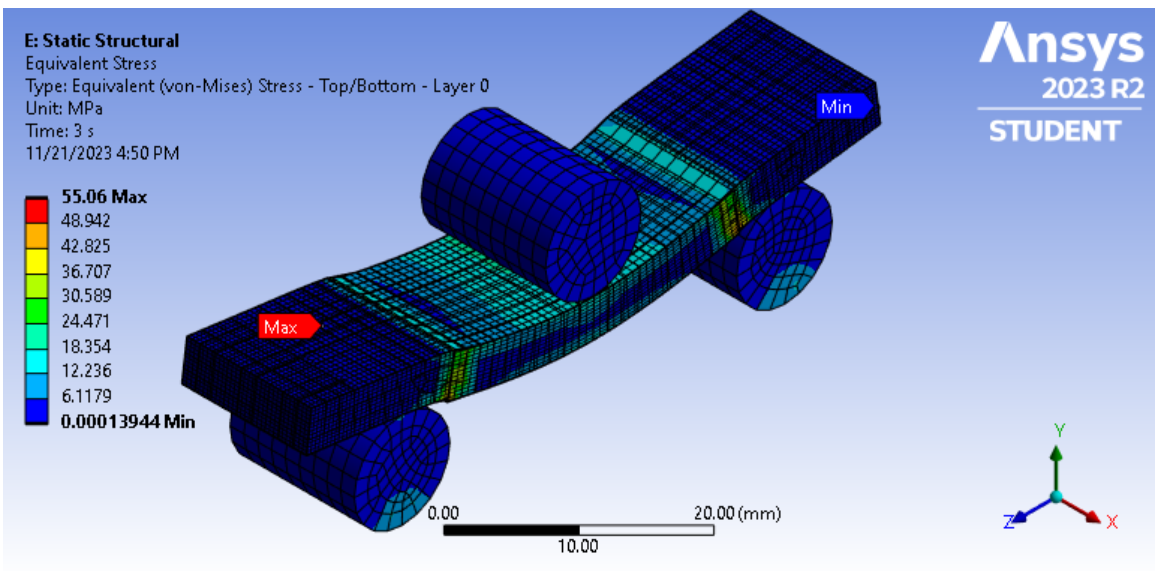


Fig. 77 Flexural stress FEA simulation of LOM printed jute/PLA biocomposites.

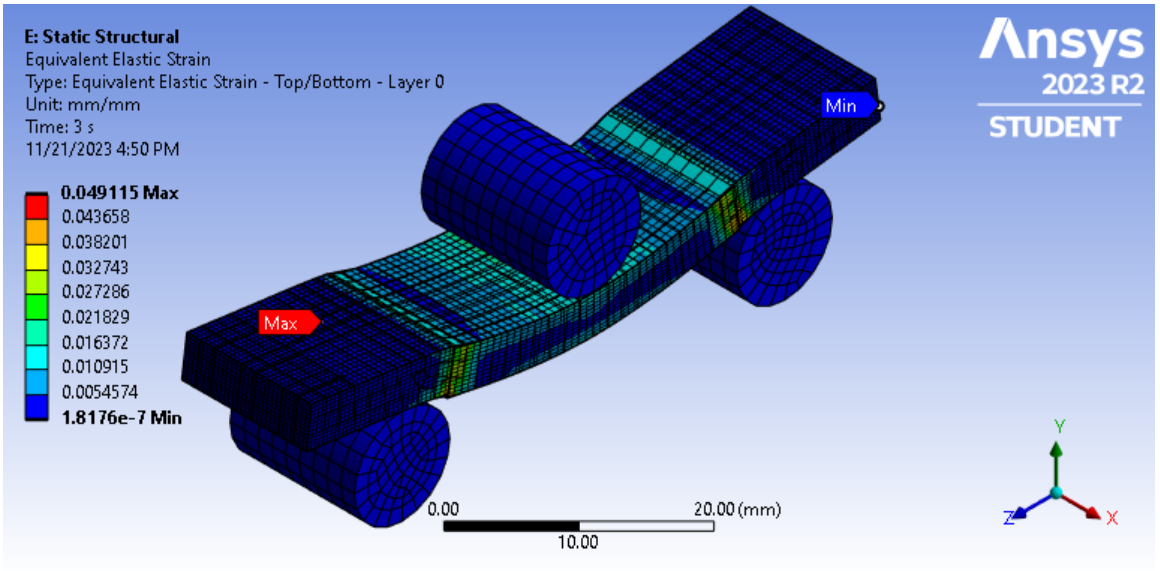


Figure 78 Flexural strain FEA simulation of LOM printed jute/PLA biocomposites.

CHAPTER 4

RESULTS AND DISCUSSIONS

The outcomes of all mechanical tests conducted in this investigation are documented in Table VI. LOM printed jute/PLA biocomposites showed significant improvement over both pure PLA printed parts and jute fiber. These improvements are particularly noteworthy in essential parameters such as tensile strength, elastic modulus, flexural strength, and flexural modulus. The data presented in the table unequivocally confirms that LOM printed jute/PLA biocomposites outperform both woven jute fiber and pure PLA printed specimens in these critical mechanical attributes. The comparisons of the mechanical properties between pure PLA, jute fabric, and LOM printed jute/PLA biocomposites are illustrated in Fig. 79.

TABLE VI
MECHANICAL PROPERTIES OF PLA AND JUTE/PLA SPECIMENS [110]

Material	Tensile Strength TS (MPa)	Elastic Modulus E (GPa)	Flexural Strength σ (MPa)	Flexural Modulus E_f (GPa)
Pure PLA	19.28	0.70	41.95	0.89
Jute fabric	15.05	0.19	N/A	N/A
Woven jute fiber- reinforced PLA (LOM Printed)	22.23	1.33	43.12	1.67

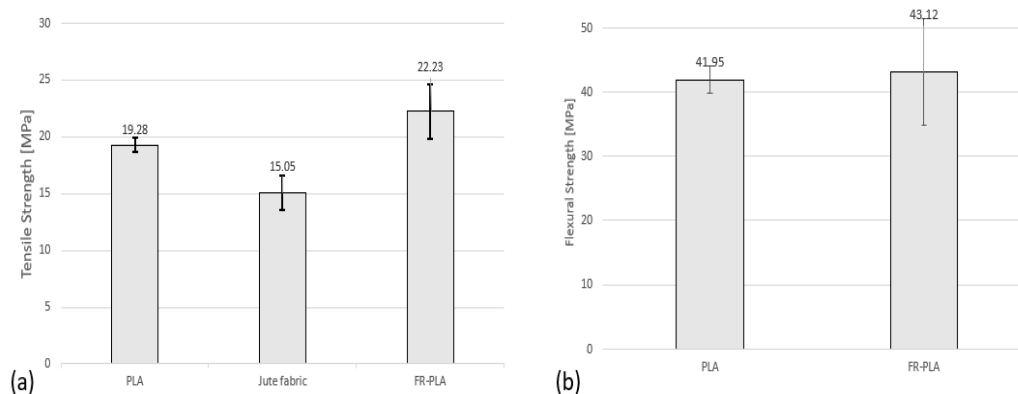


Fig. 79 Comparisons of (a) tensile, and (b) flexural strengths of pure PLA, jute fabric (tensile only), and fiber-reinforced PLA (FR-PLA) [110].

4.1 Tensile Test

The measured tensile properties of pure PLA, jute fabric, and jute fiber-reinforced composites are outlined in Table VI. It is evident that the tensile characteristics of 3D-printed pure PLA materials are relatively weak with achieving complete non-porosity in 3D-printed PLA components, as well as the flawless bonding of adjacent printed filaments. Furthermore, the measured tensile strength of jute fabric is also comparably lower than the numbers reported in prior research (300 – 700 MPa [112]), potentially due to the specific areal density of the jute fibers employed in this study and the absence of chemical treatment applied to the fabric.

The incorporation of woven jute reinforcement notably enhanced the tensile characteristics of pure PLA. The average tensile strength measured for the woven jute fiber-reinforced PLA polymer was 22.23 MPa, while the average elastic modulus was 1.33 GPa. These values demonstrate a substantial improvement compared to the properties of pure PLA whose average tensile strength was 19.28 MPa and the average elastic modulus

was 0.70 GPa. The stress-strain curves from the tensile tests conducted on both pure PLA and woven jute fiber-reinforced PLA are illustrated in Fig. 80.

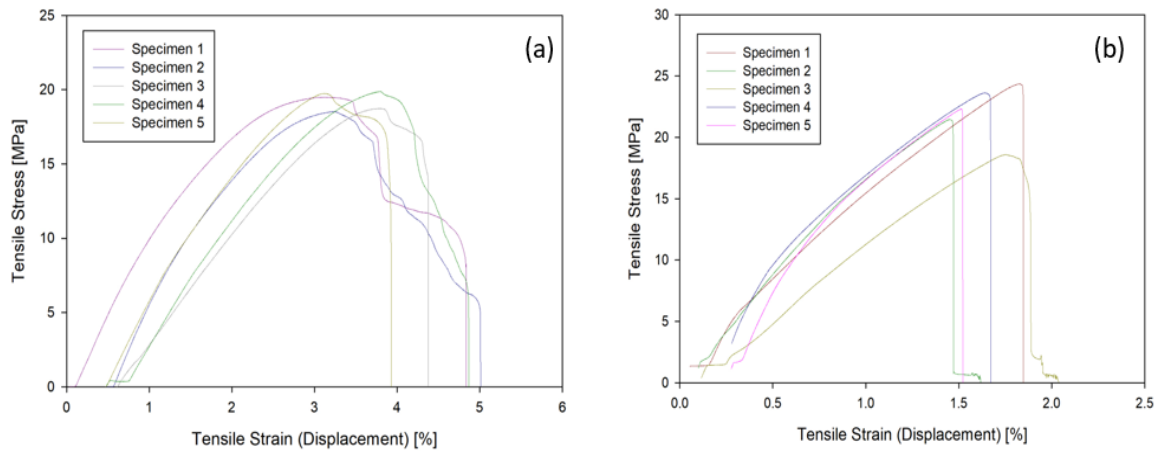


Fig. 80 Tensile test stress-strain curves (a) PLA, and (b) woven jute fiber-reinforced PLA [110].

In the stress-strain curve for pure PLA printed specimens the material undergoes elastic deformation and enters plastic deformation beyond the yield point under increasing stress. The ultimate tensile strength point is reached when the material experiences its highest resistance to deformation before it ruptures. All five pure PLA specimens' maximum tensile stress was below 20 MPa. The presence of jute fibers in the woven jute fiber-reinforced PLA specimens strengthens and toughens the material, leading to an extended initial elastic region and higher ultimate tensile strength, and the stress-strain curve may exhibit a more gradual decline due to the enhanced energy-absorbing capacity provided by the fibers, thus contributing to the overall structural integrity of the composite material. This is the reason the average tensile strength was higher than the pure PLA specimens.

To examine the mechanical properties of dry fiber, tensile tests were conducted. The average tensile strength, derived from the tensile data of five specimens, was found to

be 15.05 MPa. This information indicates that the tensile strength of jute is less than that of pure PLA. Therefore, to achieve greater tensile strength than that of either PLA or jute fiber alone, LOM printed jute/PLA specimens are preferable. Fig. 81 illustrates the tensile stress-strain curve for dry jute fiber.

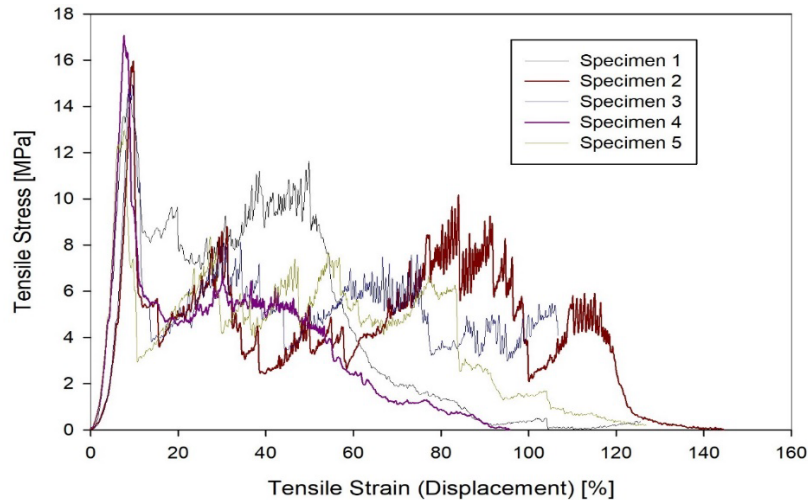


Fig. 81 Tensile stress-strain curves for natural jute fiber.

4.2 Flexural Test

The findings from the analysis of flexural strengths and moduli of both pure Polylactic Acid (PLA) samples and LOM printed woven jute/PLA biocomposites are presented in Table VI. The results of the analysis indicate that the flexural strength values of jute/PLA materials produced through LOM prototype are comparable to those obtained in previous studies (43.6 MPa – 59.6 MPa [113]). The flexural modulus values recorded in this study are significantly lower than those reported in other sources (2.96 GPa [114] – 4 GPa [115]). It was found that the flexural properties of pure PLA experienced a marginal enhancement from the application of woven jute reinforcement. Specifically, the average flexural strength registered a value of 43.12 MPa for the woven jute fiber-reinforced PLA

polymer, while the flexural modulus underwent a notable increase to 1.67 GPa (representing an 87.6% increment). The result from the flexural stress strain curve shows that the woven jute fiber reinforced PLA is scattered compared to that of pure PLA. The author assumes it may be due to inconsistency in hand lay-up fabrication and poor jute fiber quality. The reason for this result is the poor bindings among reinforcement fabrics compared to pure PLA 3D-printed parts. The stress-strain curves of flexural tests performed on pure PLA and woven jute fiber-reinforced PLA are shown in Fig. 82.

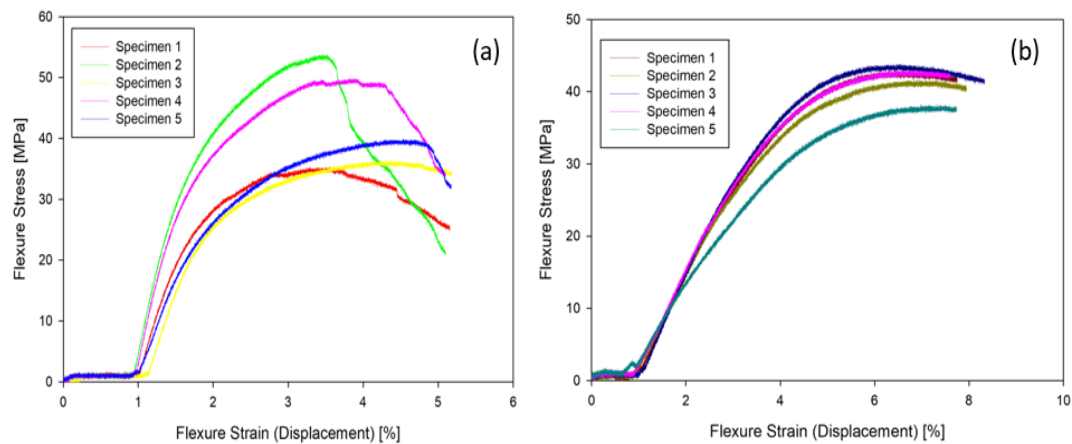


Fig. 82 Flexural test stress-strain curves of (a) woven jute fiber-reinforced PLA, and (b) pure PLA [110].

The flexural stress-strain curves provide insights into the material's response to bending stress and deformation. Through a comparative analysis of the stress-strain curves generated from conducting flexural tests on pure PLA and PLA reinforced with woven jute fibers, the influence of the added fibers on the flexural behavior of the material is clearly shown. These curves highlighted the reinforcing effects that the woven jute fibers have on strengthening the mechanical properties of the PLA polymer.

4.3 SEM Imaging

The SEM imaging findings are illustrated in Fig. 80 below, capturing crucial details about the LOM printed jute/PLA biocomposites. As depicted in Fig. 83(a), where the magnification is set at 700, it becomes evident that the PLA polymer matrix is properly infused and interlinked with the jute fibers. The natural texture and structure of the jute fibers are observable. However, there are conspicuous voids present at various locations within the composites. These voids hinder the direct contact and cohesive bonding between the reinforcing fibers and the polymer matrix. Based on this observation, the author assumes that this factor might be among the reasons why the mechanical properties of the jute/PLA biocomposites are not exhibiting a substantial surpassing of the anticipated flexural strength. The existence of these voids might contribute significantly to the mechanical properties of the jute/PLA biocomposites falling short of expectations, particularly in terms of flexural strength. These voids disrupt the seamless interaction between the fibers and the matrix, thereby potentially impeding the material's structural integrity and load-bearing capabilities.

Furthermore, at an even more intricate magnification level of 1,500 showcased in Fig. 83(b), a segment with PLA infused properly with jute fiber is shown. In this specific section, there are no gaps between the reinforcing jute fibers and the PLA biopolymer. Consequently, the interaction between the fibers and the matrix exhibits a high degree of cohesion and binding. This microstructural analysis provides invaluable insights into the intricacies of the composite's internal composition and offers a clearer understanding of how the fiber-matrix interface impacts the material's overall mechanical performance. By scrutinizing these SEM images of jute fibers and PLA, the overall behavior and

performance of composite materials that incorporate jute fibers and PLA are evaluated properly.

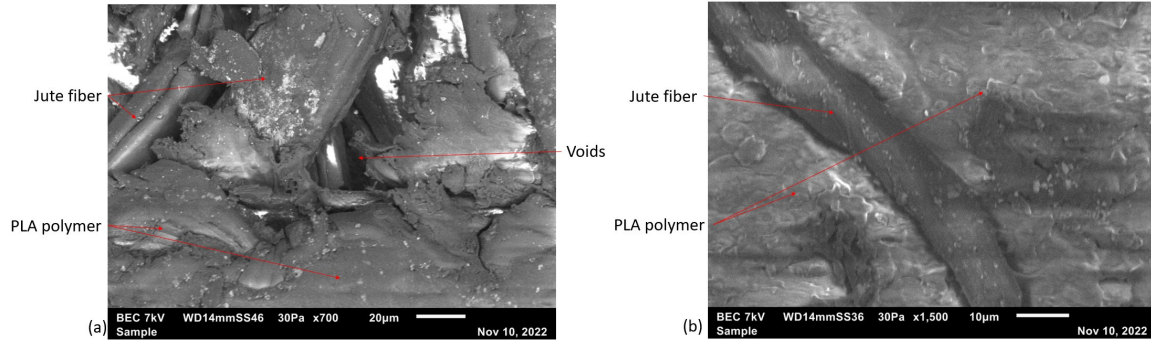


Fig. 83 SEM imaging of (a) jute fiber and PLA polymer with voids ($\times 700$), and (b) the interface of jute reinforcement fiber and PLA polymer matrix ($\times 1,500$) [110].

4.4 Discussion of The Stress Fields Obtained From The FEA Simulation

The comparative analysis between FEA simulation and experimental findings reveals a noteworthy alignment in results. The average tensile stress was recorded at 23.598 MPa with a tensile strain of 1.75% in the FEA simulation. The average value of the maximum experimental tensile stress of the 5 specimens was 22.23 MPa and the average tensile strain was 1.67%. The maximum flexural stress FEA simulated result was 55.06 MPa. The FEA results closely resembled the experimental data for 5 flexural specimens with a maximum flexural stress of 53.81 MPa. The FEA simulated maximum flexural strain was 4.91% and the experimental maximum flexural strain of 5 specimens was 5.18%. Table VII shows the FEA simulated data and experimental results comparison of LOM printed jute/PLA.

TABLE VII
COMPARISON OF FEA SIMULATED DATA AND THE EXPERIMENTAL DATA

Mechanical Properties	FEA Simulation	Experimental Results
Tensile Stress	23.598 MPa (Average)	22.23 MPa (Average of the five specimen's maximum tensile stress)
Tensile Strain	1.75% (Average)	1.67% (Average of the five specimen's maximum tensile strain)
Flexural Stress	55.06 MPa (maximum)	53.81 MPa (Maximum flexural stress of 5 flexural specimens)
Flexural Strain	4.91%	5.18% (Maximum flexural strain of 5 flexural specimens)

The congruence between FEA simulation and experimental LOM printed jute/PLA biocomposites can be attributed to several key factors that contribute to the accuracy and reliability of the simulation, aligning it closely with the actual experimental results.

1. Material properties: Accurate material properties are essential for a successful simulation. The engineering data of the FEA of jute/PLA biocomposites was assigned for the mechanical properties of jute fibers, PLA polymer, and their interaction.

2. Geometry and layering: LOM printing involves layer-by-layer fabrication. Accurately representing the layer-by-layer geometry in the FEA model ensures that the simulation mimics the actual process. For tensile properties, 6 layers of jute/PLA biocomposites were properly ensured with accurate material properties for each layer. Similarly, 12 layers were considered for the jute/PLA biocomposite flexural specimen. For each layer, layer thickness, and orientation were defined properly. FEA simulation achieved the desired experimental output by applying ply stackup and orientation properly.
3. Layer bonding and interfaces: LOM-printed jute/PLA biocomposites consist of multiple layers bonded together. The simulation must capture the behavior of each layer and the interactions between them. The author ensured proper bonding and interlayer interfaces in the simulation.
4. Loading and boundary conditions: Replicating the loading conditions applied during the experimental tests is crucial. The author properly defined the external forces, constraints, and interactions that the biocomposites experience to ensure that the simulation closely matches the experimental output. In the flexural specimen 3-point bending test simulation, the author ensured proper load and support in the specimen so that it could replicate the experimental properties of the flexural specimen.
5. Meshing quality: Just like any FEA analysis, a high-quality mesh is essential for the jute/PLA Biocomposites simulation. The author ensured a proper number of divisions on horizontal and vertical edges by using the Ansys edge sizing option. Then face meshing was done to ensure critical areas or features of the geometry

were represented with a finer mesh. Edge sizing and face meshing can allow for more accurate analysis in those regions to capture stress concentrations and strain variations accurately so that it can prevent numerical errors and deliver more reliable results.

In summary, when these factors align, FEA simulations become a powerful tool to predict the mechanical behavior of LOM-printed biocomposite materials, aiding in design optimization and performance prediction.

CHAPTER 5

CONCLUSIONS

Through a comprehensive exploration of the mechanical characteristics of both the pure PLA polymer and the LOM printed woven jute fiber-reinforced PLA composites, several key conclusions can be drawn:

1. The tensile and flexural properties of the pure PLA polymer samples appear comparatively weak. This phenomenon can be attributed to the inherent challenges of achieving solid test specimens through the FDM 3D printing technique, which may result in porosity within the material.
2. The jute fabrics utilized in this investigation exhibit weaker mechanical properties than those documented in prior studies. This divergence could be attributed to processing variations applied by the fabric supplier. To enhance the quality of the biocomposites, it is recommended to procure and incorporate higher-grade natural fiber fabrics.
3. Integrating woven jute fibers into PLA polymers via the LOM 3D printing process yields a substantial improvement in tensile properties, with a nearly twofold enhancement in tensile modulus. This enhancement is primarily attributed to the reinforcing influence of the woven jute fibers. However, marginal improvements in flexural properties were observed due to poor interlaminar bonding.
4. While the fiber-matrix interface binding within the biocomposites produced in this research is generally favorable, there remain regions with voids where the jute fiber and PLA polymer do not make contact. Therefore, these regions exhibit no binding,

consequently limiting further enhancements in the mechanical properties of the biocomposites.

5. The FEA simulation outcomes concerning the maximum tensile and flexural strength closely align with the empirical results obtained. This congruence between simulated and experimental data enhances the credibility of the simulation model and its predictive capabilities.

In summary, the results of this research demonstrate enhanced mechanical characteristics in LOM 3D printed woven jute/PLA biocomposites. However, the mechanical properties of the woven fabric employed in this research, as indicated by the pure jute fiber tests, were relatively low. Additionally, the presence of significant voids in the fabricated samples adversely affected fiber/matrix adhesion, constraining the potential for further advancements in the mechanical attributes of LOM-produced biocomposites. FEA simulation proved that the experimental results were accurate based on the mechanical properties of woven jute fiber and PLA polymer. A better quality of woven jute fiber with good bonding with PLA biopolymer will ensure higher mechanical properties for the LOM printed jute/PLA biocomposite. The research team for this research will keep on working to improve the LOM prototype and 3D print other natural fiber (e.g., flax, hemp, etc.) reinforced biocomposites.

REFERENCES

- [1] C. . M. Gonzalez, "Additive Manufacturing Trends: Looking Back at 2021 and Ahead on 2022," The American Society of Mechanical Engineers, 04 January 2022. [Online]. Available: <https://www.asme.org/topics-resources/content/additive-manufacturing-trends-looking-back-at-2021-and-ahead-on-2022>.
- [2] A. Lotfi, H. Li, D. Dao and G. Prusty, "Natural fiber-reinforced composites: A review on material, manufacturing, and machinability," *J. Thermoplastic Composites Mat.*, vol. 34, no. 2, pp. 238-284, 2019.
- [3] M. Groover, "Rapid Prototyping and Additive manufacturing," in *Fundamentals of Modern Manufacturing*, Danvers, MA, John Wiley & Sons, 2016.
- [4] I. Gibson, D. Rosen, B. Stucker and A. Khorasani, *Additive Manufacturing Technologies.*, 2020.
- [5] S. Dalbehera and S. Acharya, "Study on mechanical properties of natural fiber reinforced woven jute-glass hybrid epoxy composites.," *Adv. Polymer Sci. Tech.*, vol. 4, no. 1, pp. 1-6, 2014.
- [6] X. Jiang, Y. Luo, X. Tian, D. Huang, N. Reddy and Y. Yang, in *Poly(Lactic Acid): Synthesis, Structures, Properties, Processing, and Applications.*, John Wiley & Sons,, 2010.
- [7] T. Casalini, F. Rossi, A. Castrovinci and G. Perale, "A Perspective on Polylactic Acid-Based Polymers Use for Nanoparticles Synthesis and Applications.," *Front. Bioeng. Biotechnol.*, vol. 7, p. 259, 2019.
- [8] I. 17296-2., "Additive manufacturing general principle's part 2: overview of process categories and feedstock.," in *Additive manufacturing — General principles.*, 2015.
- [9] M. Pagac, J. Hajnys, Q.-P. Ma, L. Jancar, J. Jansa, P. Stefek and J. Mesicek, "A Review of Vat Photopolymerization Technology: Materials, Applications, Challenges, and Future Trends of 3D Printing," *Polymers*, vol. 13, no. 4, p. 598, 2021.
- [10] A. Al Rashid, W. Ahmed, M. Y. Khalid and K. Muammer, "Vat photopolymerization of polymers and polymer composites: Processes and applications," *Additive Manufacturing*, vol. 47, p. 102279, 2021.
- [11] B. Yilmaz, A. Al Rashid, A. M. Younss, Z. Evis and M. Koc, "Bioprinting: A review of processes, materials and applications," *Bioprinting*, vol. 23, 2021.

- [12] B. Mummareddy, M. Maravola, E. MacDonald, J. Walker, B. Hetzel, B. Conner and P. Cortes, "The fracture properties of metal-ceramic composites manufactured via stereolithography," *Int J Appl Ceram Technol.*, vol. 17, pp. 413-423, 2020.
- [13] S. Mubarak, D. Dhamodharan, N. Divakaran, M. . B. Kale, T. Senthil, L. Wu and J. Wang, "Enhanced Mechanical and Thermal Properties of Stereolithography 3D Printed Structures by the Effects of Incorporated Controllably Annea," *Nanomaterials*, vol. 10, no. 1, p. 79, 2020.
- [14] B. Nagarajan, P. Mertiny and A. J. Qureshi, "Magnetically loaded polymer composites using stereolithography—Material processing and characterization," *Materials Today Communications*, vol. 25, p. 101520, 2020.
- [15] T. Zhao, R. Yu, S. Li, X. Li, X. Zhang, X. Zhao, C. Wang, Z. Liu, R. Dou and W. Huang, "Superstretchable and Processable Silicone Elastomers by Digital Light Processing 3D Printing," *ACS Appl. Mater. Interfaces*, vol. 11, no. 15, p. 14391–14398, 2019.
- [16] J. Xiao, Y. Jia, D. Liu and H. Cheng, "Three-dimensional printing of SiCN ceramic matrix composites from preceramic polysilazane by digital light processing," *Ceramics International*, vol. 46, no. 16, pp. 25802-25807, 2020.
- [17] S. Asif, P. Chansoria and R. Shirwaiker, "Ultrasound-assisted vat photopolymerization 3D printing of preferentially organized carbon fiber reinforced polymer composites," *Journal of Manufacturing Processes*, vol. 56, no. B, pp. 1340-1343, 2020.
- [18] D. Dev Singh, T. Mahender and A. Raji Reddy , "Powder bed fusion process: A brief review.," *Materials Today: Proceedings.*, vol. 46, no. ISSN 2214-7853, pp. 350-355, 2021.
- [19] B. Bewlay, S. Nag, A. Suzuki and M. Weimer, " TiAl alloys in commercial aircraft engines," *Mater. High Temp.* , vol. 33, p. 549–559, 2016.
- [20] H. Attar, K. G. Prashanth, L.-C. Zhnag, M. Calin, I. V. Okulov, S. Scudino , C. Yang and J. Eckert, "Effect of Powder Particle Shape on the Properties of In Situ Ti–TiB Composite Materials Produced by Selective Laser Melting," *Journal of Materials Science & Technology*, vol. 31, no. 10, pp. 1001-1005, 2015.
- [21] B. Zhang, G. Bi, S. Nai, C.-N. Sun and J. Wei, "Microhardness and microstructure evolution of TiB₂ reinforced inconel 625/TiB₂ composite produced by selective laser melting.," *Opt. Laser Technol.*, vol. 80, pp. 186-195, 2016.
- [22] K. Prashanth, S. Scudino and J. Eckert, "Defining the tensile properties of Al-12Si parts produced by selective laser melting," *Acta Mater.*, vol. 126, pp. 25-35, 2017.

- [23] K. Ruben Bayu, F. Imaduddin, A. Fitriani, U. Dody and Z. Arifin, "A review on the fused deposition modeling (FDM) 3D printing: Filament processing, materials, and printing parameters," *Open Engineering.*, vol. 11, no. 1, 2021.
- [24] F. Ning, W. Cong, J. Qiu, J. Wei and S. Wang, "Additive manufacturing of carbon fiber reinforced thermoplastic composites using fused deposition modeling," *Composites Part B: Engineering*, vol. 80, pp. 369-378, 2015.
- [25] S. Woosley, N. Abuali Galehdari, A. Kelkar and S. Aravamudhan, "Fused deposition modeling 3D printing of boron nitride composites for neutron radiation shielding," *Journal of Materials Research*, vol. 33, no. 22, pp. 3657-3664, 2018.
- [26] W. Zhong, F. Li, Z. Zhang, L. Song and L. Zhimin, "Short Fiber Reinforced Composites for Fused Deposition Modeling.," *Mater. Sci. Eng.*, vol. 29, pp. 181-183, 2001.
- [27] P. Wang, B. Zou, S. Ding, C. Huang, Z. Shi, Y. Ma and P. Yao, "Preparation of Short CF/GF Reinforced PEEK Composite Filaments and Their Comprehensive Properties Evaluation for FDM-3D Printing.," *Compos. Part B Eng.*, vol. 198, p. 108175, 2020.
- [28] L. Mohammed, M. Ansari, G. Pua, M. Jawaaid and M. Islam, "A review on natural fiber reinforced polymer composite and its applications," *Int. J. Polym. Sci.* , 2015.
- [29] R. Zhang, L. Yu, K. Chen, P. Xue, M. Jia and Z. Hua, "Amelioration of interfacial properties for CGF/PA6 composites fabricated by ultrasound-assisted FDM 3D printing," vol. 39, 2023.
- [30] L. Cao, J. Xiao, J. K. Kim and X. Zhang, "Effect of post-process treatments on mechanical properties and surface characteristics of 3D printed short glass fiber reinforced PLA/TPU using the FDM process," *CIRP Journal of Manufacturing Science and Technology*, vol. 41, pp. 135-143, 2023.
- [31] M. A. S. R. Saadi, A. Maguire, N. T. Pottackal, M. S. H. Thakur, M. Md., A. J. Hart, P. M. Ajayan and M. M. Rahman, "Direct Ink Writing: A 3D Printing Technology for Diverse Materials.," *Adv. Mater.*, vol. 34, 2022.
- [32] S. T., P. J.A. and N. M., "High-resolution PLA-based composite scaffolds via 3-D printing technology," *Acta Biomaterialia*, vol. 9, no. 3, pp. 5521-5530, 2013.
- [33] L. Zhang, G. Yang, B. Johnson and X. Jia, "Three-dimensional (3D) printed scaffold and material selection for bone repair.," *Acta Biomater.*, vol. 84, pp. 16-33, 2019.

- [34] G. Diogo, V. Gaspar, I. Serra, R. Fradique and I. Correia, "Manufacture of β -TCP/alginate scaffolds through a Fab@home model for application in bone tissue engineering. Biofabrication.," vol. 6, no. 2, 2014.
- [35] I. D. Robertson, M. Yourdkhani, P. J. Centellas, J. E. Aw, D. G. Ivanoff, E. Goli, E. M. Lloyd, L. M. Dean and N. R. Sottos, "Rapid energy-efficient manufacturing of polymers and composites via frontal polymerization.," *Nature*, vol. 557, p. 223–227, 2018.
- [36] S. Chandrasekaran, E. B. Duoss, M. A. Worsley and J. P. Lewicki, "3D printing of high performance cyanate ester thermoset polymers," *J. Mater. Chem. A*, vol. 6, no. 3, pp. 853-858, 2018.
- [37] S. Guo, F. Gosselin, N. Guerin, A. Lanouette, M. Heuzey and D. Therriault, "Solvent-cast three-dimensional printing of multifunctional microsystems.," *Small*, vol. 9, no. 24, pp. 4118-22, 2013.
- [38] J. Dilag, T. Chen, S. Li and S. Bateman, " Design and direct additive manufacturing of three-dimensional surface micro-structures using material jetting technolog," *Addit. Manuf.*, vol. 27, pp. 167-174, 2019.
- [39] X. Shen and H. Naguib, "A robust ink deposition system for binder jetting and material jetting," *Addit. Manuf.*, vol. 29, 2019.
- [40] S. Saleh Alghamdi, S. John, N. Roy Choudhury and N. K. Dutta, "Additive Manufacturing of Polymer Materials: Progress, Promise and Challenges.," *Polymers*, vol. 13, no. 5, p. 753.
- [41] D. S. 3ds., "Introduction to Material Jetting — MJ, NPJ, DOD," 2022. [Online]. Available: <https://www.3ds.com/make/guide/process/material-jetting>.
- [42] R. Vdovin, T. Tomilina, V. Smelov and Laktionova, "M. Implementation of the additive PolyJet technology to the development and fabricating the samples of the acoustic metamaterials," *Procedia Eng.*, vol. 176, p. 595–599, 2017.
- [43] H. Kitamori, I. Sumida, T. Tsujimoto and H. Shimamoto, "Evaluation of mouthpiece fixation devices for head and neck radiotherapy patients fabricated in PolyJet photopolymer by a 3D printer.," *Phys. Med.*, vol. 58, pp. 90-98, 2019.
- [44] D. Hong, S. Lee, T. Kim, J. Hwan, Y. Lee and K. Chung, "Development of a personalized and realistic educational thyroid cancer phantom based on CT images: An evaluation of accuracy between three different 3D printers.," *Comput. Biol. Med.* , vol. 113, 2019.
- [45] C. Cramer, P. Nandwana, R. Lowden and A. Elliott, "Infiltration studies of additive manufacture of WC with Co using binder jetting and pressureless melt method," *Addit. Manuf.* , vol. 28, p. 333–343, 2019.

- [46] L. Tan, W. Zhu and K. Zhou, "Recent Progress on Polymer Materials for Additive" Manufacturing.," *Adv. Funct. Mater.*, vol. 30, 2020.
- [47] Y. Bai and C. Williams, "An exploration of binder jetting of copper," *Rapid Prototyping Journal.*, vol. 21, no. 2, pp. 177-185, 2015.
- [48] N. Parab, J. Barnes and C. Zhao, "Real time observation of binder jetting printing process using high-speed X-ray imaging.," *Sci Rep*, vol. 9, p. 2499, 2019.
- [49] Hubs., "What is Binder Jetting 3D printing?," Hubs., 2021. [Online]. Available: <https://www.hubs.com/knowledge-base/introduction-binder-jetting-3d-printing/#:~:text=Metal%20Binder%20Jetting%20is%20up%20to%2010x%20more,during%20printing%2C%20enabling%20the%20creation%20of%20complex%20geometries..>
- [50] Q. Porter, M. Moghadasi, Z. Pei and C. Ma, "Dense and strong ceramic composites via binder jetting and spontaneous infiltration," *Ceramics International*, vol. 49, no. 11, pp. 17363-17370, 2023.
- [51] J. Liu, P. Li, D. Jin, S. Her, J. Kim, Y. Yoon, M. Baldassari and S. Bae, "Evaluation of the mechanical and photocatalytic properties of TiO₂-reinforced cement-based materials in binder jet 3D printing," *Journal of Building Engineering*, vol. 72, 2023.
- [52] K. M. Rahman, A. Wei, H. Miyanaji and C. B. Williams, "Impact of binder on part densification: Enhancing binder jetting part properties through the fabrication of shelled geometries," *Additive Manufacturing*, vol. 62, 2023.
- [53] D. Svetlizky, M. Das, B. Zheng, A. Vyatskikh, S. Bose, A. Bandyopadhyay, J. Schoenung, E. Lavernia and N. Eliaz, "Directed energy deposition (DED) additive manufacturing: Physical characteristics, defects, challenges and applications," *Mater. Today.*, vol. 49, p. 271–295, 2021.
- [54] D.-G. Ahn, "Directed Energy Deposition (DED) Process: State of the Art," *International Journal of Precision Engineering and Manufacturing-Green Technology* volume, vol. 8, pp. 703-742, 2021.
- [55] A. R. McAndrew, M. A. Rosales, P. A. Colegrove, J. R. Hönnige, A. Ho, R. Fayolle, K. Eyitayo, I. Stan, P. Sukrongpang, A. Crochemore and Z. Pinter, "Interpass rolling of Ti-6Al-4V wire + arc additively manufactured features for microstructural refinement," *Additive Manufacturing*, vol. 21, pp. 340-349, 2018.
- [56] J. Pragana, R. Sampaio, I. Bragança, C. Silva and P. Martins, "Hybrid metal additive manufacturing: A state-of-the-art review," *Advances in Industrial and Manufacturing Engineering*, vol. 21, 2021.

- [57] M. L. Dezaki, A. Serjouei, A. Zolfagharian, M. Fotouhi, M. Moradi, M. Ariffin and M. Bodaghi, "A review on additive/subtractive hybrid manufacturing of directed energy deposition (DED) process," *Advanced Powder Materials*, vol. 1, no. 4, 2022.
- [58] M. Rombouts, G. Maes, M. Mertens and W. Hendrix, "Laser metal deposition of Inconel 625: Microstructure and mechanical properties," *Journal of Laser Applications*, vol. 24, 2012.
- [59] J. M. Wilson, C. Piya, Y. C. Shin, F. Zhao and K. Ramani, "Remanufacturing of turbine blades by laser direct deposition with its energy and environmental impact analysis," *Journal of Cleaner Production*, vol. 80, pp. 170-178, 2014.
- [60] S. B. M. L. S. T. M. B. L. Abdollah Saboori and P. Fino, "How the nozzle position affects the geometry of the melt pool in directed energy deposition process," *Powder Metallurgy*, vol. 62, no. 4, pp. 213-217, 2019.
- [61] A. Pilipovic, P. Raos and M. Sercer, "Experimental testing of quality of polymer parts produced by laminated object manufacturing - LOM," *Technical Gazette*, vol. 18, no. 2, pp. 253-260, 2011.
- [62] S. Kumar, I. Singh, S. S. Koloor, D. Kumar and M. Y. Yahya, "On Laminated Object Manufactured FDM-Printed ABS/TPU Multimaterial Specimens: An Insight into Mechanical and Morphological Characteristics.," *Polymers*, vol. 14, 2022.
- [63] B. Chang, P. Parandoush, X. Li, S. Ruan, C. Shen, R. A. Behnagh, Y. Liu and D. and Lin, "Ultrafast printing of continuous fiber-reinforced thermoplastic composites with ultrahigh mechanical performance by ultrasonic-assisted laminated object manufacturing," *Polymer Composites*, vol. 41, pp. 4706-4715, 2020.
- [64] T. Ltd., "“WHAT IS LAMINATED OBJECT MANUFACTURING (LOM)?”," TWI Global, 2022. [Online]. Available: <https://www.twi-global.com/technical-knowledge/faqs/what-is-laminated-object-manufacturing-lom#HowdoesitWork>.
- [65] A. May-Pat, A. Valadez-González and P. J. Herrera -Franco, "Effect of fiber surface treatments on the essential work of fracture of HDPE-continuous henequen fiber-reinforced composites," *Polymer Testing*, vol. 32, no. 6, p. 1114–22, 2013.
- [66] E. Gallo, B. Schartel, D. Acierno, F. Cimino and P. Russo, "Tailoring the flame retardant and mechanical performances of natural fiber-reinforced biopolymer by multi-component laminate.," *Composites Part B: Engineering*, vol. 44, no. 1, pp. 112-119, 2013.

- [67] X. Wang, M. Jiang, Z. Zhou, J. Gou and D. Hui, "3D printing of polymer matrix composites: a review and prospective," *Composites Part B: Engineering*, vol. 110, pp. 442-458, 2017.
- [68] G. D. Goh, Y. L. Yap, S. Agarwala and W. Y. Yeong, "Recent progress in additive manufacturing of fiber reinforced polymer composite," *Adv. Mater. Technol.*, vol. 4, p. 1800271, 2018.
- [69] D. Correa, A. Papadopoulou, C. Guberan, N. J. Haveri, S. Reichert, A. Menges and S. Tibbits, "3D-printed wood programming hygroscopic material transformations," *3D Printing and Additive Manufacturing*, vol. 2, no. 3, pp. 106-117, 2015.
- [70] J. I. Montalvo, "3D PRINTING WITH NATURAL FIBER REINFORCED FILAMENT," 2015.
- [71] A. L. Duigou, M. Castro, R. Bevan and N. Martin, "3D printing of wood fibre biocomposites from mechanical to actuation functionality," *Materials & Design*, vol. 96, pp. 106-114, 2016.
- [72] R. Matsuzaki, M. Ueda, M. Namiki, T. Jeong, H. Asahara, K. Horiguchi, T. Nakamura, A. Todoroki and Y. Hirano, "Three-dimensional printing of continuous-fiber composites by in- nozzle impregnation," *Scientific Reports*, vol. 6, no. 23058, 2016.
- [73] D. Stoof, K. Pickering and Y. Zhang, "Fused deposition modeling of natural fibre/polylactic acid composites," *J. Compos. Sci.*, vol. 1, no. 1, pp. 01-08, 2017.
- [74] D. Stoof and K. Pickering, "3D printing of natural fibre reinforced recycled polypropylene," *Processing and Fabrication of Advanced Materials - XXV*, pp. 668-691, 2017.
- [75] J. I. Montalvo N., M. A. Hidalgo-Salazar, E. E. Nunez and A. J. R. Arciniegas, "Thermal and mechanical behavior of biocomposites using additive manufacturing," *Int. J. Interact Des. Manuf.*, vol. 12, pp. 449-458, 2018.
- [76] M. Kariz, M. Sernek and M. K. Kuzman, "Use of wood powder and adhesive as a mixture for 3D printing," *European J. Wood and Wood Products*, vol. 74, no. 1, pp. 123-126, 2016.
- [77] L. Jiang, X. Peng and D. Walczyk, "3D printing of biofiber-reinforced composites and their mechanical properties: a review," *Rapid Prototyping Journal*, vol. 26, no. 6, pp. 1113-1129, 2020.
- [78] Y. Guo, W. Zeng and K. Jiang, "Preparation and Selective Laser Sintering of Wood-Plastic Composite Powers and Post Processing," *Digest J. Nanomaterials and Biostructures*, vol. 6, no. 3, pp. 1435-1444, 2011.

- [79] W. Zeng, Y. Guo, K. Jiang, Z. Yu and Y. Liu, "Preparation and selective laser sintering of Rice husk-Plastic Composite powder and post processing," *Digest J. Nanomaterials and Biostructures*, vol. 7, no. 3, pp. 1063-1070, 2012.
- [80] Z. Xin, Y. Guo, P. Yu and W. Zeng, "A study on the properties of rapidly prototyped wood-plastic composites based on selective laser sintering," in *International Technology and Innovation Conference*, 2009.
- [81] L. Quan, D. Li, C. Zhang and C. Zhu, "Preparation and mechanical properties of photocuring 3D printing composite by three-dimensional weaving," *J. Silk*, vol. 55, no. 2, pp. 13-18, 2018.
- [82] V. C. Li, X. Kuang, A. Mulyadi, C. M. Hamel, Y. Deng and H. J. Qi, "3D printed cellulose nanocrystal composites through digital light processing," *Cellulose*, vol. 26, no. 6, pp. 3973-3985, 2019.
- [83] L. Jiang, A. S. Amarasekara, Q. D. Jackson and D. Wang, "MECHANICAL PROPERTIES OF THE WOVEN NATURAL FIBER REINFORCED SHEET STOCKS USED FOR THE LAMINATED OBJECT MANUFACTURING (LOM) RAPID PROTOTYPING PROCESS," in *American Society for Composites*, 2021.
- [84] L. Weisensel, N. Travitzky, H. Sieber and P. Greil, "Laminated Object Manufacturing (LOM) of SiSiC Composites," *Adv. Eng. Mat.*, vol. 6, no. 11, pp. 899-903, 2004.
- [85] I. Objects, "Composite-based Additive Manufacturing (CBAM)," 2016. [Online]. Available: <https://www.compositesworld.com/cdn/cms/FM2016-ImpossibleObjects.pdf>.
- [86] L. Kaplan, "Impossible Objects, CBAM: Composite-Based Additive Manufacturing," 4 August 2017. [Online]. Available: <http://additivemanufacturingseries.com/wp-content/uploads/2017/04/Kaplan.pdf>.
- [87] J. Suteja, H. Firmanto, A. Soesanti and C. Christian, "Properties investigation of 3D printed continuous pineapple leaf fiber re-inforced PLA composite," *J. Thermoplast. Compos. Mater.*, vol. 35, p. 2052–206, 2022.
- [88] M. Osman and M. Atia, "Investigation of ABS-rice straw composite feedstock filament for FDM.," *Rapid Prototyp. J.*, vol. 24, pp. 1067-1075, 2018.
- [89] J. Safka, M. Ackermann, J. Bobek, M. Seidl, J. Habr and L. Behalek, "Use of composite materials for FDM 3Dprint technology.," *Mater. Sci. Forum*, vol. 862, p. 174–181, 2016.

- [90] A. De Oliveira, N. de Macedo and D. Rosa, "Eco-efficiency of Poly (lactic acid)-Starch-Cotton composite with high natural cotton fiber content: Environmental and functional value.," *J. Clean. Prod.*, vol. 217, pp. 32-41, 2019.
- [91] G. Chen and H. Luo, "Effects of node with discontinuous hierarchical fibers on the tensile fracture behaviors of natural bamboo.," *Sustainable Materials and Technologies*, vol. 26, 2020.
- [92] A. Santoni, P. Bonfiglio, P. Fausti, C. Marescotti, V. Mazzanti, F. Mollica and F. Pompoli, "Improving the sound absorption performance of sustainable thermal insulation materials: Natural hempfibres.," *Appl. Acoust.*, vol. 150, pp. 279-289, 2019.
- [93] O. El Hawary, L. Boccarusso, M. P. Ansell, M. Durante and F. Pinto, "An Overview of Natural Fiber Composites for Marine Applications," *Journal of Marine Science and Engineering* , vol. 11, no. 5, p. 1076, 2023.
- [94] M. Nasir, M. Taha, N. Razali, R. Ilyas, V. Knight and M. Norraahim, "Effect of Chemical Treatment of Sugar Palm Fibre on Rheological and Thermal Properties of the PLA Composites Filament for FDM 3D Printing.," *Materials*, vol. 15, p. 8082, 2022.
- [95] C. Baley, A. Bourmaud and P. Davies, "Eighty years of composites reinforced by flax fibres: A historical review," *Compos. Part A*, 2021.
- [96] ., Arslanoglu, S. Sert, H. ,Sahin, S. Aytaç and A. El Sabagh, " Yield and Yield Criteria of Flax Fiber (*Linum usitatissimum* L.) as Influenced by different plant densities," *Sustainability*, vol. 14, p. 4710, 2022.
- [97] M. Ahmad, M. Ishak, M. Mohammad Taha, F. Mustapha and Z. Leman, " A Review of Natural Fiber-Based Filaments for 3D Printing: Filament Fabrication and Characterization.," *Materials*, vol. 16, p. 4052, 2023.
- [98] K. Pickering, M. Efendy and T. Le, ".A review of recent developments in natural fiber composites and their mechanical performance," *Compos. Part A Appl. Sci. Manuf*, vol. 83, pp. 98-112, 2016.
- [99] S. Han, M. Taha, M. Mansor and M. Rahman, " Investigation of tensile and flexural properties of kenaf fiber-reinforced acrylonitrile butadiene styrene composites fabricated by fused deposition modeling.," *J. Eng. Appl. Sci.* , vol. 52, p. 69, 2022.
- [100] W. Yu, J. Shi, L. Sun and W. Lei, "Effects of Printing Parameters on Properties of FDM 3D Printed Residue of Astragalus/Polylactic Acid Biomass Composites.," *Molecules* , vol. 27, p. 7373, 2022.

- [101] Y. Tao, H. Wang, Z. Li, P. Li and S. Shi, "Development and Application of Wood Flour-Filled Polylactic Acid Composite Filament for 3D Printing.," *Materials* , vol. 10, p. 339, 2017.
- [102] D. Muck, H. Tomc, U. Elesini, M. Ropret and M. Leskovšek, "Colour Fastness to Various Agents and Dynamic Mechanical Characteristics of Biocomposite Filaments and 3D Printed Samples," *Polymers* , vol. 13, p. 3738, 2021.
- [103] W. Ahmed, F. Alnajjar, E. Zaneldin, A. Al-Marzouqi, M. Gochoo and S. Khalid, "Implementing FDM 3D Printing Strategies Using Natural Fibers to Produce Biomass Composite.," *Materials*, vol. 13, p. 4065, 2020.
- [104] R. R. Md., M. M. Rahman, S. Hamdan and J. Chang Hui Lai, "Impact of Maleic Anhydride, Nanoclay, and Silica on Jute Fiber-reinforced Polyethylene Biocomposites.," *BioResources*. 11, 2016.
- [105] K. Rassiah, A. Ali and M. Ahmad, "A Comparison Analysis on Mechanical Properties Between Laminated Woven Bamboo and Epoxy Composite Versus Laminated Strip Bamboo and Polyester Composite.," in *Progress in Engineering Technology V. Advanced Structured Materials*, vol. 183, Springer, 2023.
- [106] A. Chatterjee, S. Kumar and H. Singh, "Tensile strength and thermal behavior of jute fibre reinforced polypropylene laminate composite," *Composites Communications*, vol. 22, p. 100483, 2020.
- [107] L. Jiang, D. Walczyk, G. McIntyre, R. Bucinell and G. Tudryn, "Manufacturing of biocomposite sandwich structures using mycelium-bound cores and preforms.," *Journal of Manufacturing Processes*, vol. 28, pp. 50-59, 2017.
- [108] M. Sayeed, A. Sayem, J. Haider, S. Akter, M. Habib, H. Rahman and S. Shahinur, "Assessing Mechanical Properties of Jute, Kenaf, and Pineapple Leaf Fiber-Reinforced Polypropylene Composites: Experiment and Modelling," *Polymers* , vol. 15, p. 830, 2023.
- [109] Addcomposites, "Addcomposites," 13 December 2021. [Online]. Available: <https://www.addcomposites.com/post/what-are-natural-fiber-composites-basics-applications-and-future-potentials>. [Accessed 06 June 2023].
- [110] L. Jiang, S. Shahriar, T. Grady and X. Peng, "Woven Natural Fiber-Reinforced PLA Polymers 3D Printed through a Laminated Object Manufacturing Process," in *SAMPE 2023 Proceedings*, Seattle, WA, 2023.
- [111] M. P. Groover, "Chapter 3 Mechanical Properties of Materials," in *FUNDAMENTALS OF MODERN MANUFACTURING: Materials, Processes, and Systems Fourth Edition* , Wiley, 2010.

- [112] S. Arunavathi, R. D. Eithiraj and K. Veluraja, "Physical and mechanical properties of jute fiber and jute fiber reinforced paper bag with tamarind seed gum as a binder - An eco-friendly material," in AIP Conference Proceedings, 2017.
- [113] A. Nugroho, R. Ardiansyah, L. Rusita and I. L. Larasat, "Effect of layer thickness on flexural properties of PLA (PolyLactid Acid) by 3D printing," Journal of Physics: Conference Series, vol. 1130, p. 012017, 2018.
- [114] MatWeb, "Overview of materials for Polylactic Acid (PLA) Biopolymer," 2022. [Online]. Available: <https://www.matweb.com/search/DataSheet.aspx?MatGUID=ab96a4c0655c4018a8785ac4031b9278&ckck=1>. [Accessed 13 Dec. 2022].
- [115] BCN3D, "PLA Filament: The pros and cons of this 3D printing staple material," 22 July 2020. [Online]. Available: <https://www.bcn3d.com/pla-filament-stands-for-strength-temp/#:~:text=PLA's%20strength&text=Tensile%20strength%20is%2037%20Mpa,density%20is%201.3%20g%2Fcm3>. [Accessed 13 Dec. 2022].
- [116] A. Pilipovic, P. Raos and M. Sercer, "Experimental testing of quality of polymer parts produced by laminated object manufacturing - LOM," Technical Gazette, vol. 18, no. 2, pp. 253-260, 2011.
- [117] T. Casalini, F. Rossi, A. Castrovinci and G. Perale, "A Perspective on Polylactic Acid-Based Polymers Use for Nanoparticles Synthesis and Applications," Front. Bioeng. Biotechnol., vol. 7, p. 259, 2019.
- [118] V. Nagarajan, A. K. Mohanty and M. Misra, "Perspective on Polylactic Acid (PLA) based Sustainable Materials for Durable Applications: Focus on Toughness and Heat Resistance," ACS Sustainable Chemistry & Engineering, vol. 4, no. 6, pp. 2899-2916, 2016.
- [119] S. N. Vouyiouka and C. D. Papaspyrides, "4.34 - Mechanistic Aspects of Solid-State Polycondensation," in Polymer Science: A Comprehensive Reference, Elsevier, 2012, pp. 857-874.
- [120] L. Langnau, "How tensile strength relates to 3D printing," Make Parts Fast, 4 Sep. 2019. [Online]. Available: <https://www.makepartsfast.com/how-tensile-strength-relates-to-3d-printing/>. [Accessed 13 Dec. 2022].
- [121] SD3D, "PLA Technical Data Sheet," [Online]. Available: https://www.sd3d.com/wp-content/uploads/2017/06/MaterialTDS-PLA_01.pdf. [Accessed 13 Dec. 2022].
- [122] V. Pinto, T. Ramos, S. A. Alves, J. Xavier, P. J. Taraves, P. Moriera and R. Guedes, "Comparative Failure Analysis of PLA, PLA/GNP and PLA/CNT-

COOH Biodegradable Nanocomposites thin Films," *Procedia Engineering*, vol. 114, pp. 635-642, 2015.

- [123] V. Alagumalai, K. M. T. Babu, R. Aseer and V. Shanmugam, "Wear properties of natural fiber-based composites – A brief review," *Polym Adv Technol.*, pp. 1-14, 2023.
- [124] Wikipedia, "Wikipedia," 23 June 2022. [Online]. Available: https://en.wikipedia.org/wiki/Laminated_object_manufacturing .
- [125] Wikipedia, "Wikipedia," 21 September 2021. [Online]. Available: https://en.wikipedia.org/wiki/Mcor_Technologies_Ltd.

CURRICULUM VITAE

Sazidur Rahman Shahriar sshahriar@pvamu.edu

EDUCATION

- Ph.D. Mechanical Engineering, Rensselaer Polytechnic Institute, Troy, NY (Starting from Spring 2024)
- M.S. Mechanical Engineering, Prairie View A&M University, Prairie View, Texas, 2023
- B.S. Industrial and Production Engineering, Ahsanullah University of Science & Technology, Bangladesh, 2017

WORK EXPERIENCE

- Company: Prairie View A&M University, TX, USA
Position: Graduate Research Assistant, 2022 – Present
Job: Additive Manufacturing, Composites Manufacturing research
- Company: Beta Bangladesh Limited, Bangladesh
Position: Technical Executive 2019 - 2021
- Company: Sinobangla Industries Limited, Bangladesh
Position: Technical Executive 2019 - 2021

PROFESSIONAL, AND WORK-RELATED SKILLS

- Computer-Aided Design: SOLIDWORKS, Siemens NX, Autodesk Fusion360
- 3D Printing Software: ideamaker, intamsuite, catalystEX
- Simulation & Data Analytics: ANSYS, ABAQUS, MATLAB, MINITAB, Sigma Plot, Origin Lab
- Programming: C, Python, Arduino
- Electronic Project Design: Fritzing, Proteus

PUBLICATIONS AND PRESENTATIONS

1. Jiang, Lai, Shahriar, Sazidur Rahman, Grady, Tony, Peng, Xiaobo. Woven Natural Fiber-Reinforced PLA Polymers 3D Printed through a Laminated Object Manufacturing Process, SAMPE Conference Proceedings (2023) DOI: <https://doi.org/10.33599/nasampe/s.23.0198>
2. Sanglap, M. T. E., and Shahriar, S. R. "Influence of Accident-Tolerant Fuel with Steel Cladding for Sustainable Heat Transfer in the Reactor Core of VVER-1200", ASME Open J. Engineering ASME, 1 011023 (2022) DOI: <https://doi.org/10.1115/1.4054476>
3. Shahriar, S.R., Nasir, and Dhar, N. R. "Design and development of SQL system in sustainability issues of machining," AIP Conference Proceedings 1980, 060002 (2018) DOI: <https://doi.org/10.1063/1.5044370>